FIRST PRINCIPLES STUDY OF PROPERTIES OF FUNCTIONALIZED MXENE (Ti_2N) AND DEFECT ON MXENE MONO-LAYERS

A Dissertation

Submitted to the Central Department of Physics,

Tribhuvan University, Kirtipur in the Partial Fulfillment for the

Requirement of Master's Degree of Science in Physics

By

YOGENDRA LIMBU

Reg. No. : 5-2-37-1117-2012

Roll. No. : 1617/073

February, 2021

RECOMMENDATION

It is certified that Mr. **Yogendra Limbu** has carried out dissertation work entitled "**FIRST PRINCIPLES STUDY OF PROPERTIES OF FUNCTIONALIZED MXENE (Ti_2N) AND VACANCY DEFECT ON MXENE MONOLAYERS**" under my supervision and guidance.

I recommended the dissertation in the partial fulfillment for the Master's Degree of Science in Physics.

.....

Supervisor

Assoc. Prof. Dr. Gopi Chandra Kaphle

Central Department of Physics

Tribhuvan University

Kathmandu, Nepal

Date:.....

ACKNOWLEDGEMENT

My gratitude goes to my supervisor Asso. Prof. Dr. Gopi Chandra Kaphle for giving learning opportunity in the field of two dimensional family (MXenes).

I am also equally thankful to our head of department Prof. Dr. Om Prakash Niraula for his motivational encouragement in research. I would also thankful to all faculty members who seemingly or unseemly supported me to completed my research work.

I am extremely thankful to Dr. Durga Paudyal for his strong support in every aspects (especially in band topology and magnetism) during research time period. I would also equally thankful to Dr. Rjendra Adhikari for his valuable support and providing computational resource. I am also thankful to Mr. Hari Paudyal for his kind support especially in computation.

I would like to extend my acknowledge to my friends, Chhatra Tamang, Bhuwan Poudel, Niraj Kumar Shah for their support. Especially thankful our seniors, Alok Lal Karna, Sashi Nepal, Suman Acharya, Ram Babu Ray, and Raj Kumar Rai for their constant support in difficulties during research work period.

Finally, I would like to give thanks to my family member who always encourage and supported in any aspect during the period of my dissertation without whom I wound not have been able to complete this work.

EVALUATION

We certify that we have read this dissertation and in our opinion, it is good in the scope and quality as dissertation in partial fulfillment for the requirement of Master's Degree of Science in Physics.

Evaluation Committee

.....

Assoc. Prof. Dr. Gopi Chandra Kaphle

Supervisor

Central Department of Physics

Tribhuvan University

Kathmandu, Nepal

.....

Prof. Dr. Om Prakash Niraula

Head

Central Department of Physics

Tribhuvan University

Kathmandu, Nepal

.....

External Examiner

.....

Internal Examiner

Date:.....

ABSTRACT

The evolution of structural and electronic properties of graphene-like titanium nitride MXene has been studied with different functional groups (-F, -O, -H, and -OH) employing first principles electronic structure calculations. The calculated formation and cohesive energies reveal the chemical stability of all MXenes and MAX phase. The bare MXene exhibits same hexagonal symmetry as its parent bulk MAX phase. The surface terminated species are distributed randomly on the surface of bare MXene with preferred locations between Ti atoms. The MAX phase and all the studied defect free functionalized MXenes are metallic in nature except for oxygen terminated one, which is found to be 100% spin polarized half-metallic. Additionally, the bare MXene is nearly half-metallic ferromagnet. The spin orbit coupling (SOC) only significantly influences in the bare MXene and trivially influences with O and N defected MXenes. The strain effect influences the Fermi level thereby shifting towards the lower energy state under compression and toward higher energy state under tensile strain in Ti_2NH_2. These properties are reversed in the case of Ti_2N, Ti_2NF_2, and $Ti_2N(OH)_2$. The half-metallic nature changes to semi-metallic under 1% compression and completely destroyed under 2% compression. The variable topological phenomena have been studied in pristine, strained, and defected MXenes. Interestingly, the band structure of Ti_2NO_2 remarkably transforms from half-metallic to semi-conducting (with large band gap of 1.73 eV) in 12.5% Ti, weakly semi-conducting in 5.5% Ti, and topological semi-metal in 12.5% oxygen. The N defect with 25% converts from half-metallic to metallic with certain topological features. Further, the 12.5% Co substitution in Ti_2NO_2 preserves the half-metallic character, whereas Mn substitution allows to convert half-metallic into weak semi-metallic preserving ferromagnetic (FM) character. However, Cr substitution converts half-metallic FM to half-metallic anti-ferromagnetic (AFM) character.

List of Abbreviations

PBE	Perdew-Burke-Ernzerhof
PWscf	Plane Wave self-consistent field
DFT	Density Functional Theory
PAW	Projector Augmented Wave
GGA	Genralized Gradient Approximation
DOS	Density of States
PDOS	Partial Density of States
ESPRESSO	opEn-Source Package for Research in Electronic Structure, Simulation, and Optimization
SCF	Self Consistent Field
CP	Car Parrinello
HK	Hohenberg-Kohn
HF	Hartee-Fock
KS	Kohn-Sham
LSDA	Local Spin Density Approximation
LDA	Local Density Approximation
XC	Exchange and Correlation
TM	Trasition Metal
SOC	Spin Orbit Coupling
2D	Two Dimensional
3D	Three Dimensional
KF	Potassium Fluoride

HF	Hydrofluoric
GEA	Gradient Expansion Approximation
NEB	Nudged Elastic Band
NM	Non-magnetic
FM	Ferro-magnetic
AFM	Anti-ferromagnetic

List of Figures

List of Tables

Contents

Chapter 1

Introduction

1.1 General Consideration

After the discovery of graphene by the group of Novoselov and Geim in 2004 [5], many researchers are focusing on two-dimensional (2D) materials with diverse physical phenomena. Many 2D materials go beyond the graphene [6]. Atomically-thin 2D materials have unique physical, chemical, electronic, and optical properties [7], as well as their various potential applications compared to their conventional three-dimensional (3D) counterparts. Graphene, which is a single atomic layer of carbons [8], is the most illustrious and studied of these newly emerging 2D materials. However, graphene is limited to just carbon atoms in its composition, whereas the rapidly growing area of 2D materials include large set of transition metal (TM) carbides and nitrides (MXenes) [9]. These new 2D materials are one of the most promising candidate materials in materials science and engineering. These materials have wide range of applications in diverse field such as energy storage, water electrolyzers, super-capacitor, lithium ions batteries [10], biomedical applications [11], sensors [12], catalysis [13], and spintronic devices [14].

In 2011, a new group of 2D materials based on TM carbides were synthesized [15]. The 2D MXenes are obtained from 3D MAX phase, having general chemical formula $M_{n+1}AX_n$ where n=1 to 3, M is TM, A is an A-group (basically IIIA and IVA or groups

13 and 14) elements and X is either carbon or nitrogen. The unit cell of the MAX phase is characterized by near close-packed M layers interleaved with the layers of a pure A-group elements, with the X atoms filling the octahedral sites. The A-group elements are positioned at the center of trigonal prism [16]. Currently, investigators are paying attention to theoretical modeling of the MAX phases. Unlike the MX phases, bonding in the MAX phases are combination of metallic, covalent, and ionic. In the MX phase, there is a strong overlap between the *p* orbitals of the X elements and the *d* orbitals of the M atoms, making the strong covalent bonds that are comparable to those in the MX binaries [17].

The 2D materials offer a large variety of chemical compositions compared to graphene [18]. MXenes can be thought of as conductive clays in which cation intercalation and exchange easily occur [19]. Among all experimentally synthesized and theoretically predicted MXenes, the carbide based MXenes are widely studied especially $Ti_3C_2T_2$ (T= surface termination) [20]. On the basis of stability and activity, many different MXenes were predicted to highly active for hydrogen evolution reaction electrocatalysts, the thickness of this materials play an important role to turn activity of proposed MXenes [21]. In contrast, the synthesis of titanium nitride based MXene is quite difficult due to large value of formation energy in their 3D MAX phase and it's poor stability in etchant, typically in hydrofluoric acid (HF) [22]. The Ti_4N_3 MXene was successfully synthesized from precursor Ti_4AlN_3 using molten fluoride salt to etching Al element [23]. The Ti_2N MXene was successfully synthesized by immersing Ti_2AlN in a mixture of potassium fluoride (KF) and hydrochloric acid (HCl) [22]. The nitride MXenes exhibit better pseudocapacitive performance than carbide based MXenes [24]. This type of 2D materials have high value of electrical conductivity and wide range of absorption application properties, which are key to their success in the aforementioned applications [25]. The MXene Ti_2N is the 2D materials obtained from selectively etching of 'A' element from bulk MAX phase Ti_2AlN. The mono-layer MXene Ti_2N is terminated with -OH, -H, -O, -F, and functionalized MXenes become Ti_2NT_2 (T = -OH, -H, -O, -F). After surface termination on mono-layer MXene, there may be significant

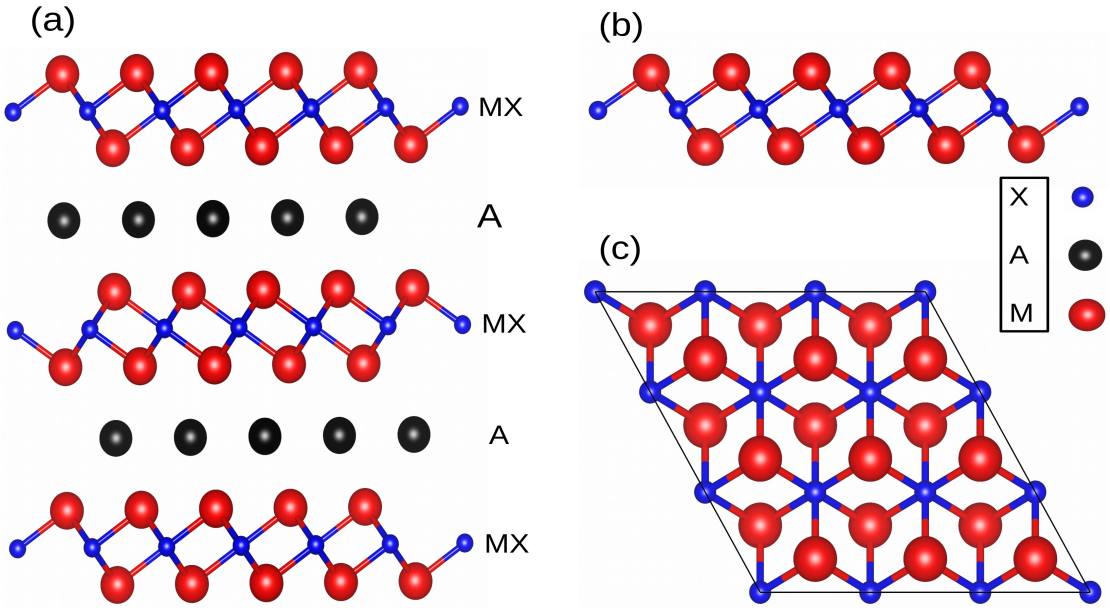

Figure 1.1: (Color online) (a) Hexagonal closed packed (hcp) structure of MAX phase M_2AX, and (b) and (c) are corresponding side and top views of MXene M_2X in $3\times3\times1$ super-cell.

change in structural stability, electronic, and magnetic properties as compared to bare MXene [1].

The 2D materials are highly flexible and extremely sensitive to the applied strain to modulate the electronic band structure [26]. The strain in 2D materials can be introduced by many ways, such as depositing flexible substrate, subjecting them to external load, pseudomorphic growth, and nano indentation [27]. The effect of strain in graphene sheet was experimentally observed and maximum bi-axial strain was attained up to 25% before breaking the C-C bond in graphene sheet [28]. The nature of band structure changes from indirect band gap to direct band gap under tensile strain and the band gap closes under compression strain in Ti_2CO_2 MXene [29]. Therefore, in addition to applied strain in MXenes sheet, it is worth to investigate the magnitude of externally applied strain up to which the considered structures do not break.

Despite having all fascinating properties, the defect in MXenes severely alter the structural stability, electronic, and magnetic properties [30]. The presence of intrinsic Ti-defects in $Ti_3C_2T_2$ layers was experimentally determined (using scanning tunneling microscopy) in ref. [31]. However, the detail explanation of structural defect in MXene is missing, which is addressed here.

Beside the major astonishing properties and applications of MXenes, there was a limitation in the field of storage capacity. This was solved by doping nitrogen atom in Nb_2CT_2 MXenes, which increases storage capacity in lithium ions batteries [32]. The Nb doping can change electronic properties by shifting the Fermi level toward the conduction band that enhances the electronic conductivity in $Ti_3C_2T_2$ [33]. Further, the B doping in oxygen terminated Ti_2C MXene improves the elastic properties with reasonably high critical strain making suitable for the flexible device applications [34]. The doping of selected transition elements in graphene changes the conduction properties from semi-conductor to 100% spin polarized half-metallic [35]. The half-metallic properties [36] have created a great attention due to their potential applications in spintronic devices [37]. The selection of dopant atom plays a significant role to change the electronic properties. So, the doping effect in MXenes is one of the important emerging fields to enhance the properties of graphene like 2D MXenes sheet.

Furthermore, the realization of free-standing single atomic layers of graphene opened a new route towards the topological phenomena in 2D materials. Firstly, the Dirac cones were observed in graphene [38]. These gapless Dirac cones in graphene are robust under the structural deformation [39], which exhibit peculiar transport phenomena in their electronic band structure [40]. The experimental study shows the high mobility of charge carriers and an unusual half integer quantum Hall effect for both electrons and holes carriers in graphene [41]. The coexistence of electron and hole packets with Dirac cone is responsible for the quantum oscillation in 3D topological materials beyond the graphene [42]. Similarly, the Zr_2Si MXene also exhibits anisotropic Dirac cones with comparable Fermi velocities [43]. Theoretically, the titanium carbide based MXenes can also be predicted to exhibit the Dirac topology in their electronic band structure [44]. In the similar vein, the topological and associated properties are expected in Ti_2N MXene.

In this paper, we have studied the electronic and magnetic properties of the MAX phase, and bare and it's corresponding functionalized MXenes. The chemical stability of all MXenes and MAX phase were studied with the help of cohesive and formation ener-

gies. The O terminated MXene was found to be relatively stable as compared to all other MXenes. The MAX phase and functionalized MXenes exhibit the non-magnetic (NM) metallicity except for O terminated MXene, which is predicted to be half-metallic ferromagnet. The strain effect in mono-layer MXene influences the position of the Fermi level with different topological nature. The defect in Ti_2NO_2 brings significant changes in electronic properties with various topological nature. The electronic properties of Ti defect strongly depend upon vacancy concentration. The half-metallic nature changes to strong and weak semi-conductor depending upon the concentration. Similarly, half-metallic property changes to topological semi-metal and also remain metallic with Dirac topology depending on different defects. Interestingly, the TM substitution introduces peculiar magnetic to semi-metallic to topological phenomena in Ti_2NO_2 MXene.
According to the best of our knowledge, the topological features, effect of SOC in the band structure, vacancy concentration dependent semi-conducting nature, doping, and detail explanation of half-metalicity are the new finding of this work.

1.2 Scope of Present Work

In this work, we have extensively studied on the structural stability, electronic, magnetic, and topological properties of MAX phase, bare and its corresponding functionalized MXenes in $1 \times 1 \times 1$, $2 \times 2 \times 1$, and $3 \times 3 \times 1$ cells separately. We have also studied the single vacancy defect and doping in the relatively stable configuration Ti_2NO_2 in $2 \times 2 \times 1$ and $3 \times 3 \times 1$ super-cells respectively. Here, the stability of MXenes were calculated through formation and cohesive energies. The calculated values of cohesive ad formation energies reveal the structural stability from $2 \times 2 \times 1$ super-cell. Our research would help to understand how the structure, electronic, magnetic, and topological properties change as we go from the bulk phase to surface states.
In chapter 2, we described the theoretical background and methodology used for completion of our work such as Born approximation for many body problem, Schrdinger equation, Hartee-Fock method, Hohenberg-Kohn Theorem 1, Hohenberg-Kohn Theo-

rem 2, Basics of Density Functional Theory (DFT), exchange correlation functional. In chapter 3, we described the computational package and its implementation in our research work. In chapter 4, we discussed the results of this research work. And finally in chapter 5, we discussed the conclusion of our work and suggest future possibilities of this work. It would be helpful for who try to extends this research or 2D family in coming future days.

Chapter 2

Theoretical Background

2.0.1 Born-Oppenhiemer Approximation

The solid are system composing by mutually interacting system of electrons, protons and its motion. The many properties of interacting system is obtained through by determining eigenfunction which is the fundamental problem in solid state physics. The Hamiltonian of interacting system is given by

$$\hat{H} = \sum_{i=1}^{N} \frac{-\hbar^2}{2m_e} {\nabla_i}^2 + \sum_{I=1}^{M} \frac{-\hbar^2}{2M_I} {\nabla_I}^2 - \sum_{i}^{N} \sum_{I}^{M} \frac{Z_I e^2}{|\mathbf{r}_i - \mathbf{R}_I|} + \sum_{j>i}^{N} \sum_{i=1}^{N} \frac{e^2}{|\mathbf{r}_i - \mathbf{r}_j|} + \sum_{J>I}^{M} \sum_{I=1}^{M} \frac{Z_I Z_J e^2}{|\mathbf{R}_I - \mathbf{R}_J|} \tag{2.1}$$

where m and M are the masses of electron and nuclei. i , j and I, J are number whose takes value from 1 to N and M, respectively. First two term represent sum of kinetic energy of nuclei and electron and remaining term give interaction term. First three terms show attractive in nature whereas the last two terms show repulsive in nature. The mass of electrons are very small as compared to nuclei so nuclei is considered to be fixed for the motion of electrons. On other hand, the nuclei moves with in the circumstance of average potential generated by revolving electrons called as Born-Oppenheimer approximation, which takes nuclear effect remain static first and solves the problem by taking nuclear motion into account later. The Born-Oppenheimer is also called adia-

batic. This approximation provide the concept about dependency of electronic wave function on nuclear position not in nuclear motion. So, above Hamiltonian can be separated into two groups i.e core and valence / conduction electrons. The core electrons which moves with nuclei and conduction or valence electrons transport throughout the solid. The Hamiltonian can be written as,

$$\hat{H} = \sum_{i=cond.elec.}^{N} \frac{{p_i}^2}{2m_e} + \sum_{I=1}^{M} \frac{{p_I}^2}{2M_I} + \sum_{I,I'}^{M} V_{II'}(|\mathbf{R}_I - \mathbf{R}_{I'}|) + \frac{e^2}{2} \sum_{I,I'=cond.elec.} \frac{1}{(|\mathbf{r}_I - \mathbf{r}_{I'}|)} + \sum_{i,I} V_{ei}(|\mathbf{r}_i - \mathbf{R}_I|) + E_{core} \tag{2.2}$$

$$\hat{H} = T_I + T_e + V_{I,I'} + V_{ee} + V_{eI} + E_{core} \tag{2.3}$$

Where $\mathrm{V}_{I,I'}$ and V_{ei} represent the effective potential between ions and between valence electrons with ions. The total wave function of system is the function of electron position and ion position expressed as

$$\psi(\mathbf{r}, \mathbf{R}) = \sum_{n} \phi(\mathbf{R}) \psi_{e,n}(\mathbf{r}, \mathbf{R}) \tag{2.4}$$

Where $\psi(\mathbf{r}, \mathbf{R})$ is the solution of electrons-ions for fixed set of ions position $\mathbf{R}$. The Schrodinger wave equation become

$$(T_I + T_e + V_{I,I'} + V_{ee} + V_{eI} + E_{core} \psi(\mathbf{r}, \mathbf{R}) = E\psi(\mathbf{r}, \mathbf{R}) \tag{2.5}$$

$$(T_I + V_{I,I'} + E_{core})\psi(\mathbf{r}, \mathbf{R}) + \sum_{n} \phi_n (T_{ee} + V_{ee} + V_{ei}) \psi_{e,n}(\mathbf{r}, \mathbf{R}) = E\psi(\mathbf{r}, \mathbf{R}) \tag{2.6}$$

Here first part represents the electronic and second represents ionic respectively. Let $E_{e,n}(\mathbf{R})$ is energy for the electrons system for fixed set of nuclear position $\mathbf{R}$. Then

electronic and ionic eigenvalue equation can be separated as

$$(T_e + V_{ee} + V_{ei})\psi_{e,n}(\mathbf{r}, \mathbf{R}) = E_{e,n}\psi_{e,n}(\mathbf{r}, \mathbf{R}) \tag{2.7}$$

and

$$(T_I + V_{II} + E_{core} + E_{e,n}(\mathbf{R})) = E_n\phi_n(\mathbf{R}) \tag{2.8}$$

The equations 2.7 and 2.8 are the principles results in Born-Oppenheimer approximation [45].

2.0.2 Hartree Approximation

We are moving to simplify the complex many body problem to simplified form by considering system as the collection of ions and essential quantum mechanical particle that reflect the behavior of the electrons in system is called single-particle picture. Where the each electrons are revolving around nucleus under the central field develop by nucleus and rest of the electrons present within the system is called Hartree field [46]. According to Hartree, the total wave function is the product of one-electron wave function i.e

$$\psi(\mathbf{r}_1\, \mathbf{r}_2, ..., \mathbf{r}_N) = \phi_1(\mathbf{r}_1), \phi_2(\mathbf{r}_2), ..., \phi_N(\mathbf{r}_N) \tag{2.9}$$

Where $\phi_i(\mathbf{r}_i)$ is the single particle wave function. The expectation value of Hamiltonian is calculated as

$$\begin{aligned} \hat{H} = \langle\psi|\, H\, |\psi\rangle = \sum_i \int d\mathbf{r}\psi_i^*(\mathbf{r}) \left\{ -\frac{1}{2}\nabla^2 + U_{ion}(\mathbf{r} \right\} \psi_i(\mathbf{r})) \\ + \frac{1}{2}\sum_i \sum_{i\neq j} \int d\mathbf{r} d\mathbf{r'} \frac{|\psi_i|^2 |\psi_j(\mathbf{r'})|^2}{|\mathbf{r} - \mathbf{r'}|} \end{aligned} \tag{2.10}$$

Introducing the Lagrange multiplier ϵ_i, for normalized one-electron wave function and minimizing equation (2.10) with respect to wave function,

$$\frac{\delta}{\delta\psi}[\langle\psi|\, H\, |\psi\rangle - \sum_j \epsilon_j \int |\psi_j|^2 d\mathbf{r}] = 0 \tag{2.11}$$

This equation lead to give set of single particle equation as,

$$(-\frac{1}{2}\nabla^2 + U_{ion}(\mathbf{r})\psi_i(\mathbf{r}) + \sum_{i\neq j}\int d\mathbf{r'}\frac{|\psi_j(\mathbf{r'})|^2}{|\mathbf{r}-\mathbf{r'}|}\psi_i(\mathbf{r}) = \epsilon_i\psi_i(\mathbf{r}) \tag{2.12}$$

This equation is known as Hartree equation.

2.0.3 Hartree-Fock Approximation

In Hartree approximation, the total wave function of system is the product of single particle wave function. So, there is some missing in motion of electron contributed by asymmetry of complete wave function. As a result, exchange term in energy is missing. This error was corrected by V. Fock using anti-symmetrized wave function in determinant form [46]. For N electrons system total anti-symmetrized wave function can be expressed as,

$$\Psi \approx \Phi_{SD} = \frac{1}{\sqrt{N!}}\begin{vmatrix} \chi_1(\mathbf{x}_1) & \chi_2(\mathbf{x}_1) & \dots & \chi_N(\mathbf{x}_1) \\ \chi_1(\mathbf{x}_2) & \chi_2(\mathbf{x}_2) & \dots & \chi_N(\mathbf{x}_2) \\ \vdots & \vdots & & \vdots \\ \chi_1(\mathbf{x}_N) & \chi_2(\mathbf{x}_N) & \dots & \chi_N(\mathbf{x}_N) \end{vmatrix}. \tag{2.13}$$

Here, $\chi_i(\mathbf{x}_i)$ are called spin orbitals and are composed of spatial orbitals $\phi_i(\mathbf{r})$ and one of two spin function $\alpha(s)$ or $\beta(s)$.

$$\chi_i(\mathbf{x}) = \phi(\mathbf{r})\sigma(s) \quad ;\ \sigma = \alpha, \beta \tag{2.14}$$

This spin functions have property of ortho-normality .i.e $\langle\alpha|\,|\alpha\rangle = \langle\beta|\,|\beta\rangle = 1$ and $\langle\alpha|\,|\beta\rangle = \langle\beta|\,|\alpha\rangle = 0$.

The spin orbitals are chosen in such a way that it follows orthonormal properties.

$$\int \chi_i^*(\mathbf{x})\chi_i(\mathbf{x})d\mathbf{x} = \langle\chi_i|\chi_j\rangle = \delta_{ij} \tag{2.15}$$

Where, δ_{ij} is Kronecker delta (δ_{ij}= 1 for i = j and δ_{ij} = 0 for $i \neq j$).

$$\hat{H} = \langle\psi| H |\psi\rangle \tag{2.16}$$

Now applying variation principle in equation (2.16). Then, finally Hartree-Fock energy E_{HF} in terms of integrals of the one- and two-electron operator,

$$E_{HF} = \sum_{ij} \langle i| h |j\rangle + \frac{1}{2}\sum_{ij}[\langle ii| |jj\rangle - \langle ij| |ji\rangle] \tag{2.17}$$

Where $\langle i| h |j\rangle$ is one-electron operator define as

$$\langle i| h |j\rangle = \int d\mathbf{x}_1 \chi_i^*(\mathbf{x}_1) \left\{ -\frac{1}{2}\nabla^2 - \sum_j^M \frac{Z_j}{|\mathbf{r}_1 - \mathbf{R}_j|} \right\} \chi_j(\mathbf{x}_1) \tag{2.18}$$

gives the contribution due to the kinetic energy and electron-nucleus attractive interaction and two-electrons operator as,

$$\langle ii|jj\rangle = \int\int |\chi_i(\vec{x}_1)|^2 \frac{1}{r_{12}} |\chi_j(\vec{x}_2)|^2 d\vec{x}_1 d\vec{x}_2 \tag{2.19}$$

$$\langle ij|ji\rangle = \int\int \chi_i(\vec{x}_1)\chi_j^*(\vec{x}_1)\frac{1}{r_{12}}\chi_j(\vec{x}_2)\chi_i^*(\vec{2})d\vec{x}_1 d\vec{x}_2 \tag{2.20}$$

representing Coulomb and exchange integral between the electrons respectively [47].

2.0.4 Thomas-Fermi Approximation

The Thomas-Fermi (TF) model is a quantum mechanical theory for the electronic structure calculation of many-body systems developed semi-classically after the introduction of the Schrodinger equation. Working independently, Thomas and Fermi used this statistical model in 1927 to approximate the distribution of electrons in an atom. They were succeed to attempt to use electrons density instead of wave function to obtained the information about many body system [48]. This concept of electron density is the fundamental basis variables in Density Functional Theory. For simplicity consider an

atom with N electrons with atomic number Z. Thomas-Fermi energy functional can be expressed as,

$$E_{TF}[\rho] = \frac{3}{10}(3\pi^2)^{\frac{2}{3}} \int \rho^{\frac{5}{3}}(\mathbf{r})d\mathbf{r} - Z\int \frac{\rho(\mathbf{r})}{\mathbf{r}}d\mathbf{r} + \frac{1}{2}\int\int \frac{\rho(\mathbf{r})\rho(\mathbf{r'})}{|\mathbf{r}-\mathbf{r'}|}d\mathbf{r}d\mathbf{r'} \quad (2.21)$$

Where the first term represents the kinetic energy based on uniform electrons gas and last two terms represent attractive interaction between electron-nucleus and repulsive interaction between electron-electron interaction, respectively. Here, the total energy is function of electrons density mean that how equation (2.21) provide the energy of system without considering wave function. The Thomas-Fermi model assume that, the ground state energy of system can be obtained by minimizing the equation (2.21) under the constraint of

$$N = \int \rho(\mathbf{r})d\mathbf{r} \quad (2.22)$$

2.0.5 Density Functional Theory (DFT)

The Density Functional Theory is the powerful computational quantum mechanical modeling use in physics, chemistry, and material science to investigate the electronic and magnetic properties of many-body system, particularly in atoms, molecules, and condense phases. The foundation of DFT begin with Hohenberg and Walter Kohn paper published in Physical Review in 1964 [49]. In this paper, they develop an exact variation principle for ground state energy under the consideration of density as variable function. Walter Kohn is the founding father of DFT. Then in 1998 Walter Kohn was awarded with the Novel Prize in Chemistry for his development of DFT. In DFT the complicated wave function ψ is replaced by electron density. The central idea of DFT is to describe a many-body interacting system through particle density instead of many-body wave function. The probability of finding N electrons within volume element $d\mathbf{r}$ is given by

$$\rho(\mathbf{r}) = N\int ..... \int .\psi(\mathbf{r}_1, \mathbf{r}_2....\mathbf{r}_N)^*\psi(\mathbf{r}_1, \mathbf{r}_2.....\mathbf{r}_N) \quad (2.23)$$

Where

$$N = \int \rho(\mathbf{r}) d\mathbf{r} \tag{2.24}$$

The DFT works on the firm foundation of theorem due to Pierre C. Hohenberg and Walter Kohn, known as Hohenberg-Kohn theorem (HK theorem).

2.0.6 Hohenberg-Kohn Theorem

Hohenberg-Kohn theorem is related with the system consisting revolving electron under the influence of external potential v_{ext} it stated as follow,

Hohenberg-Kohn Theorem 1

It state that, the electron operator is same for all-electron system so, the system is completely defined by number of electrons and external potential or in other hand the external potential $v_{ext}(r)$, and hence total energy is a unique functional of the electrons density $\rho(\mathbf{r})$ [50].

let us consider, the ground state electronic wave function ψ that gives an electron density $\rho(\mathbf{r})$ for an external potential $v_{ext}(\mathbf{r})$. Assume we have a second external potential $v'_{ext}(\mathbf{r})$ that has a ground state ψ' with same electrons density $\rho(\mathbf{r})$. Again, E and E' are the total energy corresponding to Hamiltonian H and H' for ground state wave function ψ and ψ', respectively. The total energies are the expectation value of Hamiltonian as below,

$$E = \langle \Psi | \, H \, | \Psi \rangle \tag{2.25}$$

$$E' = \langle \Psi' | \, H' \, | \Psi' \rangle \tag{2.26}$$

Here, ψ' is not ground state wave function for Hamiltonian H'. Then,

$$\begin{aligned} E &= \langle\psi|\, H\, |\psi\rangle < \langle\psi'|\, H\, |\psi'\rangle \\ &= \langle\psi'|\, H'\, |\psi'\rangle + \langle\psi'|\, (H - H')\, |\psi\rangle \\ &= E' + \int [v_{ext}(\mathbf{r}) - v'_{ext}(\mathbf{r})]\rho(\mathbf{r})d\mathbf{r} \end{aligned} \tag{2.27}$$

Similarly, prime and un-prime are reversed, then we get

$$E' < E + \int [v'_{ext} - v_{ext}]\rho(\mathbf{r})d\mathbf{r} \tag{2.28}$$

Adding equation (2.27) and (2.28), we get

$$E + E' < E' + E \tag{2.29}$$

This lead to contradict the above statement. So, the external potential $v_{ext}(\mathbf{r})$ must be unique functional for ground state electrons density. Also, the wave function is determined by the external potential and therefore wave function must also be unique functional of electron density $\rho(\mathbf{r})$. If we calculate the Hamiltonian of system as sum of kinetic energy (T) and electron-electron interaction term (V_{ee}) i.e

$$H = T + V_{ee} \tag{2.30}$$

then there must exit the universal functional as a function of electrons density

$$F[\rho(\mathbf{r})] = T[\rho(\mathbf{r})] + V_{ee}[\rho(\mathbf{r})] \tag{2.31}$$

From equation (2.31), we can say that universal functional entirely depends on electrons density. Then, the energy functional $E[\rho(\mathbf{r})]$ can be expressed in term of external potential v_{ext} and universal density functional $[\rho(\mathbf{r})]$ which is independent of the external

potential $v_{ext}(\mathbf{r})$ such that

$$E[\rho(\mathbf{r})] = \int v_{ext}(\mathbf{r})\rho(\mathbf{r})d^3\mathbf{r} + F[\rho(\mathbf{r})] \tag{2.32}$$

Hohenberg-Khon Theorem 2

It state that, the ground state energy can be obtain from variationally: the density that minimizes the total energy is the exact ground state density [50]. The electron density which determine v_{ext}, N, and v_{ext} determine $\hat{H}$ and ψ. It implies ψ is function of $\rho(\mathbf{r})$. For system having ground state electron density $\rho(\mathbf{r})$, the total energy of system is given by

$$E = \langle\psi| H |\psi\rangle \tag{2.33}$$

Again, let we assume different electrons density $\rho(\mathbf{r})$ corresponding to wave function ψ'. According to variational principle, the energy of system is greater than that of ground state energy i.e

$$E < \langle\psi'| H' |\psi'\rangle = E' \tag{2.34}$$

Therefore, the total energy functional $E[\rho(\mathbf{r})]$ gives the exact ground state energy only for the exact ground state density. If the universal functional of system is known for the system, then total energy in equation (2.33) can be minimize with respect to electrons density $\rho(\mathbf{r})$ and exact ground state electrons density and energy would be found.

2.0.7 Kohn-Sham Approach

Kohn- Sham approach to the problem consider the many body problem with non interacting particles where total wave function of the system is given by Slater determinant in accordance with the **Hartree-Fock approximation**. Two separate systems containing interacting and non interacting particles are considered which have same particle density in ground state. In Kohn-Sham equations, the exchange and correlation portions of the chemical potentials of a uniform electron gas appears as effective potential.

An approximation for $G[\rho(\mathbf{r})]$ is proposed,

$$G[\rho(\mathbf{r})] = T_s[\rho(\mathbf{r})] + E_{xc}[\rho(\mathbf{r})] \tag{2.35}$$

where $T_s[\rho(\mathbf{r})]$ is kinetic energy of the system of non interacting electrons and $E_{xc}[\rho(\mathbf{r})]$ is exchange and correlation energy of an interacting system with density $\rho(\mathbf{r})$. So,

$$E[\rho(\mathbf{r})] = \int v(\mathbf{r})\rho(\mathbf{r})\, d^3r + \frac{1}{2}\int \frac{\rho(\mathbf{r})\rho(\mathbf{r}')}{|\mathbf{r}-\mathbf{r}'|}\, d^3r\, d^3r' + T_s[\rho(\mathbf{r})] + E_{xc}[\rho(\mathbf{r})] \tag{2.36}$$

so we write,

$$E[\rho(\mathbf{r})] = V[\rho(\mathbf{r})] + U_H[\rho(\mathbf{r})] + T_s[\rho(\mathbf{r})] + E_{xc}[\rho(\mathbf{r})] \tag{2.37}$$

where $U_H[\rho(\mathbf{r})]$ is the **Hartree energy** stated in equation (2.37). The minimization of energy as asserted by **Hohenberg-Kohn theorem** yields the correct ground density. The procedure is as follows:

$$\frac{\delta E[\rho(\mathbf{r})]}{\delta\rho(\mathbf{r})} = 0 = \frac{\delta V[\rho(\mathbf{r})]}{\delta\rho(\mathbf{r})} + \frac{\delta U_H[\rho(\mathbf{r})]}{\delta\rho(\mathbf{r})} + \frac{\delta E_{xc}[\rho(\mathbf{r})]}{\delta\rho(\mathbf{r})} + \frac{\delta T_s[\rho(\mathbf{r})]}{\delta\rho(\mathbf{r})}$$

so

$$0 = \frac{\delta T_s[\rho(\mathbf{r})]}{\delta\rho(\mathbf{r})} + v(\mathbf{r}) + v_H(\mathbf{r}) + v_{xc}(\mathbf{r}) \tag{2.38}$$

where, $v_{xc}(\mathbf{r})$ is called the exchange-correlational potential. Now, considering a system of N non interacting particles in potential $v_s(\mathbf{r})$ where minimization condition for ground state energy is

$$0 = \frac{\delta E_s[\rho(\mathbf{r})]}{\delta\rho(\mathbf{r})} = \frac{\delta T_s[\rho(\mathbf{r})]}{\delta\rho(\mathbf{r})} + \frac{\delta U_s[\rho(\mathbf{r})]}{\delta\rho(\mathbf{r})}$$

Here, $E_s[\rho(\mathbf{r})]$ is the ground state total energy of non interacting particles. Which can be written as

$$0 = \frac{\delta T_s[\rho(\mathbf{r})]}{\delta\rho(\mathbf{r})} + v_s(\mathbf{r}) \tag{2.39}$$

Let $\rho_s^o(\mathbf{r})$ and $\rho_v^o(\mathbf{r})$ be ground state densities for non-interacting and interacting system of particles respectively.

$$v_s(\mathbf{r}) = v(\mathbf{r}) + v_H(\mathbf{r}) + v_{xc}(\mathbf{r}) \tag{2.40}$$

So, single body Schrodinger equation for a particle in non interacting system in potential $v_s(\mathbf{r})$ is

$$[\frac{-\hbar^2}{2m_e}\nabla^2 + v_s(\mathbf{r})]\phi_i(\mathbf{r}) = \epsilon_i\phi_i(\mathbf{r}) \tag{2.41}$$

so that $E_s[\rho(\mathbf{r})] = \sum_{i=1}^{N} f_i\epsilon_i$ and,

$$\rho_s^o(\mathbf{r}) = \sum_{i=1}^{N} f_i|\phi_i(\mathbf{r})|^2 = \rho_v^o(\mathbf{r}) \tag{2.42}$$

The equations (2.40), (2.41), and (2.42) are called Kohn-Sham equations which replace the problem of minimizing $E[\rho(\mathbf{r})]$ by that of solving a Schrodinger wave equation of non-interacting particles. Starting with initial guess of $\rho(\mathbf{r})$ we calculate the corresponding $v_s(\mathbf{r})$ as it is functional of $\rho(\mathbf{r})$ then solving differential equation for $\phi_i(\mathbf{r})$ yields new $\rho(\mathbf{r})$. Again, the process is continued until self consistency is obtained. Final expression of ground state energy will be then given as below:

$$E_o = \sum_{i=1}^{N}\epsilon_i - \frac{1}{2}\int\int \frac{\rho_v^o(\mathbf{r})\rho_v^o(\mathbf{r}')}{|\mathbf{r}-\mathbf{r}'|}\, d^3r\, d^3r' - \int v_{xc}(\mathbf{r})\rho_o(\mathbf{r})\, d^3r + E_{xc}\rho[(\mathbf{r})] \tag{2.43}$$

$E_{xc}[\rho(\mathbf{r})]$ is a functional of spin densities $n_\downarrow$ and $n_\uparrow$. Since the exact dependence of $E_{xc}\rho[(\mathbf{r})]$ upon $\rho_\downarrow$ and $\rho_\uparrow$ is not known, these equations do not predict the correct ground state and spin densities of the many electron system. So, $E_{xc}\rho[(\mathbf{r})]$ must approximated by the exchange-correlational functional [50].

Exchange Correctional Functional

The KS equation is able to explained the exactly contribution of electronic energy of atomic or molecular energy of the system including the major portion of the kinetic

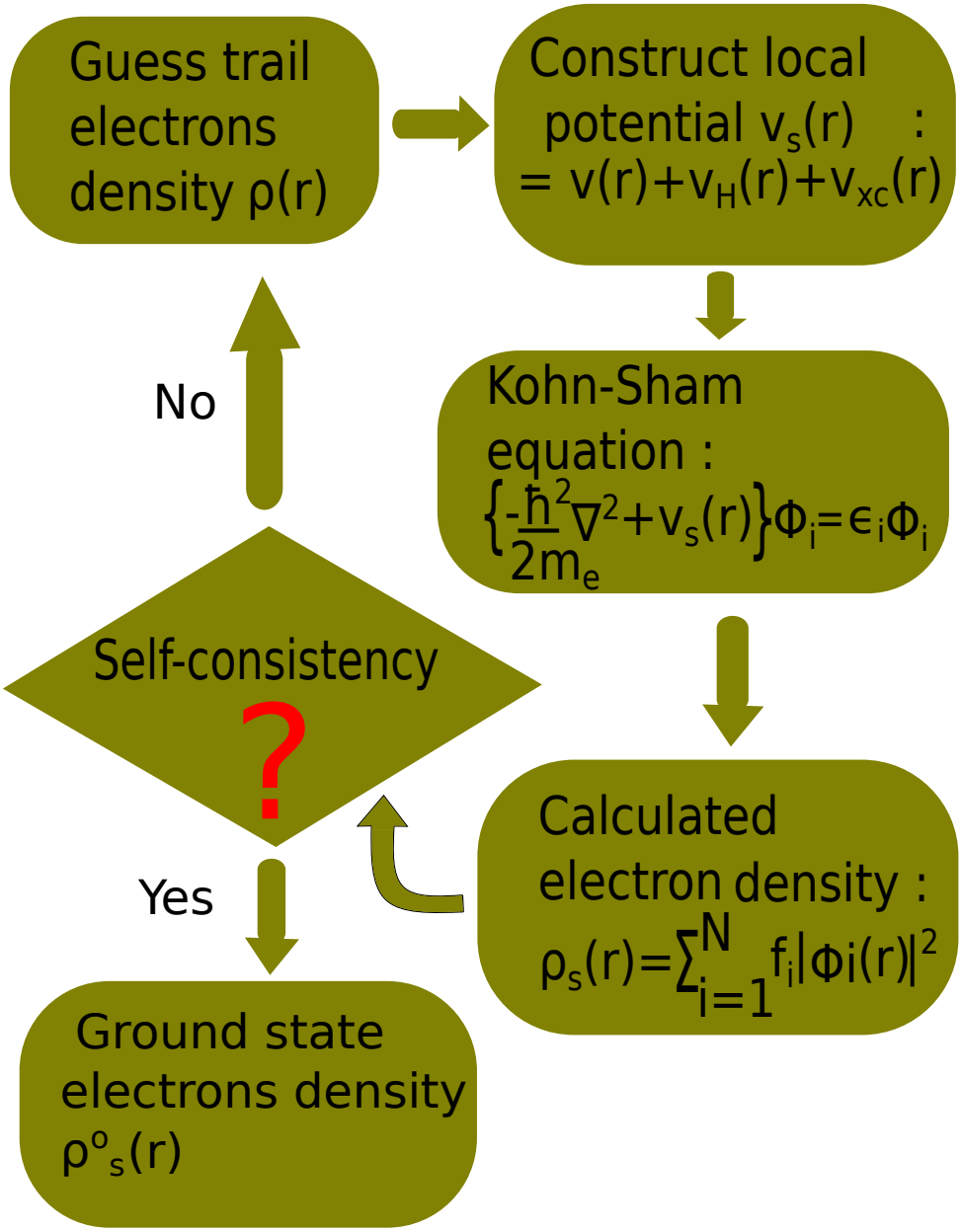

Figure 2.1: Schematic algorithm to solve Kohn-Sham equation.

energy. The remaining unknown term are collectively called the exchange correlation energy functional $E_{xc}\rho[\mathbf{r}]$. The KS equation also explicitly succeed to explain the correct ground states electrons density by considering the interacting and non-interacting systems. The unknown exchange correlation energy functional $E_{xc}\rho[\mathbf{r}]$ in KS equation include the quantum-mechanical Pauli and Coulomb correlations and the other of the correlation-kinetic effects. The quality of the DFT approaches hinges solely on selection of approximation for $E_{xc}\rho[\mathbf{r}]$. Some of the ways of approximating exchange-

correlational functional are explain briefly as follows,

2.0.8 Local Density Approximation (LDA)

In this section, we consider uniform electrons gas, where the negatively charge electrons are moving on the uniform positive background charges distribution such that the ensemble is electrically neutral and all virtually approximated exchange correlation functionals are based on this consideration. The number of electrons and volume of this considered system approach to infinity, where the electrons density $\rho = \frac{N}{V}$ is finite and constant value at everywhere. This uniform electrons gas model is the good approximation of the metal such as sodium, where the electrons are smeared out the core part forming the uniform positive back ground charge. However, this approximation is quite far good approximation for realistic situation like in atom or molecules, which is characterized by rapidly varying electrons densities. The reason why the uniform electron gas has such a prominent place in DFT to calculate unknown term present in KS formulation. So, LDA is good approach for uniform electron gas to understand exchange and correlation energy functionals exactly or at least to very high accuracy.

$$E_{xc}^{\mathrm{LDA}}[\rho(\mathbf{r})] = \int \rho(\mathbf{r})\epsilon_{xc}(\rho(\mathbf{r}))\, d^3r$$

Where, $\epsilon_{xc}(\rho(\mathbf{r}))$ is the exchange-correlation energy per particle of a uniform electron gas of density $\rho(\mathbf{r})$. This energy per particle is weighted with the probability $\rho(\mathbf{r})$. The exchange-correlation energy can be split into two separate part as follow, ϵ_{xc} = $e_x\rho(\mathbf{r})$ + $e_c\rho(\mathbf{r})$ The first term is exchange and second is correlation part respectively. The exchange part ϵ_x represent the exchange energy of an electron in uniform electrons gas in particular electrons density $\rho(\mathbf{r})$ have the form

$$\epsilon_x(\rho(\vec{r})) = -\frac{3}{4}\sqrt[3]{\frac{3\rho(\vec{r})}{\pi}}\,. \tag{2.44}$$

This exchange functional is frequently called Slater exchange. No any explicit expression is available for correlation part. However, highly accurate numerical quantum

Monte-Carlo simulations for homogeneous electrons gas available for correlation part. The preceding approximate functional can be expressed in the unrestricted version, where the electrons density is replaced by two spin densities $\rho_\alpha(\mathbf{r})$ and $\rho_\beta(\mathbf{r})$ with $\rho_\alpha(\mathbf{r})$ + $\rho_\beta(\mathbf{r})$ =$\rho(\mathbf{r})$ [51]. If we extend the LDA to the unrestricted condition, we get local spin density approximation (LSDA) have the form

$$E_{xc}^{LSDA}[\rho_\alpha, \rho_\beta] = \int \rho(\vec{r})\epsilon_{xc}(\rho_\alpha(\vec{r}), \rho_\beta(\vec{r}))\, d\vec{r} \tag{2.45}$$

.

2.0.9 Generalized Gradient Approximation (GGA)

The LDA is insufficient for most application in materials science. To overcome the insufficiency in LDA, GGA was introduced. The GGA is not only give the information about density of an electron at particular position **r**, but also supplement the density with information about the gradient of the charge density $\nabla\rho(\mathbf{r})$ in account the inhomogeneity in the electron density. Now, we consider the expression with ρ and ρ' for α and β spins,

$$\begin{aligned} E_{xc}^{GEA}[\rho_\alpha, \rho_\beta] = &\int \rho\epsilon_{XC}(\rho_\alpha, \rho_\beta)\, d\vec{r} \\ &+ \sum_{\sigma,\sigma'} \int C_{xc}^{\sigma,\sigma'}(\rho_\alpha, \rho_\beta) \frac{\nabla\rho_\sigma}{\rho\sigma^{2/3}} \frac{\nabla\rho_{\sigma'}}{\rho\sigma'^{2/3}}\, d\vec{r} + \ldots \end{aligned} \tag{2.46}$$

This form of functional is known as gradient expansion approximation (GEA). It is applicable for the modern system where the electrons density slowly varying. Unfortunately, we used this approximation for real molecular system, it does not lead to desired improved accuracy and frequently gives the result worse than simple LDA. The reason behind this failure is that the exchange-correlation hole associated with a functional (2.46) has lost many of the properties which made the LDA hole physically meaningful. The sum rules does not applied and exchange hole is not restricted to be negative for any pair. The dependence between the depth of the on-top hole and its extension

is lost and the holes as well as the corresponding exchange-correlation energies will provide significant error. This problem was solved by enforcing the restrictions for the true holes and also, for the hole of the beyond LDA functionals. The Functionals that include the gradients of the charge density and where the hole constraints have been restored are collectively known as generalized gradient approximations (GGA) [51]. In general, the functional underling this approximation can be expressed as

$$E_{XC}^{GGA}[\rho_\alpha, \rho_\beta] = \int f(\rho_\alpha, \rho_\beta, \nabla\rho_\alpha, \nabla\rho_\beta)\, d\vec{r} \tag{2.47}$$

2.1 Computational Details and Experimental Information

This study uses the DFT in conjunction with pseudo potential plane wave method. To describe exchange-correlation potential, Perdew-Burke-Ernzerhof (PBE) [52] within the generalized gradient approximation (GGA) has been used, where scalar relativistic pseudo potential for collinear calculation and fully-relativistic pseudo potential for non-collinear calculations are considered. The projected augmented wave (PAW) method is used to describe the ion-electron interaction [53], with $1s^1$, $2s^2\ 2p^3$, $2s^2\ 2p^4$, $2s^2\ 2p^5$, $3s^2\ 3p^1$, and $4s^2\ 3d^2$ treated as valence electrons for H, N, O, F, Al, and Ti, respectively. A plane wave basis set with a sufficient cutoff energy of 680 eV has been considered to represent valence electrons and 6800 eV for charge density, which are sufficient for these class of materials [1]. To model 2D-lattice, we performed both bare and terminated species of $1 \times 1 \times 1$, $2 \times 2 \times 1$ and $3 \times 3 \times 1$ cells. The underlying structural optimization is performed using small k grid $4 \times 4 \times 1$ with the convergence criterion in the order of 1.0^{-5} eV / cell in energy. After full structural optimization, large vacuum space more than 17 Å along the lattice vector (c vector or z direction) was set to avoid any interaction between MXenes sheet and densed k-points grid $20 \times 20 \times 1$ was used for electronic calculations and $25 \times 25 \times 1$ for DOS calculations. DOS was calculated by onlinear tetrahedral integration method. The geometries of MXenes were relaxed

until force becomes less than or equal to 0.01 eV / cell.

Experimentally, these promising MXenes within 2D materials family also posses unique properties acquired from complex combined bonding nature and electronic structure, atomic stacking, synthesis condition, and surface termination [54]. Despite these fascinating properties and growing interest, the field lacks a systematic experimental investigation. The titanium nitride based MXenes and their derivatives are difficult to prepare due to large value of formation energy in their MAX phase and poor stability in etchant, typically in the hydrofluoric acid(HF) [22]. Experimentally, the poor structural stability of surface terminated nitride based MXenes are improved by making multi-layer structure, which has great application in biology [3]. The scanning transmission electron microscopy imaging reveals the presence of the different point defects in the single-layer $Ti_3C_2T_2$. The excellent conductivity due to point defect predicted by DFT is conformed with the help of direct electrical measurements of single- and few-layer flakes of $Ti_3C_2T_2$ [31]. The robust $Ti_3C_2T_2$/S conductive paper/sheet with excellent conductivity, unique chemisorption, and mechanical properties of lithium polysulfide shuttle was fabricated through filtration-evaporation approach. $Ti_3C_2T_2$/S paper/sheet has excellent electrochemical properties [55]. The surface de-functionalization increased the electronic conductivity through in situ vacuum annealing, electrical biasing, and spectroscopic analysis within the transmission electron microscope [56].

The available literature based on experimental and computational studies show the nitride based MXene has great attention in the next generation electronic applications. However, there is a lack of systematic investigation in Ti_2N and its derivatives. Herein, we have intensively focused the structural, electronic, magnetic, and topological properties in pristine, strained, defected, and doped systems.

2.1.1 Quantum ESPRESSO

Quantum ESPRESSO is an integrated suite of open- source computer codes for quantum simulations of materials using state-of-the-art electronic-structure techniques, based on DFT, density-functional perturbation theory, and many-body perturbation theory,

within the plane-wave pseudo potential and projector-augmented-wave approaches [57]. It was first released on 15-06-2001 named as pw.1.0.0. The program mainly written in Fortran-90 with some parts in C or in Fortran-77, was build of merging and re-engineering of different independently developed core packages, sets of packages, designed to be inter-operable with core components, that allow the performance of more advanced tasks. The important package of Quantum ESPRESSO are

- **PWscf**: **PWscf** [**P**lane-**W**ave self-consistent filed] is one core component of Quantum ESPRESSO package use to solve Kohn-Sham equation on the basis of plane wave basis sets.

- **CP**: **CP** [**C**ar-**P**arrinello] is another component of Quantum ESPRESSO package. It can perform Car-Parrinello molecular dynamics.

- **PostPro** : It is an open-source package for post processing of data produced by PWscf and CP. which allows data analysis and plotting.

- **Phonon** : It is another additional package of Quantum ESPRESSO. It implements density-functional perturbation theory for the calculation of second- and third-order derivatives of the energy with respect to atomic displacements and Nudged Elastic Band (NEB) for the calculation of reaction pathways and energy barriers.

Chapter 3

Results and Discussion

In this chapter, we have discussed the result of our present work. This chapter contain discussion of structural optimization such as convergent test, lattice parameter optimization, electronic, magnetic, and topological properties of MAX phase Ti_2AlN, bare MXene Ti_2N, and its corresponding functionlized MXene Ti_2NT_2 (T = -OH, -O, -H, -F) in $1 \times 1 \times 1$, $2 \times 2 \times 1$, and $3 \times 3 \times 1$ cells. We have also discussed the structural stability on the basis of formation and cohesive energies in different super-cells. Furthermore, we have also studied the inference of defect in stable configuration of Ti_2NO_2 with different concentrations.

3.0.1 Structural Optimization / Convergence Test

The convergence test is required to obtained the fairly accurate result with minimal computational cost. Ideally, the larger value of ecutoff energy and denser K-point grid provide better results but it take more time as well. Again, on increasing the ecutoff energy and density of K-point, the computational cost also increases. Therefore, to obtain good result with minimum computational cost and less time, we perform convergence test and optimization corresponding to K. E cutoff for plan wave function, K-points grid, and cell-dimension of the system.

According to literature review, the optimized K. E cutoff for plan wave function for bulk Ti_2AlN is enough for pristine and terminated species. So, we have just optimized

K-points grid and cell-dimension in 3D bulk MAX phase Ti_2AlN, bare and its corresponding functionalized MXenes Ti_2NT_2, where T represents surface termination (T= -OH , -H, -F, -O) separately.

3.0.2 MAX phase

K. E Cutoff for Plan Wave Function

The small K-points grid of $4 \times 4 \times 1$ is used for K. E cuttoff plan wave function optimization. Here, we have taken different value of K. E cutoff of plan wave function (ecutoff) and performed scf calculations. After completion of scf calculations, noted the corresponding total energy for different value of ecutoff energy and plot ecutoff energy verses total energy. The nature of graph is shown in FIG. 3.1. There is no sig-

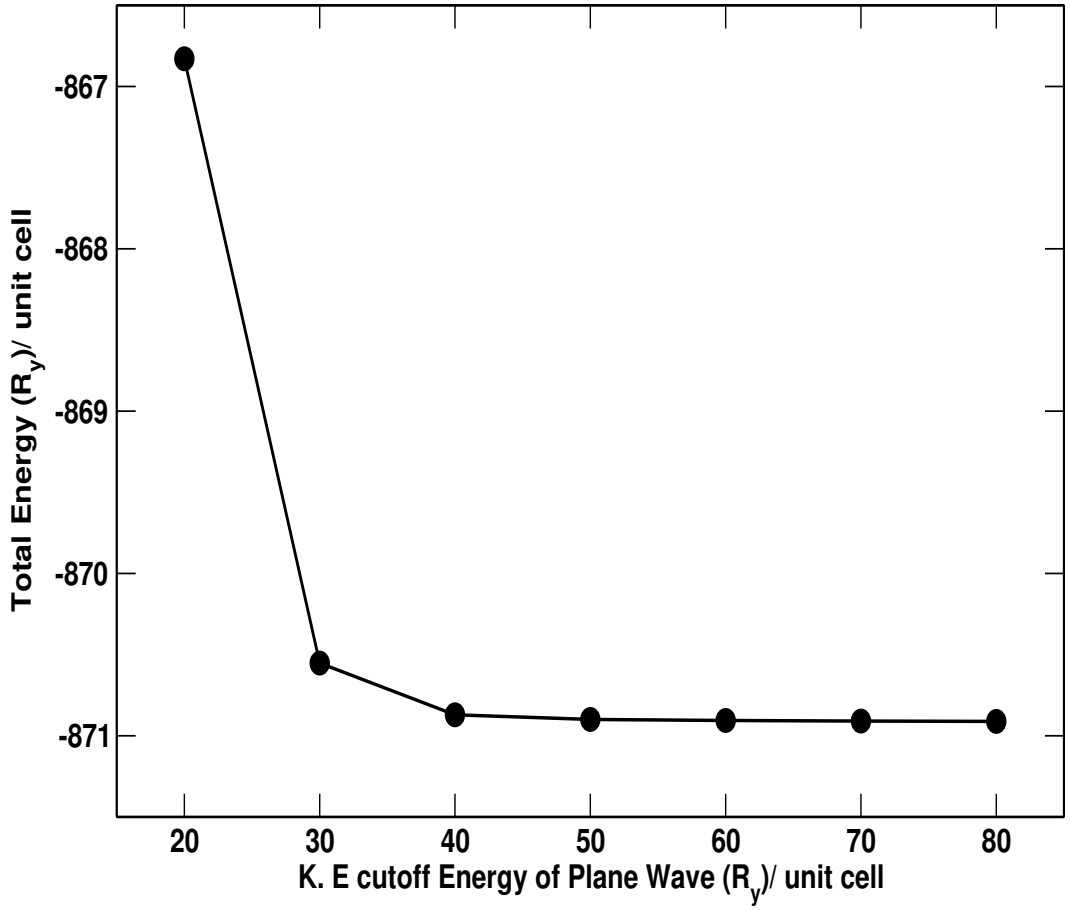

Figure 3.1: K. E cutoff for wave function vs total energy of MAX Ti_2AlN respectively.

nificant change in total energy after 50 Ry. So, we have adopted this value for further calculations.

K-points Optimization

Taking fixed value of ecutwfc (50 Ry) for different value of K-points along x, y, z direction and perform scf calculations and noted corresponding total energy. The plot of different value of K-points and total energy is shown in FIG.3.2. There is no significant

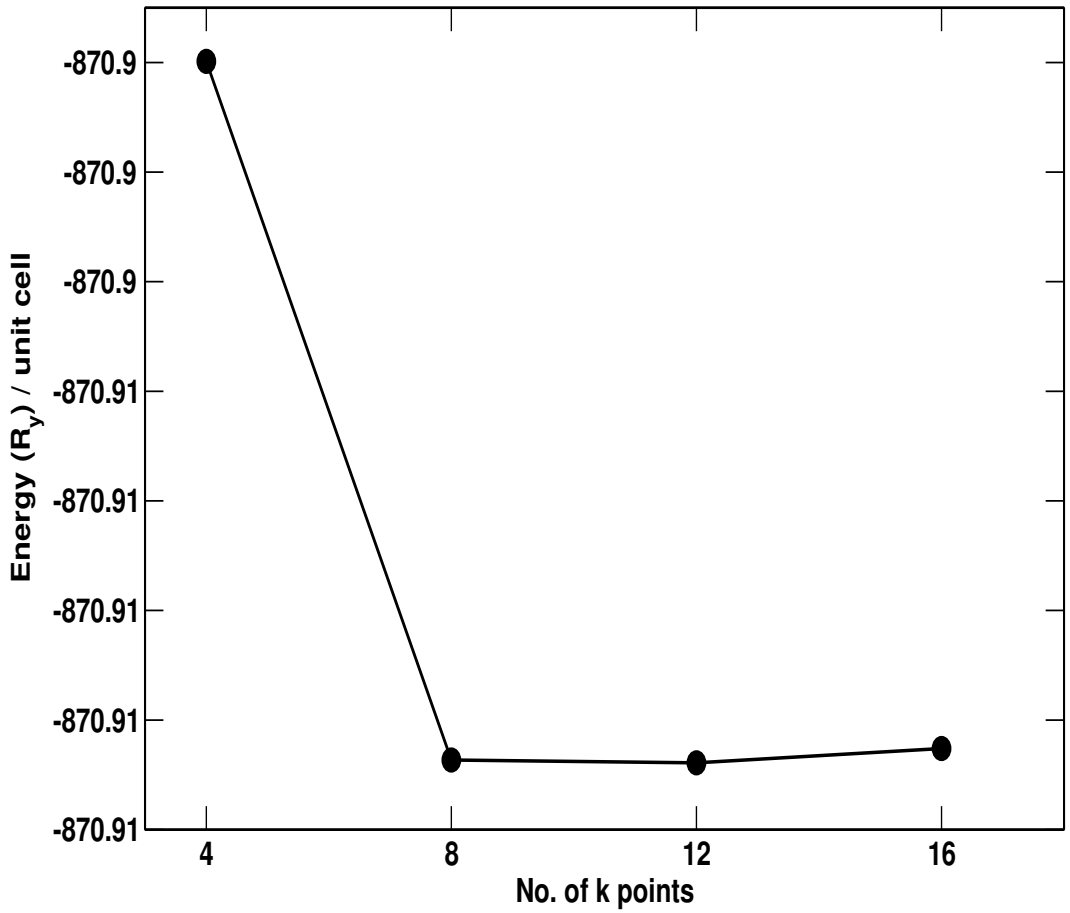

Figure 3.2: No. of K-points vs total energy of MAX Ti_2AlN.

change in total energy after $8 \times 8 \times 2$ K-points grid along x, y, and z respectively. So, we have used this value for electronic calculations in 3D MAX phase Ti_2AlN.

Lattice Parameter Optimization

We have optimized the lattice parameters of MAX phase Ti_2AlN through energy minimization process. The optimization were carried out by taking a loose K-points grid $4\times4\times1$ and optimized value of K. E for plane wave function (50 Ry). Here, we have optimized cell-dimension(1) first by varying its value for fixed value of cell-dimension(3) and corresponding total energy were noted. Similarly, for cell-dimension(3) optimiza-

tion, we have used optimized value of cell-dimension(1) as constant and varying the value of cell-dimension(3) and noted corresponding total energy. The plot of different value of cell-dimension and corresponding to total energy is shown in FIG. 3.3. From

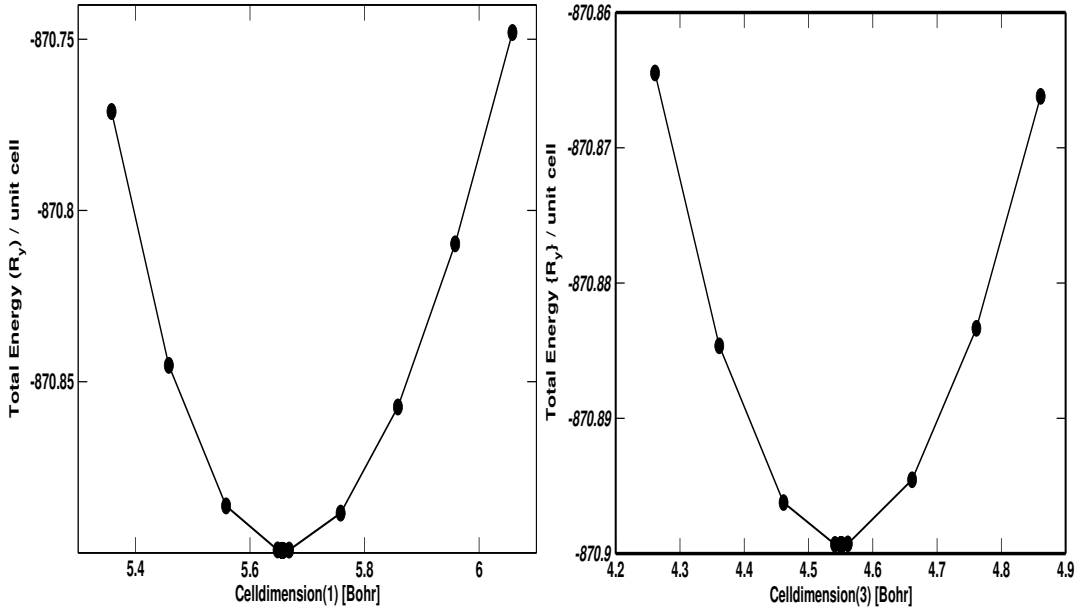

Figure 3.3: Total energy [Rydberg] vs cell-dimension(1) and cell-dimension(3)[Bohr] respectively.

above graph, we see that energy is minimum at 5.6559831 and 4.5506381 Bohr for cell-dimension(1) and cell-dimension(3) which are corresponding to 2.993 Å and 13.620 Å. Our optimized value are very nearly closed to experimental values, which are discussed below in structural stability section.

3.0.3 MXenes Ti_2NT_2 (T = -OH, -H, -O, -F)

The MXene is 2D materials obtained by selective etching for elements from MAX phase. In our case, the pristine MXene Ti_2N was obtained by etching of Al elements from parent precursor Ti_2AlN and finally terminated the MXene sheet T_2N with terminated species (T= -OH,-H, -O ,-F). The lattice parameters corresponding to pristine (Ti_2N) and functionalized MXenes ($Ti_2N(OH)_2$, Ti_2NH_2, Ti_2NO_2, Ti_2NF_2) are shown in figure below,

From above plot between cell-dimension(1) [Bohr] and total energy [Rydberg], our optimized lattice parameters are found to be 5.5947831, 5.7216831, 5.8860531, 5.9156631,

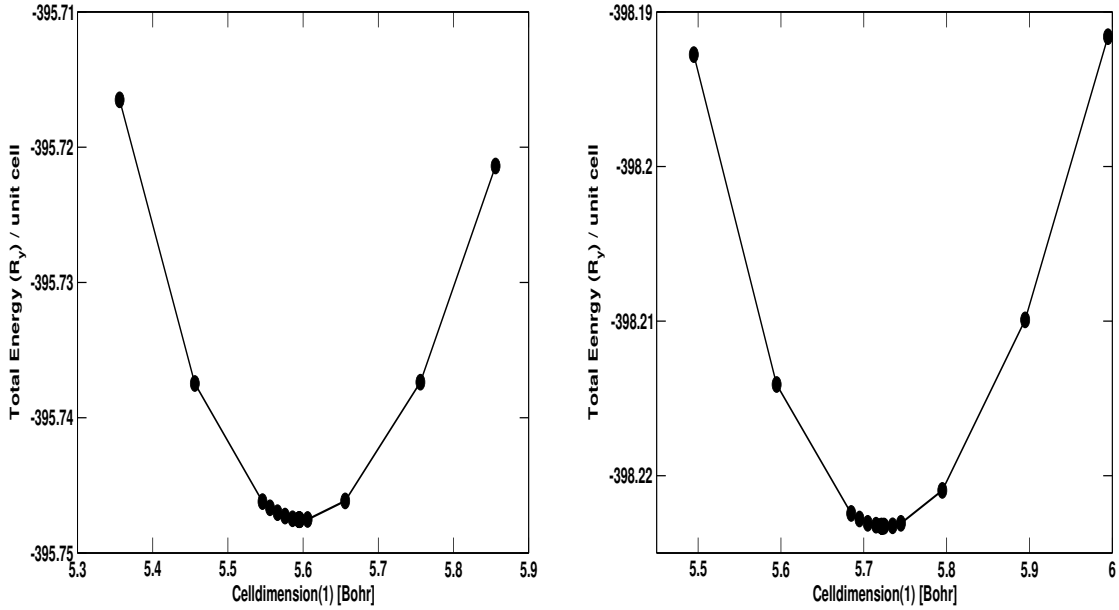

Figure 3.4: Total energy [Rydberg] vs cell-dimension(1) corresponding to pristine Ti_2N and functionalized MXene Ti_2NH_2 respectively.

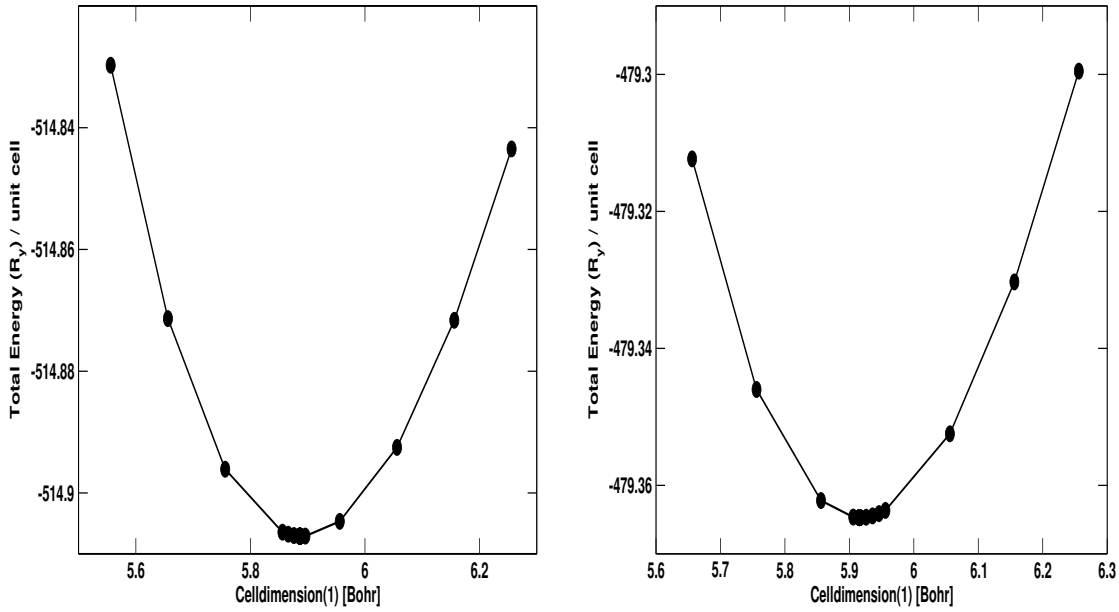

Figure 3.5: Total energy [Rydberg] vs cell-dimension(1) corresponding to functionalized MXene Ti_2NF_2 and Ti_2NO_2 respectively.

and 5.7798531 Bohr which are corresponding to 2.960 Å, 3.027 Å, 3.114 Å, 3.130 Å, and 3.058 Å for Ti_2N, Ti_2NH_2, Ti_2NF_2, Ti_2NO_2, and $Ti_2N(OH)_2$, respectively. In our DFT calculations, the optimized value of lattice parameters consistent with previous reported results (less than 1.7%) as compared to experimental value but quite larger deviation (less than 4.3%) compared with previous theoretical results. In the case of Ti_2NO_2 the optimized value of lattice parameter slightly grater than previously reported

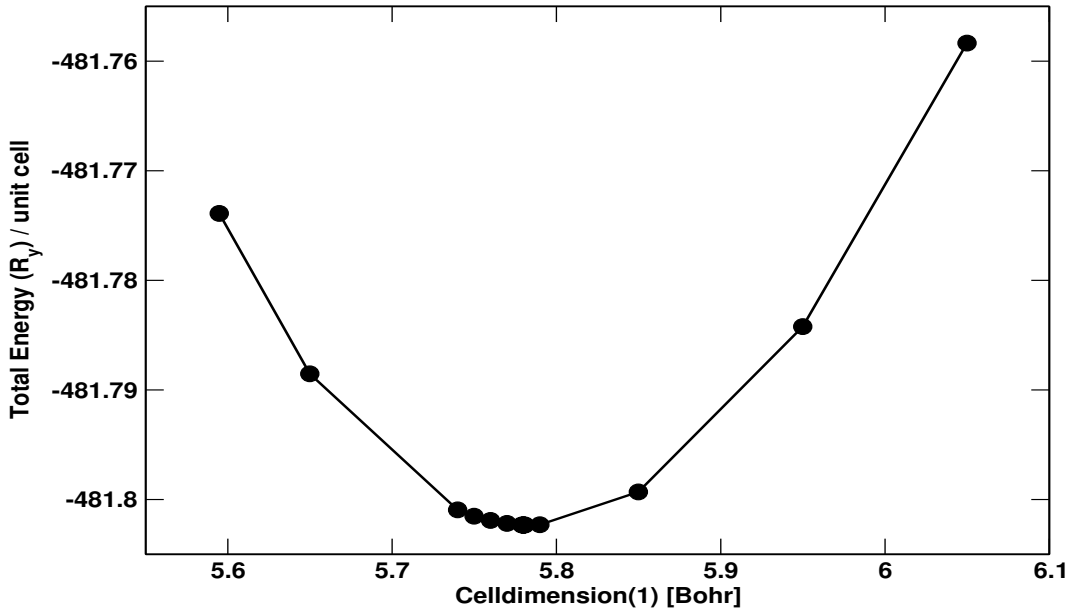

Figure 3.6: Total energy [Rydberg] vs cell-dimension(1) corresponding to functionalized MXene $Ti_2N(OH)_2$.

theoretical value of lattice parameter [1]. The comparison of optimized lattice parameters with available previous theoretical and experimental values are shown in Fig. 3.7.

3.1 Structural Stability

The 2D MXene Ti_2N is obtained by removing Al from hexagonal structure with space group number 194 ($P6_3/mmc$) of MAX phase Ti_2AlN. The MAX phase is formed due to mixed combination of ionic/covalent/metallic bonding [58] between Ti, Al, and N atoms thereby hybridizing Ti 3*d*- N 2*p*, Ti 3*d*-Al 3*s*, and Ti 3*d*- Al 3*p* states. The Al components in MAX phase are chemically reactive and the bonding between Ti and Al is purely metallic [59]. So, the relatively weak bond and reactive A element can be selectively etched with suitable chemical composition leaving behind the chemically stable closely packed MX phase Ti_2N, where the N atom filling the octahedral side of Ti_2N. The chemical exfoliation of MXene Ti_2N from MAX phase Ti_2AlN usually leaves some -O, -F, -H, and -OH on the surface, and these groups may have significant influences on the electronic and magnetic properties of MXene [15]. There are three

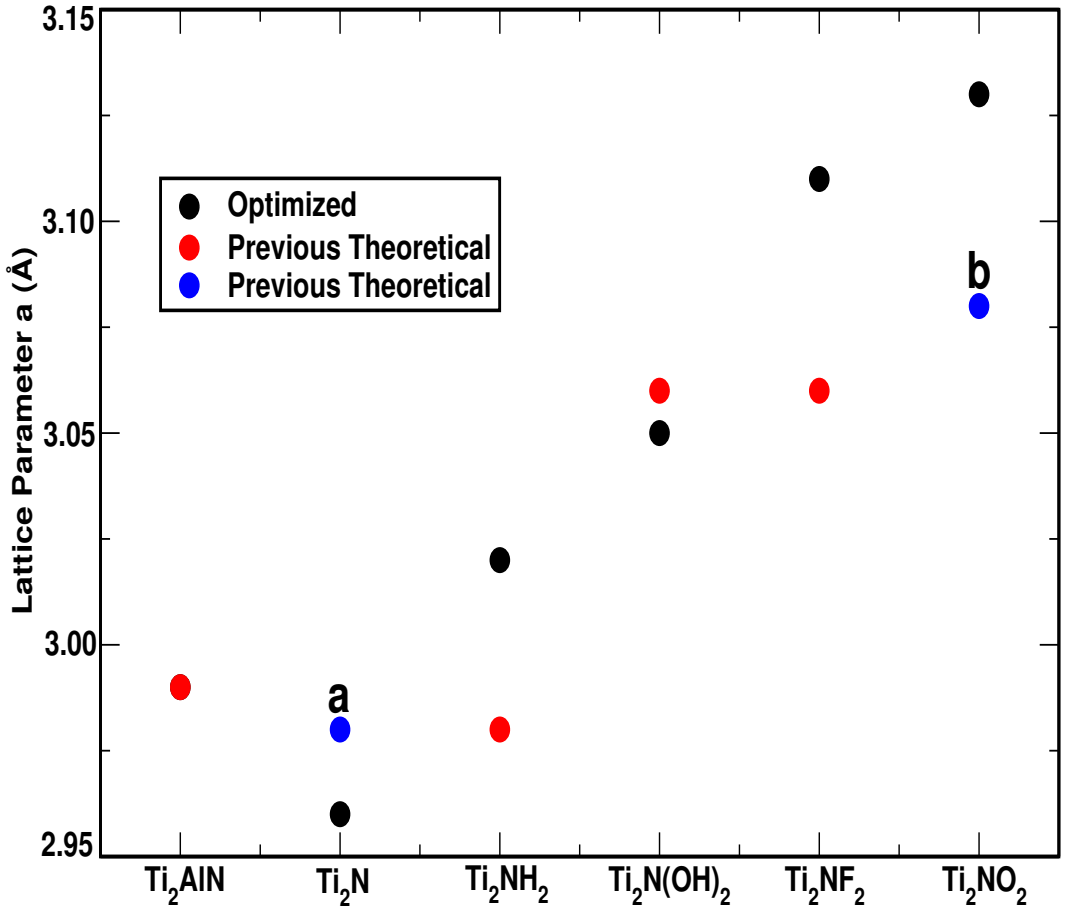

Figure 3.7: (Color online) Red [1] and blue (a [2], b [3]) small circles represent previous theoretical value, and black small circles represent optimized lattice parameters of MAX phase, and bare and its corresponding functionalized MXenes. The optimized values of lattice parameters are in fair agreement with previously reported theoretical values.

possible sites of surface termination, on the top of Ti(1) (site a), on the top of atom N (site b), and on the top of Ti(2) (site c) as shown in FIG. 3.9c. On the basis of these three sites, there are four possible configurations for the position of terminated species. In model I, at site a, in model II, at site b, in model III, at site c, and in model IV (mixed model II and III), one termination at site b and other termination at site c, are considered. The most preferential position for termination is in model III [60]. So, the terminated atoms were positioned in the model III. In the case of -OH termination, the favorable position of the hydrogen atom is on the top of oxygen atom, as a result, the structure becomes symmetrically equivalent to a mono-atom termination [44]. After surface termination, there are electronic reconstruction of new energy states between Ti atoms with terminated species.

To investigate the stability of bulk MAX phase Ti_2AlN, and bare Ti_2N and its corresponding functionalized MXenes Ti_2NT_2 (T= -OH, -H, -O, -F), the formation energy is calculated using formula,

$$E_f(Ti_2NT_2) = E_{tot}(Ti_2NT_2) - 2E_{bulk}(Ti) - E_{bulk}(N) \\ -2E_{bulk}(T) \tag{3.1}$$

Where $E_{tot}(Ti_2NT_2)$, $E_{bulk}(Ti)$, $E_{bulk}(N)$, and $E_{bulk}(T)$ represent total energy of optimized systems, bulk energies of Ti, N, and T atoms, respectively [61]. In the similar way, cohesive energy is calculated as

$$E_c(Ti_2NT_2) = E_{tot}(Ti_2NT_2) - 2E_{iso}(Ti) - \\ E_{iso}(N) - 2E_{iso}(T) \tag{3.2}$$

Where $E_{tot}(Ti_2NT_2)$, $E_{atm}(Ti)$, $E_{atom}(N)$, and $E_{atom}(T)$ represent total energy of optimized systems, energies of isolated Ti, N, and T atoms, respectively. The energy of isolated atoms are calculated by adding single atom at the center of defined large supercell [3]. From FIG. 3.8, the negative value of cohesive and formation energies indicate

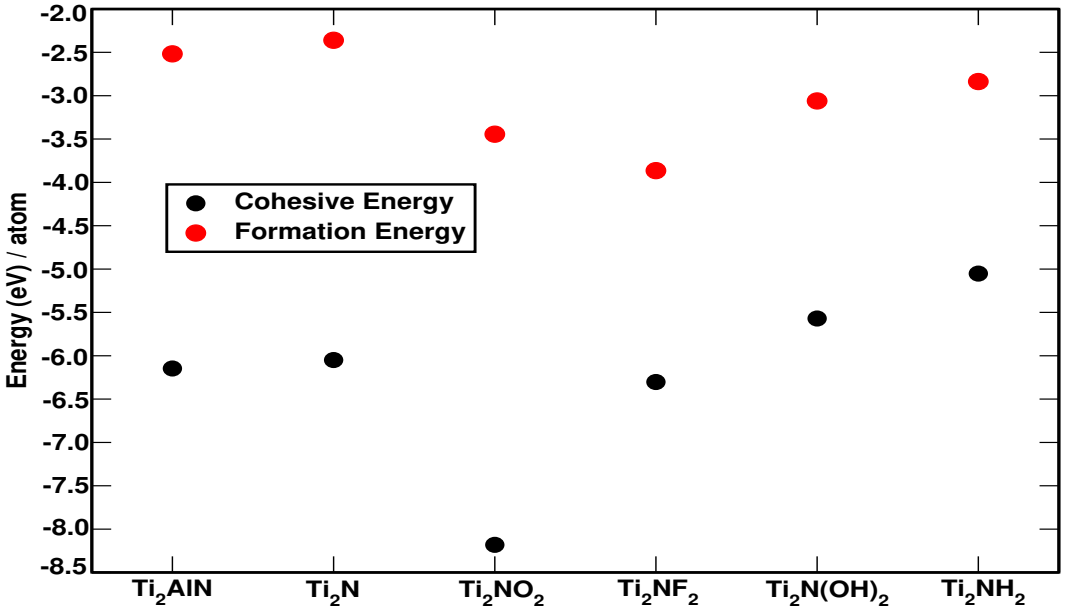

Figure 3.8: (Color online) Formation and cohesive energies per atom of MAX phase, and bare and its corresponding functionalized MXenes mono-layers. The negative values show the chemical stability of all MXenes and MAX phase. The oxygen terminated MXene mono-layer is the most stable among all other MXenes and MAX phase.

that our systems are stable and the oxygen terminated MXene is found to be relatively more stable as compared to all other MXenes and MAX phase. This is mainly due to the strong hybridization between Ti-3*d* and O-2*p* atoms. The formation energy is very large as compared to cohesive energy of nitride based MXenes, which is consistent with previously reported values [62]. So, it is difficult to extract nitride based MXene from its parent precursor MAX phase. From cohesive energy curve, the stability increase in the sequence, $Ti_2NH_2 < Ti_2N(OH)_2 < Ti_2N < Ti_2AlN < Ti_2NF_2 < Ti_2NO_2$ [2]. But this sequence is quite different for formation energy: $Ti_2N < Ti_2AlN < Ti_2NH_2 < Ti_2N(OH)_2 < Ti_2NO_2 < Ti_2NF_2$. The bare MXene is quite less stable than it's of parent precursor MAX phase (FIG. 3.8). We found that, the value of formation and cohesive energies are significantly decreased after surface termination, particularly in -O and -F groups, which indicates the functionalized MXenes are more stable than their corresponding bare MXene. The Ti_2N MXene and its derivative structures have lower formation energy than that shown in the Open Quantum Materials Database [63, 64]. Following this finding and literature, we use here the mono-layered hexagonal structure [1].

We first optimize our material systems, that makes easier to study electronic and magnetic properties. Table 3.1 shows optimized lattice parameters, thickness of mono-layers (L), bond length between titanium atom Ti and terminated species T (d_{Ti-T}), titanium-titanium atoms (d_{Ti-Ti}), and titanium to nearest atom N (d_{Ti-N}) of selected functionalized MXenes. The calculated values are compared with previously reported theoretical values (shown in parenthesis) [1].

Table 3.1: Calculated values of mono-layer thickness (L) and distance between Ti-T, Ti-Ti, and Ti-N atoms.

Crystals	L(Å)	d_{Ti-T}(Å)	d_{Ti-Ti}(Å)	d_{Ti-N}(Å)
Ti_2AlN	....	....	2.90	2.08
Ti_2N	2.31	....	2.87	2.06
Ti_2NF_2	4.57(4.63)	2.18(2.16)	2.77	2.08(2.07)
Ti_2NO_2	4.24(4.35)	2.00(1.98)	3.09	2.20(2.15)
Ti_2NH_2	4.23(4.20)	2.00, 2.01(2.00)	2.84	2.08(2.07)
$Ti_2N(OH)_2$	6.66(6.66)	2.17(2.17)	2.82	2.08(2.08)

Our optimized lattice parameters are in general consistent with the previously reported theoretical values [1]. The extracted 2D MXenes from 3D MAX phase have decreased cell size, and bond length between Ti-Ti and Ti-N. But after surface termination, the cell size and thickness of mono-layers are increased due to the addition of extra atoms in bare MXene Ti_2N. The thickness of mono-layer strongly depends on terminating species. The thin mono-layer was found in hydrogen termination while thick mono-layer was found in hydroxyl termination in bare MXene. Interestingly, the bond length between Ti-N and Ti-T in Ti_2N, Ti_2NO_2, Ti_2NF_2, and $Ti_2N(OH)_2$ follow symmetrical bond nature except for Ti_2NH_2. In hydrogen termination, Ti-T bond length of the top side is slightly shorter than that of the bottom side. But the bond length between Ti and N atoms show symmetrical nature 3.1.

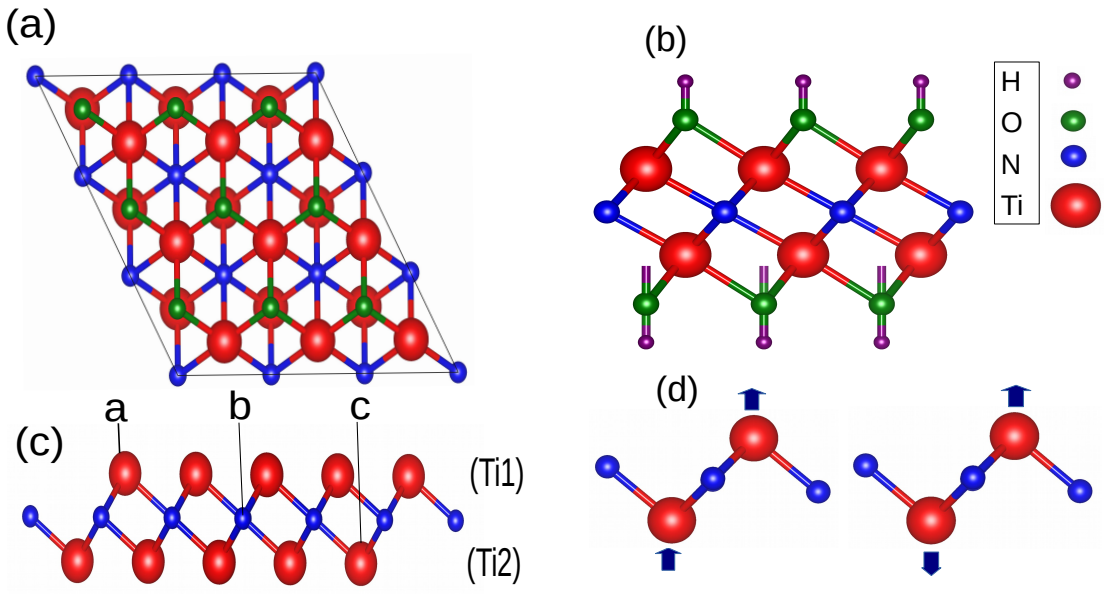

Figure 3.9: (Color online) (a) The top view of Ti_2NO_2, and (b) and (c) are side views of $Ti_2N(OH)_2$ and Ti_2N in $3\times3\times1$ super-cell, respectively, (d) the side view of mono-layer Ti_2N. The up and down arrows indicate the up and down spins in Ti_2N mono-layer.

The oxygen termination on MXene layers plays a remarkable role as compared to other terminated species. In oxygen termination, the bond length between Ti-Ti atoms increases by 0.22 Å and decreases by 0.1 Å in F termination but only slight change occurs in the case of -OH, -H terminations. Also, relatively shortest distance between d_{Ti-T} bond and longest d_{Ti-N} bond length representing strong interaction between surface of Ti and O atoms. The bond length between Ti-F is found to be larger as compared to

other terminations, which shows weak interaction between Ti and F.

The FIG. 3.9a and 3.9b represent top and side views of the optimized structure of Ti_2NO_2 and $Ti_2N(OH)_2$ in $3 \times 3 \times 1$ super-cell. The terminated atoms are filling the vacant space on the top and bottom sides of Ti layers forming alternate position with titanium atoms in the stable configuration as shown in FIG. 3.9b.

3.2 Electronic Properties

3.2.1 Band Structure

The electrons in an isolated atom occupy atomic orbitals having discrete energy level. When two or more atoms are combine together to form molecule, where their atomic orbitals are overlap. Now, according to Pauli exclusion principle , 'no two electrons have same quantum umber in a molecule. So, if two identical atoms are combined to form diatomic molecule. Their atomic orbital splits into two different molecular orbitals of different energy by allowing the electrons in former atomic orbitals to occupy the new orbital structure without having same energy. Similarly, if N identical atoms are combined to form solid, their atomic orbitals overlap. Due to Pauli exclusion principle, each atomic orbitals splits into N discrete molecular orbitals with different energy levels. If larger number of atoms ($N \approx 10^{22}$ or greater) are join together,the number of orbitals are very large and they formed very closely spaced in energy(order of 10^{-22}eV). So, the energy of adjacent levels are very closed together considered as continuum, an energy band.

The electrons in an solid forming energy bands. So the study of the energy level in solid is important to get insight information about Solid and Condensed matter Physics. On the basis of energy bands, main importantly solid is classified as three categories, Conductor, Semi-conductor, and Insulator. This classification is entirely depend upon types of bands structure form by arrangement of electrons in solid. In solid their are mainly three type of bands, Valence band, Conduction band, and Forbidden band or forbidden gap as in FIG. 3.10,

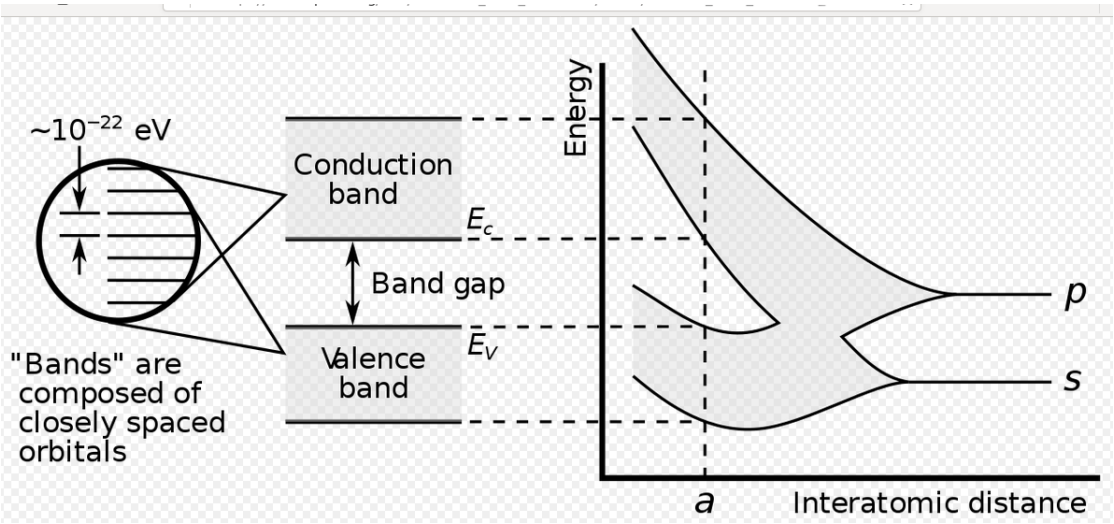

Figure 3.10: Classification of bands in solid [4]

Valence Band

The valence bands is the bands of electrons formed by group of valence electrons that can jump to conduction bands when it's excited. The valence electrons are simply the outermost electrons orbital of an atom. This is closely related to the characteristic of valence electrons.

Conduction Band

The conduction band is the band of electron orbitals that electrons can jump from the valence band when it's excited. When the electrons are in this orbitals, it has enough energy to move freely in the material. This movement of electrons generate an electric current in the materials. But at absolute zero temperature, it is completely unoccupied states.

Forbidden Band or Forbidden Gap

The forbidden gap is also called energy band. In this band there are no any states exit. It is actually bands gap between top of valence band and bottom of the conduction band in insulator and semi-conductor. The magnitude of the forbidden gap is depend up on the amount of energy required to jump electrons from valence band where electrons are bound by nucleus to conduction band where electrons get free. In case of semi-

conductor it is very small value but for insulator it become very high as compare to semi-conductor.

In our study, we calculated the electronic band structure of MAX phase Ti_2AlN, bare and it's corresponding functionalized MXene using Qunatum ESPRESSO code. The calculations were carried out along G-M-K-G path in first Brillouin zone as in FIG. 3.11.

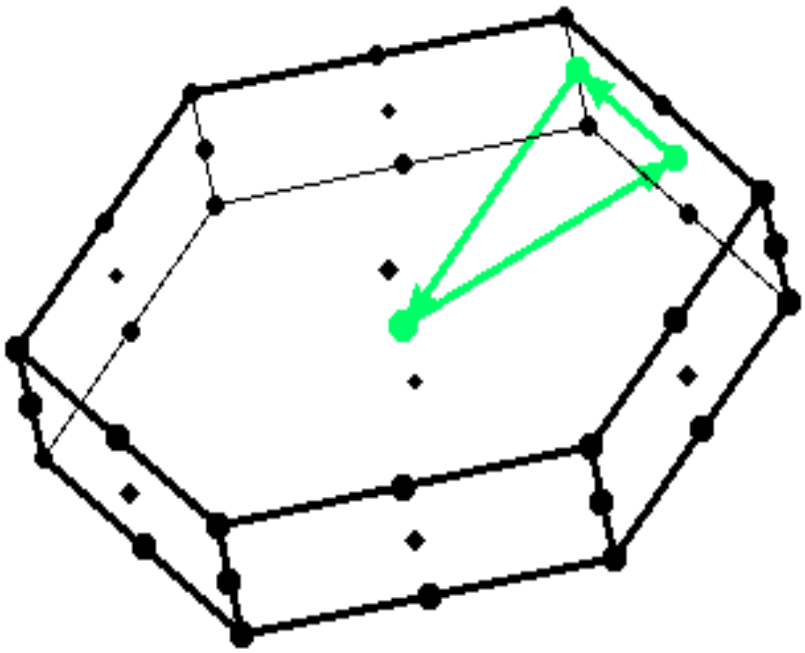

Figure 3.11: Selection of high-symmetry points (G-M-K-G) for hexagonal structure in first Brillouin zone.

3.2.2 Electronic and Magnetic Properties Without Vacancy Defect

The energetically stable configurations of MAX phase, bare MXene and its corresponding functionalized MXenes have been studied with the full relaxed calculations corresponding to possible NM, FM, and AFM configurations. The MAX phase is energetically stable in NM configuration. In the case of bare MXene, the relaxation calcula-

tions with AFM configuration show zero net total magnetization with 0.33 μ_B magnetic moment for individual Ti atoms. Similarly, the relaxation calculations with FM configuration show total magnetization 1.10 μ_B per unit cell (with 0.25 μ_B magnetic moment for each Ti) which is closely comparable to 1.00 μ_B per unit cell found in ref. [62]. The energy of FM and AFM configurations with reference to NM configuration are -39 meV and -36 meV, respectively. This shows, the FM configuration is energetically more stable than the AFM configuration. We used $1 \times 1 \times 1$, $2 \times 2 \times 1$, and $3 \times 3 \times 1$ supercells to study the electronic band structure (with SOC) and the DOS without SOC. The surface termination on bare MXene mono-layer results the complete removal of magnetism except for oxygen terminated one, which is found to be 100% spin polarized half-metallic.

The overlap of the valence and the conduction bands at the Fermi level in band structure and DOS of MAX phase reveals the considerable metallic character. The bands are mainly contributed from Ti-3*d*, N-2*p*, Al-3*p*, and Al-3*s* states. The total DOS is dominated by Ti-3*d* states. The 3*s* and 3*p* states of Al, and 2*p* and 2*s* states of N forms a very large energy gap of 6.49 eV, which is consistent with previously reported value of 6.2 eV [65]. This large energy gap in valence band indicates that, there is no *sp* hybridization in Ti_2AlN. The value of DOS near the Fermi level N(E_F) is 2.74 states per eV, which is also consistent with the previously reported value of 3.03 states per eV [66].

To illustrate the electronic properties vividly, we divided the valence band into two sub-bands of A and B as shown in FIG. 3.12Q. In the sub-band A, there is a strong contribution from Ti-3*d* and Al-3*p* states. Similarly, in the sub-band B, the strong contributions are from the Ti-3*d* and N-2*p* states and weak contributions are from the Al-3*s* states. So, the Ti-3*d* states play a significant role in both sub-bands A and B. The presence of SOC does not influence these outcomes.

On moving from 3D bulk states (Ti_2AlN) to 2D surface states (Ti_2N), there are myriad changes in the electronic structure properties from metallic to nearly half metallic [62] with topological characters. Interestingly, at the region between high symmetry points

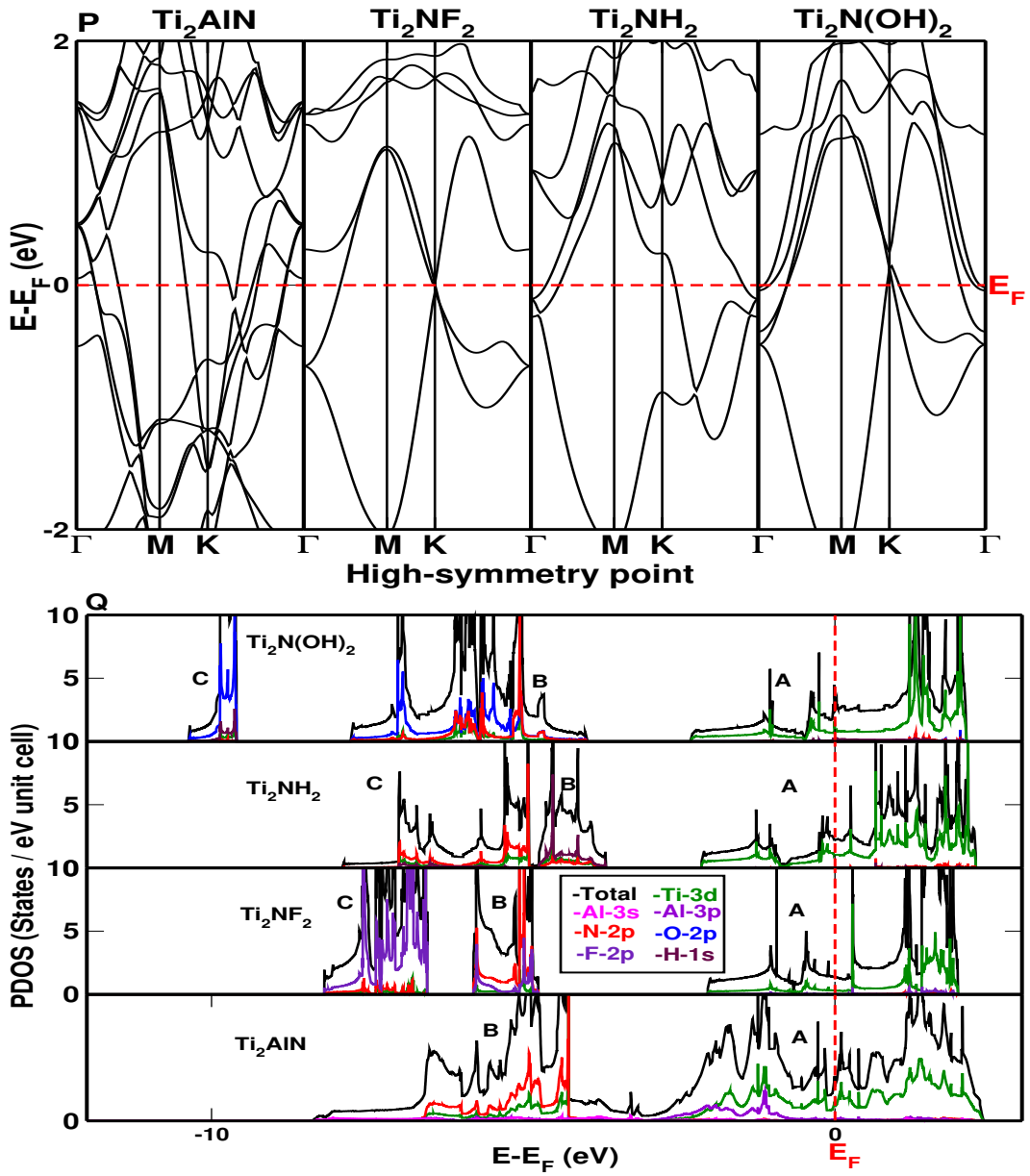

Figure 3.12: (Color online) P and Q represent the band structure and partial density of states (PDOS) of MAX phase Ti_2AlN and functionalized MXene Ti_2NT_2 (T = -F, -H, -OH) mono-layers. The red dash lines represent the position of the Fermi level in the electronic band structure and PDOS.

of K and Γ, there are two distorted Dirac cones (a) and (b) below the Fermi level in spin up channel and two distorted Dirac cones (c) and (d) above the Fermi level in spin down channel as shown in FIG. 3.13P. The formation of distorted Dirac cone apparently diminishes the characteristic of quantum oscillation [42]. The formation of Dirac cone (b) just below the Fermi level reveals the idea of n-type self doping character informing the presence of electron carriers even without transforming the electrons from surrounding environment [38]. The spin down bands show metallic character whereas

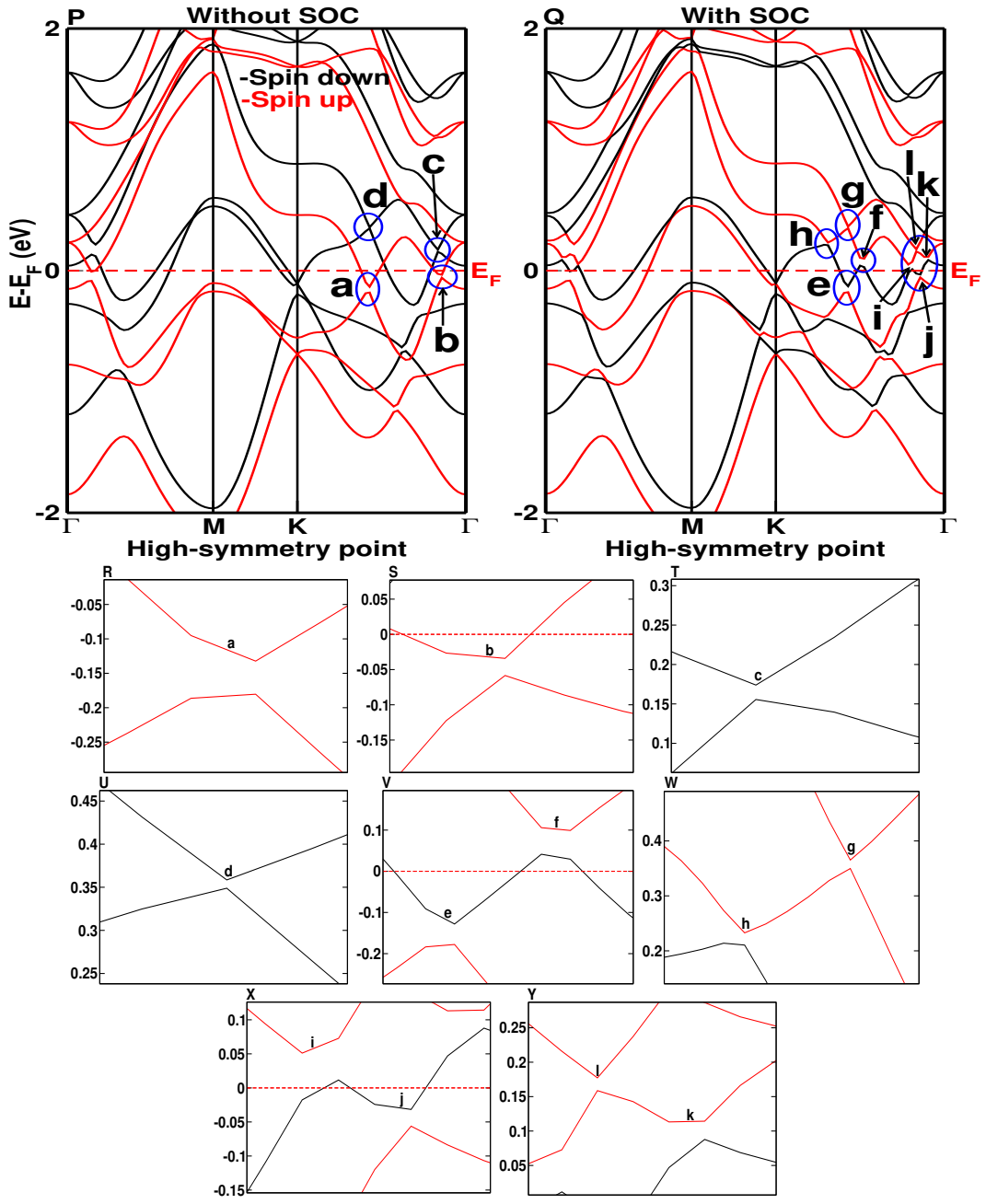

Figure 3.13: (Color online) P and Q represent the spin polarized band structure correspond to without SOC and with SOC of bare MXene Ti_2N mono-layer, respectively. R, S, T, U, V, W , X, and Y highlight the Dirac topology found in the electronic band structure. The red dash lines represent the position of the Fermi level in the electronic band structure.

the spin up bands show nearly half-metallic character. This indicates that Ti_2N is nearly half-metallic, which is supported by ref. [62]. The same band crosses the Fermi level multiple-times forming multiple Dirac cones at and near the Fermi level, which reveals the characteristic of multi-nodal properties in Ti_2N [67]. The bottom of unoccupied states in the spin down and top of occupied states in the spin up channels lie just above

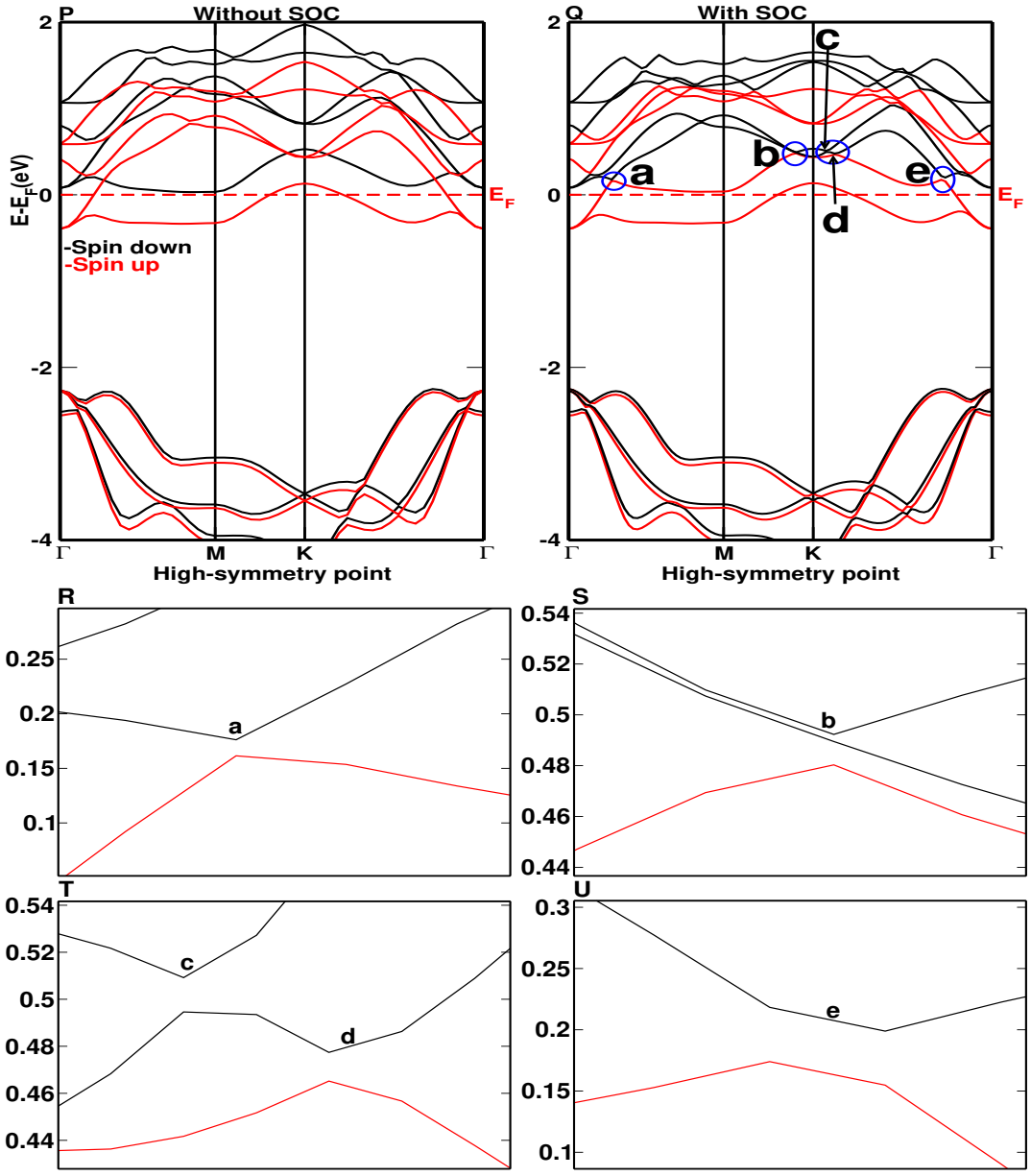

Figure 3.14: (Color online) P and Q represent the spin polarized band structure corresponding to without SOC and with SOC of oxygen terminated MXene Ti_2NO_2 monolayer. R, S, T, and U highlight the Dirac topology found in the electronic band structure. The red dash lines represent the the position of the Fermi level in the electronic band structure.

and below the Fermi level, which reveal the exchange splitting energy of 0.16 eV as shown in FIG. 3.13P [68]. This exchange splitting is caused by the 3*d* states of Ti atom clearly shown in FIG. 3.15. The noteworthy influence of SOC is found in bare MXene. The band structure corresponds to SOC in Ti_2N is shown in FIG. 3.13Q. The overlapped bands (without SOC) near the Fermi level in region Γ-M are separated and formed Dirac topological features under the presence of SOC. Interestingly, the SOC allows to make

two gapped linear Dirac cones (e) and (f) below and above the Fermi level as shown in FIG. 3.13Q. The formation of Dirac cone below the Fermi level reveals the self n-type of doping character, whereas the formation of Dirac cone just above the Fermi level reveals the self p-type doping character indicating the electrons and holes carriers even without transforming the electrons from surrounding environment [38, 42]. Similarly, the gapped linear Dirac cone (i) and gapped distorted Dirac cone (j) are found near the Fermi level (above and below) in region K-Γ as shown in FIG. 3.13Q. In the same region, the gapped distorted Dirac cones (g), (h), (k), and (l) are found above the Fermi level. The multi-nodal properties are also preserved under SOC in Ti_2N.

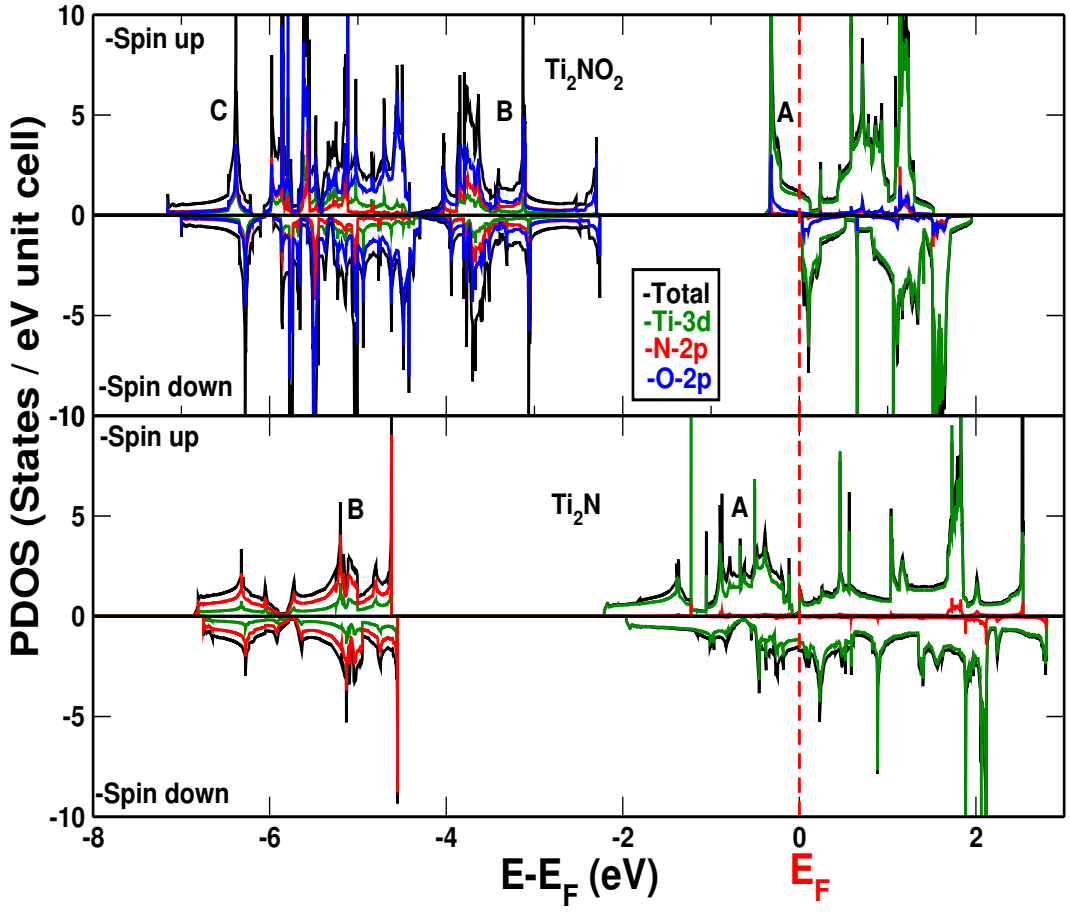

Figure 3.15: (Color online) Spin polarized PDOS of oxygen terminated MXene Ti_2NO_2 and bare MXene Ti_2N. The oxygen terminated MXene shows the half-metallic nature. The red dash lines represent the position of the Fermi level in PDOS.

Figure 3.16 shows the spin down (P) and spin up (Q) band structures of Ti_2N in $2\times2\times1$ super-cell. The bands are dispersed from M to K and Γ points in the regions above and below the Fermi level in spin down channel as shown in FIG. 3.16P. These dispersed

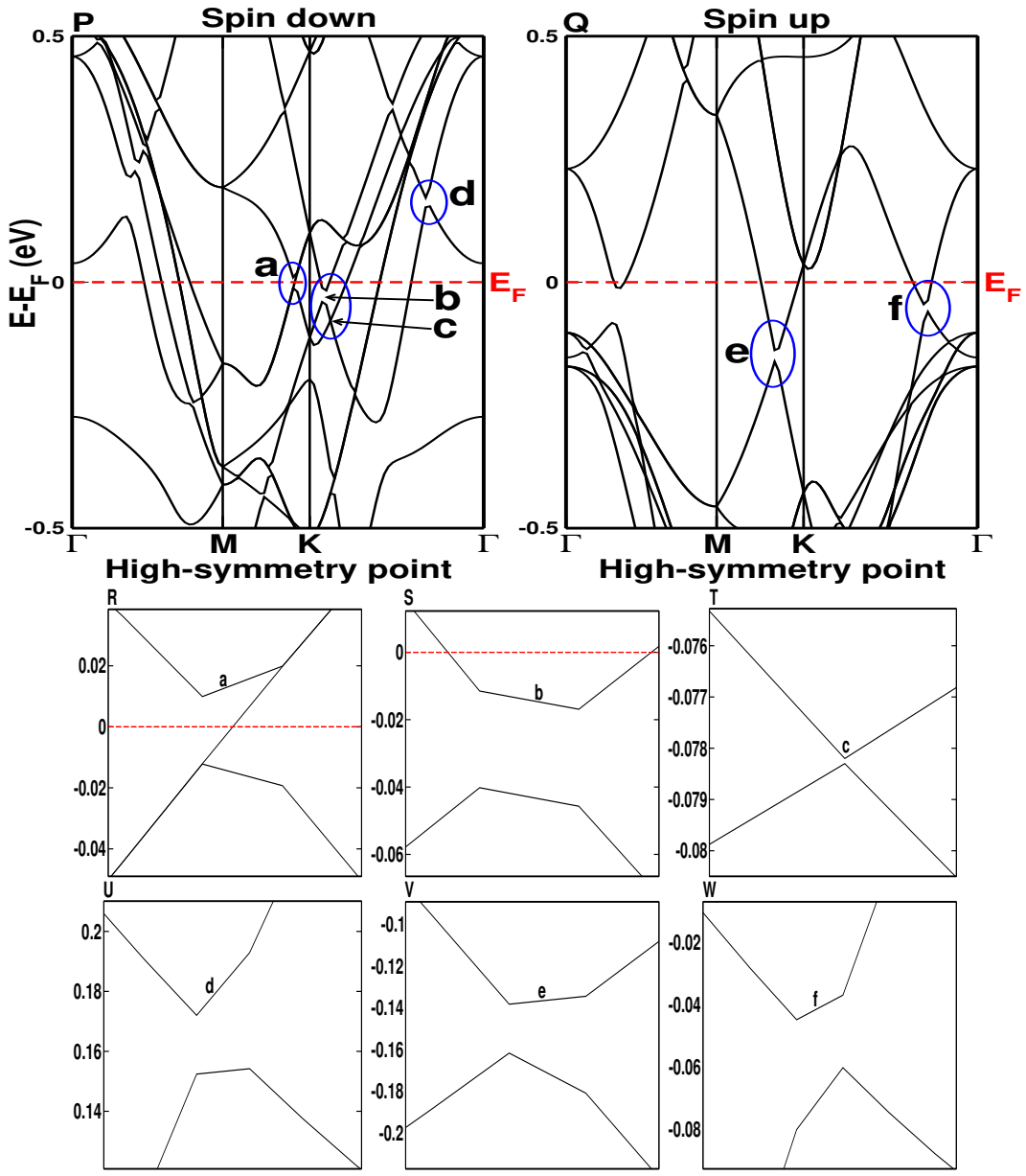

Figure 3.16: (Color online) P and Q represent the spin down and spin up band structure of MXene Ti_2N in $2 \times 2 \times 1$ super-cell respectively. R, S, T, U, V, and W highlight the open Dirac topology of bare MXene Ti_2N. The red dash lines represent the position of the Fermi level in the electronic band structure.

bands form slightly distorted linear Dirac cone in the region between M-K above the Fermi level. Interestingly, a linear distorted gapped Dirac cone (a) is found at the Fermi level in the spin down channel. Here, the energy dispersion is linear and the electron dynamics can be treated as relativistic, where the Fermi velocity of the electrons exhibit the role of speed of light, which is also availed by the ref. [41]. The formation of Dirac cone at the Fermi level exhibits the peculiar transport characteristic of electrons

in the system [40]. These bands correspond to Dirac bands and they exhibit mass-less fermions [69]. A perfect linear gapped type Dirac cone (b) was found below the Fermi level near the K point in the spin down channel. The self doping properties are also preserved in $2 \times 2 \times 1$ forming the Dirac cone below the Fermi level. Similarly, a linear gapped Dirac cone (c) and a distorted gapped Dirac cone (d) are also found at region K-Γ below and above the Fermi level in the spin down channel, respectively. The dispersed bands from M to K points are reunited at the K point above the Fermi level. Similarly, in regions between Γ-M and K-Γ, there are multiple topological states in region above the Fermi level. These topological phenomena are resulted from quantum oscillations. Figure 3.16Q represents the band structure corresponding to the spin up channel. Two open Dirac cones, one linear (e) and other distorted (f) are found in regions M-K and K-Γ below the Fermi level.

Figure 3.17 represents the band structure of Ti_2N corresponding to the spin down (P) and spin up (Q) channels in $3 \times 3 \times 1$ super-cell. The bands cross the Fermi level from the occupied states to the unoccupied states and vice versa as shown in FIG. 3.17P. Interestingly, a gapped Dirac cone (a) is found at the Fermi level revealing the peculiar transport phenomenon at region between Γ-M in the spin down channel [40]. In the spin up channel, the bands are slightly crossed at the Fermi level from the unoccupied states to the occupied states revealing the half-metallic character preserved in $3 \times 3 \times 1$ super-cell as shown in FIG. 3.17Q. Two distorted Dirac cones (c) and (d) are found above the Fermi level in regions Γ-M and K-Γ. Similarly, one linear gapped (e) and a gapped angular (f) Dirac cones are found below the Fermi level in regions M-K and K-Γ, respectively. While moving from $2 \times 2 \times 1$ to $3 \times 3 \times 1$ super-cells, the gap in the Dirac cones (f) is decreased by 10 meV by flipping the nature of tip of the Dirac cone as shown in FIG. 3.16f and 3.17f, respectively. Similarly, the gap in Dirac cone (e) is also decreased by 30 meV as shown in FIG. 3.16e and 3.17e.

After surface termination, all the functionalized MXenes Ti_2NT_2 (T = -OH, -H, -F) become metallic NM [1] except for oxygen terminated one, which is found to be half-metallic ferromagnet [14]. The electronic properties of Ti_2NF_2 and $Ti_2N(OH)_2$ are

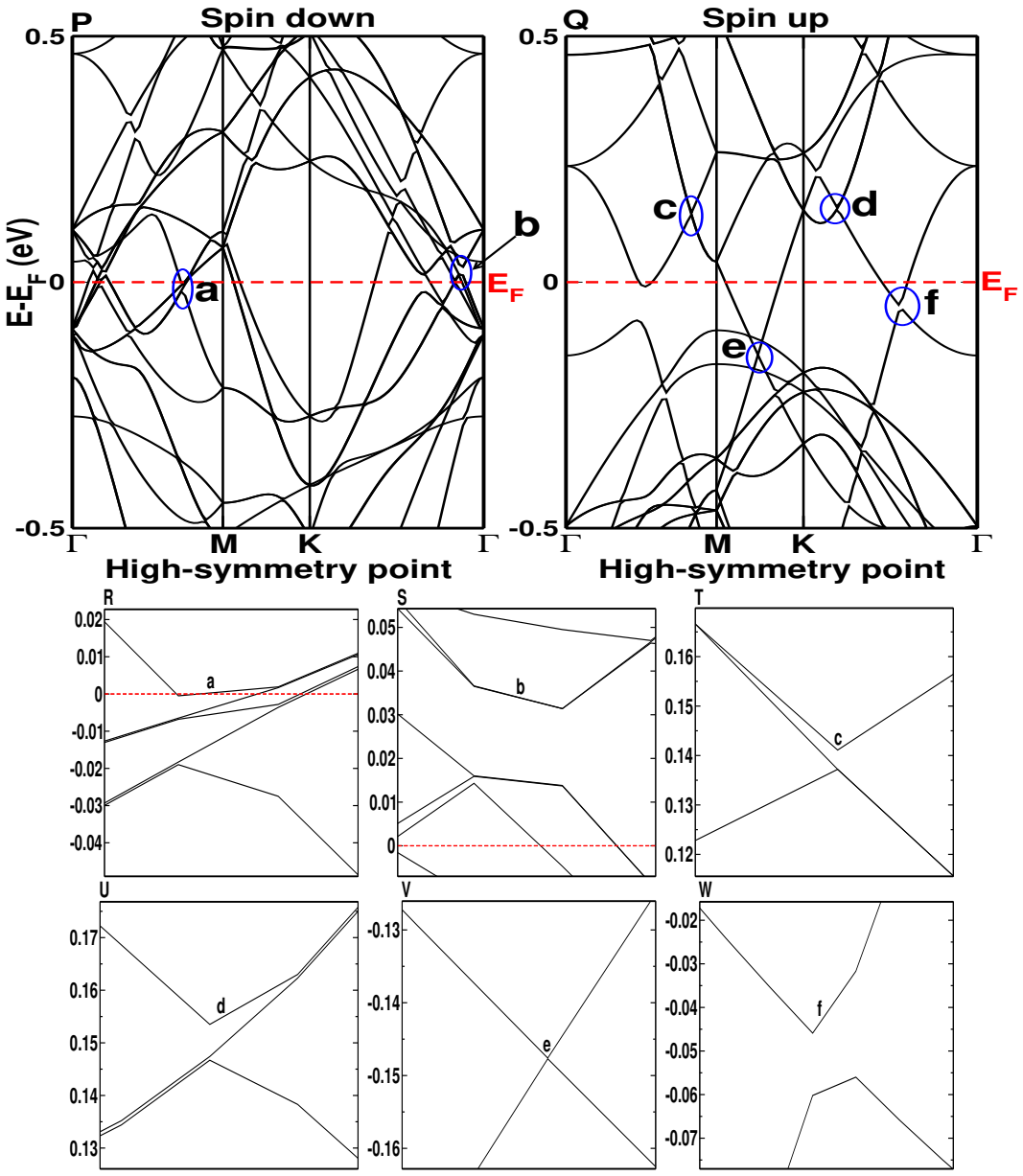

Figure 3.17: (Color online) P and Q represent the spin down and spin up band structure of MXene Ti_2N in $3 \times 3 \times 1$ super-cell respectively. R, S, T, U, V, and W highlight the Dirac topology found in the electronic band structures. The red dash lines represent the position of the Fermi level in the electronic band structure.

similar due to the presence of electrophiles -F and -OH, which accept one electron from Ti. However, the electronic property of Ti_2NO_2 is different due to the presence of -O electrophile, which accepts two electrons from Ti atom [70].

The band structure of hydrogen terminated MXene in $1 \times 1 \times 1$ mono-layer is shown in FIG. 3.12. The band splitting from a Γ point is reconstructed at another Γ point just below the Fermi level. Further, the bands cross the Fermi level from the occupied states to

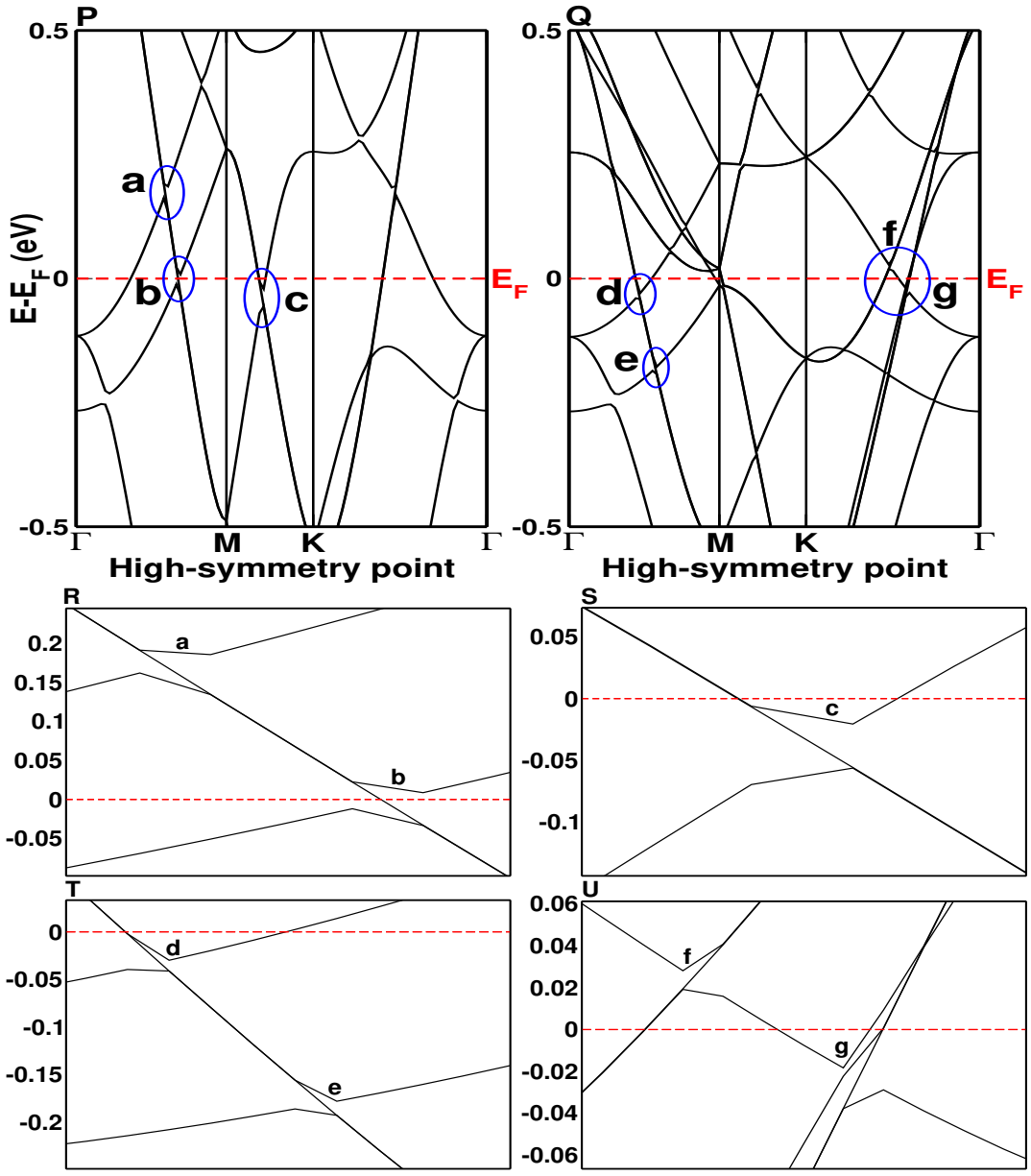

Figure 3.18: (Color online) P and Q represent the band structure of MXene Ti_2NH_2 in $2 \times 2 \times 1$ and $3 \times 3 \times 1$ super-cells respectively. R, S, T, and U represent the Dirac topology associated in the electronic band structures. The red dash lines represent the position of the Fermi level in the electronic band structure.

the unoccupied states, thereby converting the nearly half-metallic Ti_2N to metallic. This metallic behavior is also preserved in $2\times2\times1$ and $3\times3\times1$ super-cells as shown in FIG. 3.18. Various multiple Dirac features have been found under the H termination. The linear gapped Dirac cone (b) is found exactly at the Fermi level exhibits the paramount transport characteristic of electrons in the band structure [40] as shown in FIG. 3.18R. The bands corresponding to that Dirac cones are called Dirac bands and the charge car-

riers (electrons and holes) in that region will behave as massless Dirac fermions similar to that of SiC_3 siligraphene [71]. Similarly, a gapped slightly distorted Dirac cone (c) found just below the Fermi level (FIG. 3.18S) exhibits n-type self-doping character [38] and enhances the conductivity. These features are shifted down in $3 \times 3 \times 1$ super-cell as shown in FIG. 3.18(P and Q). While moving to $3 \times 3 \times 1$ from $2 \times 2 \times 1$ super-cells, the gapped linear Dirac cone (a) found above the Fermi level (conduction band) is shifted down below the Fermi level (valence band) in the form of gapped distorted Dirac cone (d), a self n-type doping character. Surprisingly, two linear distorted Dirac cones (f) and (g), which exhibit self p- and n- types of doping characters [38], have been found exactly above and below the Fermi level as shown in FIG. 3.18U. A gapped distorted Dirac cone (e) is also found in region Γ-M below the Fermi level. The presence of SOC does not changes the electronic properties in the band structure.

The bands cross the Fermi level from the occupied states to the unoccupied states indicating metallic property in F terminated $1 \times 1 \times 1$ mono-layer MXene as shown in FIG. 3.12 similar to that of H terminated one. Astonishingly, a gapped Dirac cone is found at K point on the Fermi level. Figure 3.19 shows the band structure of fluoride terminated MXene in $2 \times 2 \times 1$ and $3 \times 3 \times 1$ super-cells. The linear and angular distorted Dirac cones (a) and (b) have been found below the Fermi level in the region Γ-M and above the Fermi level in the region M-Γ as shown in FIG. 3.19(R and Q). Two distorted Dirac cones (c) and (d) are found above the Fermi level as shown in FIG. 3.19T. A distorted and a linear Dirac cones (e) and (f) above the Fermi level have been found in the region Γ-M in $3 \times 3 \times 1$ super-cell as shown in Fig. 3.19U. The presence of SOC does not change the electronic properties in the band structure as expected.

The oxygen termination in Ti_2N MXene converts the nearly half-metallic to 100% spin polarized half-metallic as shown in FIG. 3.14. The spin up and the down bands are found to be with similar characters as shown in FIG. 3.14P. The black and red colored bands correspond to the spin down and the spin up channels. The spin down channel clearly shows the semi-conducting nature whereas the spin up channel shows the metallic nature exhibiting the half-metallic character. This half-metallic FM nature is

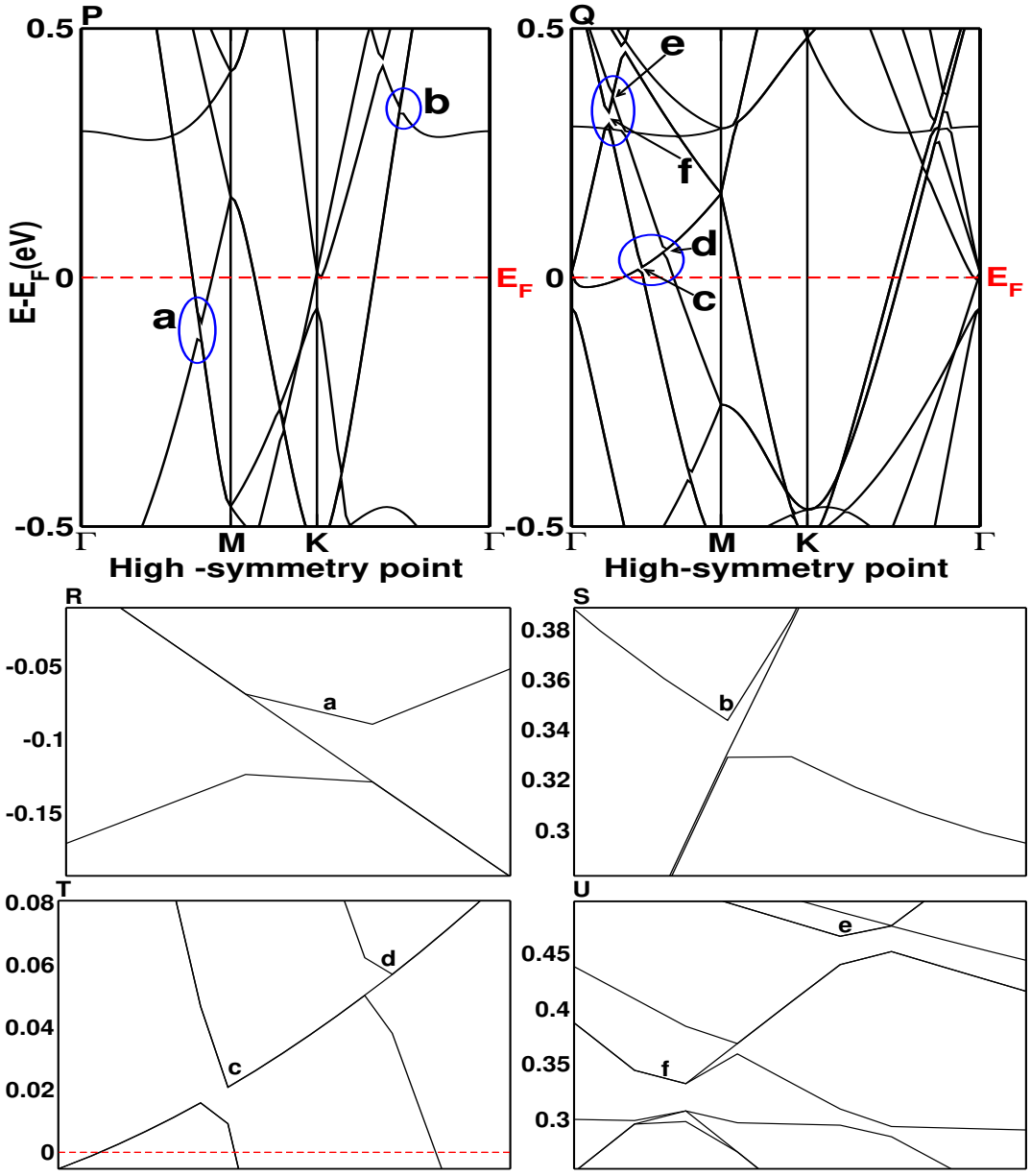

Figure 3.19: (Color online) P and Q represent the band structures of MXene Ti_2NF_2 in $2\times2\times1$ and $3\times3\times1$ super-cells respectively. R, S, T, and U highlight the Dirac topology found in the electronic band structures. The red dash lines represent the position of the Fermi level in the electronic band structure.

due to the exchange splitting energy of 0.42 eV, which is higher than that found in Ti_2N mono-layer. The spin down band splits from the near Γ point above the Fermi level and reconstructs at another Γ point above the Fermi level. Same behavior happens for the spin up band starting from below the Fermi level. The presence of SOC in Ti_2NO_2 mono-layer converts half-metallic to topological half-metallic nature. Interestingly, the distorted gapped Dirac cone (a) and linear gapped Dirac cone (e) are found above the

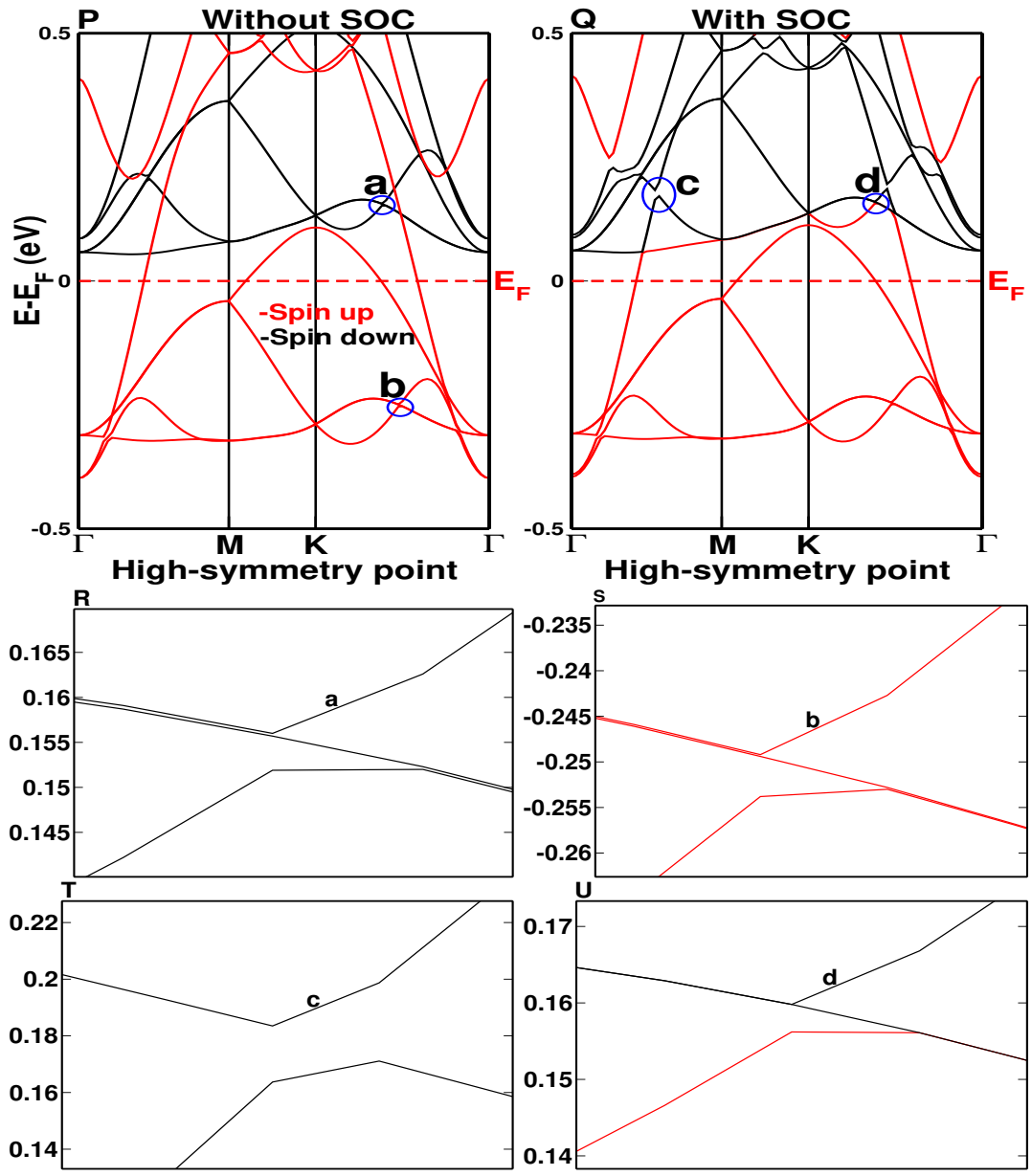

Figure 3.20: (Color online) P and Q represent the band structures corresponding to without SOC and SOC of MXene Ti_2NO_2 in $2 \times 2 \times 1$ super-cell respectively. R, S, T, and U highlight the Dirac topology found in the electronic band structures. The red dash lines represent the position of the Fermi level in the electronic band structure.

Fermi level in region Γ-K and K-Γ, respectively. Similarly, three distorted Dirac cones (b), (c), and (d) are found in the vicinity of K point above the Fermi level. On moving from $1 \times 1 \times 1$ mono-layer to $2 \times 2 \times 1$ and $3 \times 3 \times 1$ super-cells, the multiple Dirac cones have been found as shown in FIG. 3.20 and 3.21. In $2 \times 2 \times 1$ super-cell, two distorted Dirac cones (a) and (b) have been found above and below the Fermi level in the region K-Γ as shown in FIG. 3.20P. The presence of SOC appreciably changes

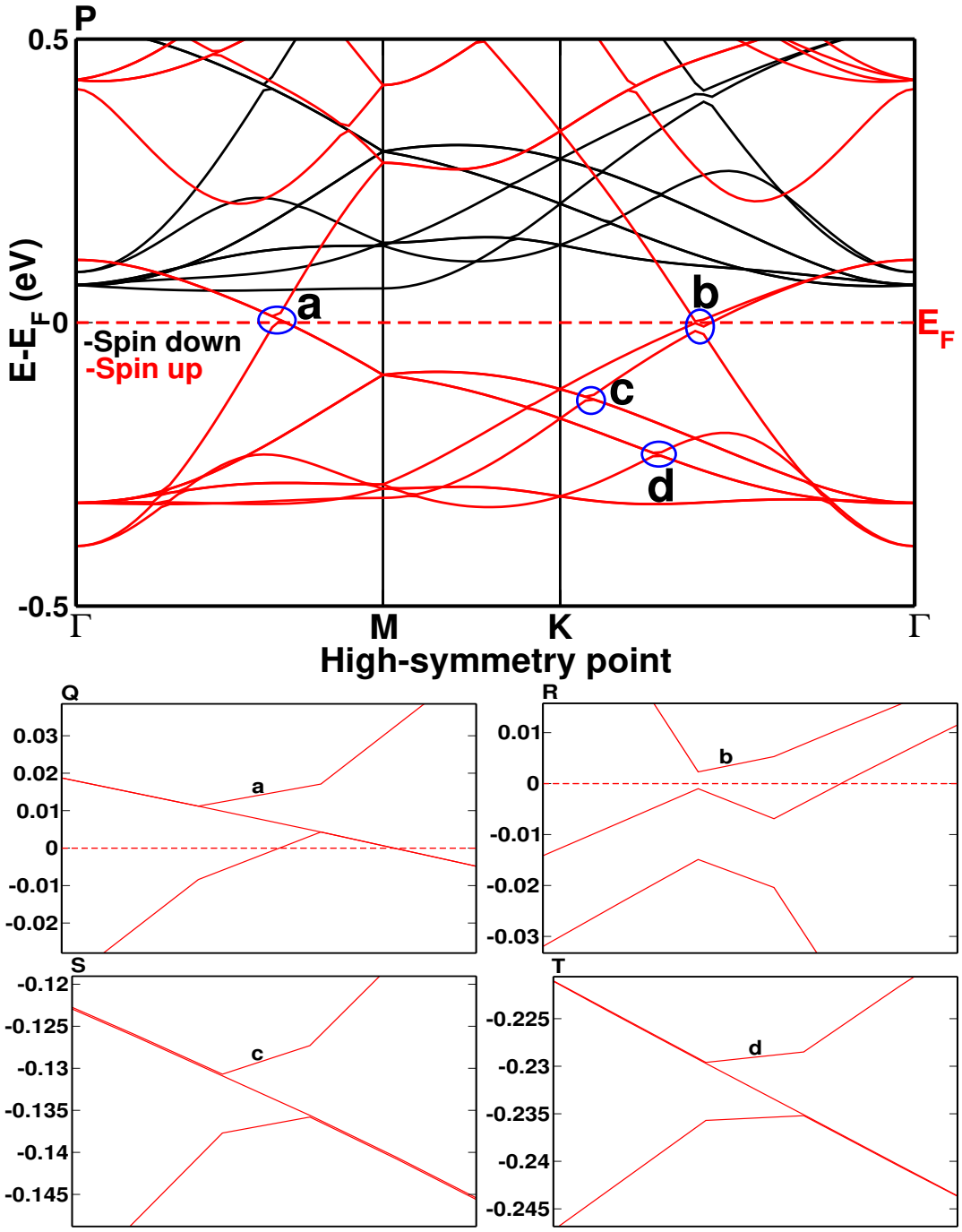

Figure 3.21: (Color online) P represents the band structure of MXene Ti_2NO_2 in $3\times3\times1$ super-cell. Q, R, S, and T highlight the Dirac topology found in the electronic band structure. The red dash lines represent the position of the Fermi level in the electronic band structure.

the electronic properties especially at the region above the Fermi level of Ti_2NO_2 in $2\times2\times1$ super-cell as shown in FIG. 3.20Q. Linear gapped Dirac cone (c) and a gapped angular Dirac cone (d) are found in regions Γ-M and K-Γ above the Fermi level. While moving to $3\times3\times1$, two distorted gapped Dirac cones (a) and (b) are found at the

Fermi level as shown in FIG. 3.21 (Q and R). Similarly, two linear Dirac cones (c) and (d) are also found in region K-Γ below the Fermi level as shown in FIG. 3.21 (S and T), respectively. These behaviors provide a control over electron-hole doping and transport phenomenon exhibited by these materials.

Similarly, -OH termination in $1 \times 1 \times 1$ mono-layer is also found to be metallic character. Interestingly, a gapped Dirac cone is found at K point above the Fermi level. The charge carrier corresponding to that Dirac cone behaves like hole-packets at the conduction band [42]. The metallic properties are also preserved in $2 \times 2 \times 1$ and $3 \times 3 \times 1$ super-cells with various topological characters as shown in FIG. 3.22. In the region Γ-M of $2 \times 2 \times 1$ super-cell, two linear gapped Dirac cones (a) and (b), and one linear gapped Dirac cone (c) are found above and below the Fermi level, respectively. While moving to $3 \times 3 \times 1$ super-cell, two linear Dirac cones (d) and (e) are found just above the Fermi level in region Γ-M. Similarly, three linear gapped Dirac cones (f), (g), and (h) are found above the Fermi level and other three linear gapped Dirac cones (i), (j), and (k) are found in the region K-Γ below the Fermi level as shown in FIG. 3.22Q. Alluringly, a gapped distorted Dirac cone (l) and a gapped linear Dirac cone (m) are also found in the region K-Γ near the Fermi level exhibiting the quantum oscillation. Therefore, the -OH termination in $3 \times 3 \times 1$ super-cell is topologically more informative as compared to other surface terminated MXenes. The presence of SOC in -OH termination also does not changes the electronic properties.

To get better deliberation on the electronic structure properties of MXene, PDOS are shown in FIG. 3.12. After eliminating Al from MAX phase, bands become narrow and form open gap making large indirect gap of 2.40 eV in the spin up and 2.59 eV in the spin down (within the occupied part) are found between the sub-bands A and B in Ti_2N as shown in FIG. 3.15. The sub-band A is formed due to strong contribution from Ti-3*d* states and weak contribution from N-2*p* states. Similarly, the sub-band B is formed due to the combination of N-2*p* states and Ti-3*d* states with major contribution from N-2*p* states. This may indicate that, the change occurring way below the Fermi level influences the electronic states at the Fermi level as discovered earlier in ref. [72]. The

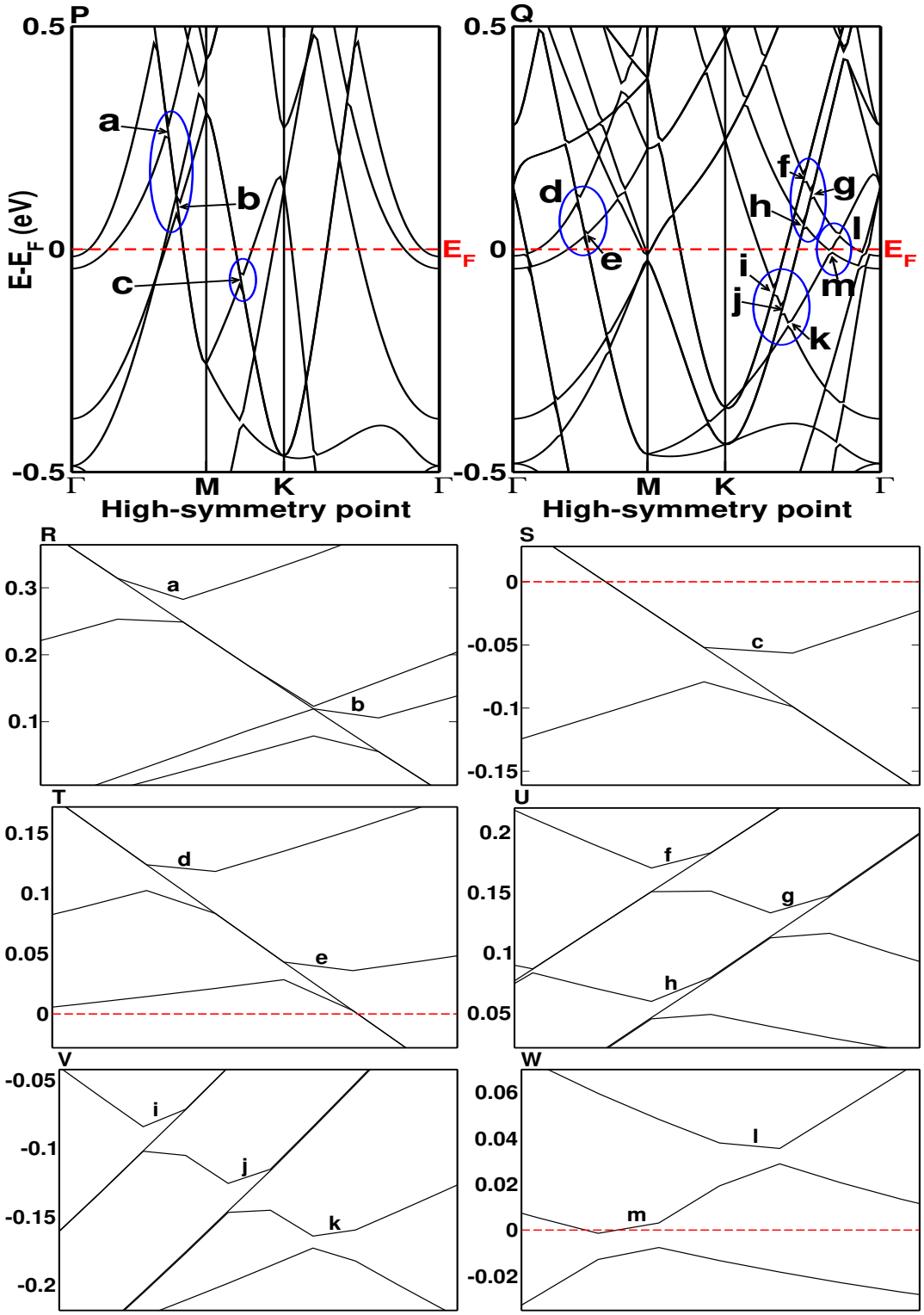

Figure 3.22: (Color online) P and Q represent the band structure of MXene $Ti_2N(OH)_2$ in $2 \times 2 \times 1$ and $3 \times 3 \times 1$ super-cells, respectively. R, S, T, U, V, and W highlight the Dirac topology found in the electronic band structure. The red dash lines represent the position of the Fermi level in the electronic band structure.

nature of PDOS are preserved in larger super-cells as shown in FIG. 3.23.

The termination on mono-layer MXene plays a vital role especially far below the Fermi

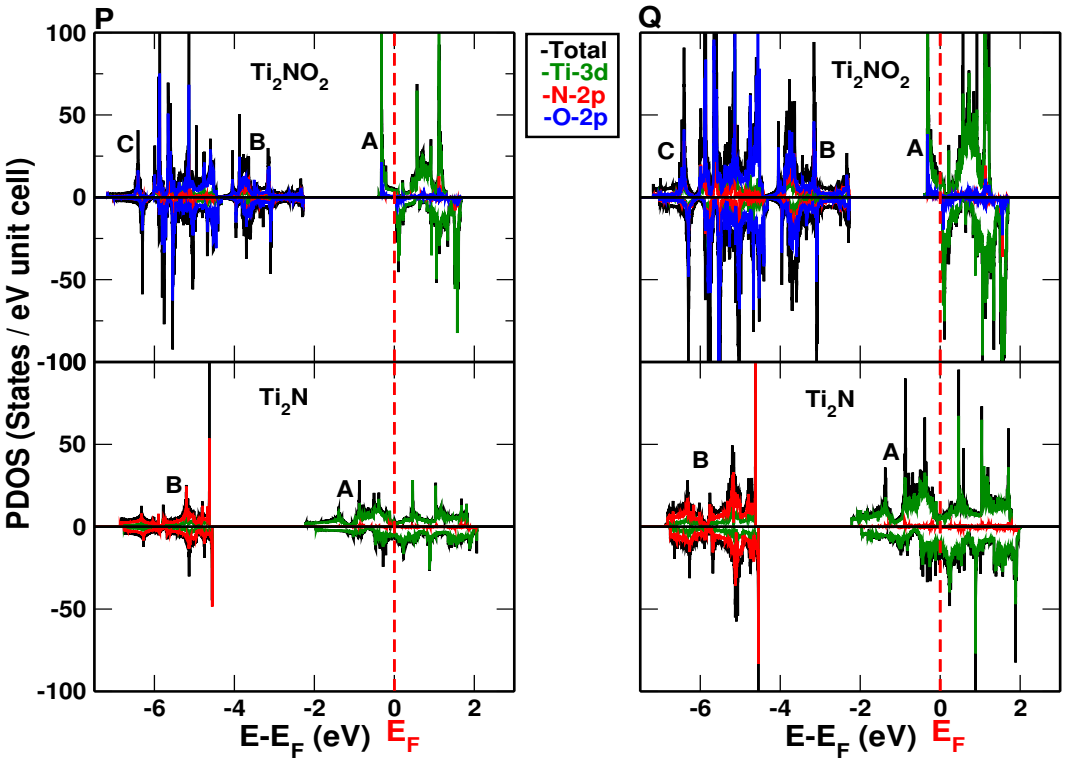

Figure 3.23: (Color online) P and Q represent the PDOS of MXenes Ti_2N and Ti_2NO_2 in $2 \times 2 \times 1$ and $3 \times 3 \times 1$ super-cells respectively. The red dash lines represent the position of the Fermi level in PDOS.

level in the valence band. The surface termination in the bare MXene mono-layer splits the sub-band B into separate sub-bands B and C. In fluoride termination, the sub-band A is dominated by Ti-3*d* states and the sub-bands B and C are the mixed of Ti-3*d*, N-2*p*, and F-2*p* states. The sub-band C is significantly dominated by F-2*p* states. The large indirect energy gap of 2.71 eV and comparatively small direct energy gap of 0.74 eV are found between the sub-bands A and B, and the sub-bands B and C, respectively. The nature of PDOS are preserved in larger super-cells as shown in FIG. 3.24.

Hydroxyl termination follows the similar trend in which the sub-band A is dominated by Ti-3*d* states. The sub-band B is the mixed states of Ti-3*d*, N-2*p*, and O-2*p* states but the sub-band C is the mixed states of O-2*p*, Ti-3*d*, and H-1*s*, and N-2*p* states. The indirect energy gap of 1.65 eV and the direct energy gap of 1.84 eV are found between the sub-bands A and B, and B and C ,respectively. The nature of PDOS are also preserved in larger super-cells as shown in FIG. 3.24.

Similarly, the sub-band A in H and O terminated MXenes are also dominated by Ti-3*d*

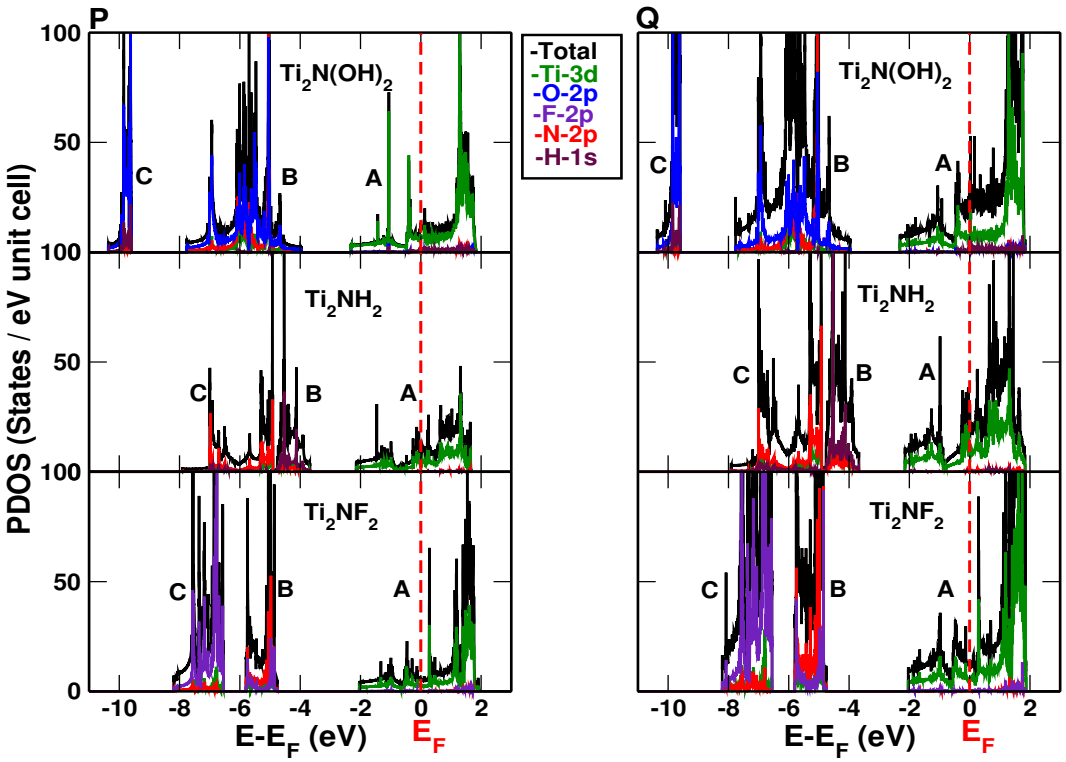

Figure 3.24: (Color online) P and Q represent the PDOS of MXenes Ti_2NF_2, Ti_2NH_2, and $Ti_2N(OH)_2$ in $2 \times 2 \times 1$ and $3 \times 3 \times 1$ super-cells, respectively. The red dash lines represent the position of Fermi level in PDOS.

states. The hydrogen atom contributes only in the sub-band B. In hydrogen termination, only one indirect energy gap of 1.53 eV is found between sub-bands A and B, and continuous bands are found between the sub-bands B and C indicating that the hydrogen atom does not play significant role in the bare MXene Ti_2N as compared to other. Likewise, in oxygen termination, the small direct energy gap of 0.13 eV in the spin up and 0.09 eV in the spin down are found between the sub-bands B and C exhibiting the strong hybridization between Ti-3*d*, N-2*p*, and O-2*p* states. But the large indirect energy gap of 1.88 eV in the spin up and 2.22 eV in the spin down are found between the sub-bands A and B. The sub-band C is mainly dominated by N-2*p* states. The nature of PDOS are also preserved in larger super-cells as shown in FIG. 3.23 and 3.24 for oxygen and hydrogen termination.

From the electronic band structure, the Fermi level is shifted down in bare MXene obtained by etching Al from the MAX phase and is again shifted down under the surface terminations. The sub-band C is found below the sub-band B, due to electronic

reconstruction between Ti and functional group. The functional group significantly contributes in sub-band C except for sub-band B in hydrogen termination.

3.2.3 Origin of Half-metallic Gap in Ti_2NO_2

The magnetism and half-metallicity strongly depends upon the coordination environment of Ti and the number of 3*d* electrons associated within it. It plays a vital role in the electronic and magnetic properties.

Similar to TM dichalcogenides, the non-bonding 3*d* bands in MXenes are positioned between the bonding and anti-bonding of Ti-N and Ti-O states [73]. Presuming all the constituent elements (N and O) are in their normal oxidation states O^{2-} and N^{3-}, the Ti-N and Ti-O bonding states are completely filled, while their anti-bonding states are empty. So, only the presence of 3*d* electrons in non-bonding states are able to contribute to the magnetism of Ti_2NO_2. In Ti_2NO_2, the Ti atom subjected to octahedral crystal field (with symmetry D_{3d}) from neighboring N and O atoms. As shown in FIG. 3.25, E_g corresponds to (x^2-y^2, xy) and (xz, yz) degenerate states, whereas $A_{1g}(z^2)$ form a separate state refs. [73, 74]. The magnetism appearing in this class of materials are due to mixed localized and delocalized characters of Ti-3*d* instead of electron counting applied in refs. [14, 73].

Figure 3.25P details the projected spin polarized 3*d* DOS of Ti in $1 \times 1 \times 1$ mono-layer Ti_2NO_2. The t_{2g} and e_g are not separated in DOS. The d_{xy} from t_{2g} and $d_{x^2-y^2}$ from e_g states make degenerate states, whereas the d_{xz} and d_{yz} states of t_{2g} also make degenerate state. The three multiplets are formed by d_{z^2}, d_{xy} and $d_{x^2-y^2}$, and d_{yz} and d_{xz}. Individually, the non-degenerate d_{z^2} state dominates the other states in both spin channels. The d_{z^2} state crosses the degenerated states $d_{x^2-y^2}$ and d_{xy} exactly at the Fermi level. The concept of t_{2g} and e_g states breaks down due to the local symmetry, which is responsible for the half-metallic character in Ti_2NO_2.

The top and bottom layers of Ti provide two electrons to O atoms in respective sides and they jointly (both bottom and top of Ti layers) provide three electrons to the neighboring N atoms. Due to lattice symmetry, there is equal possibility for +4 and +3 oxidation

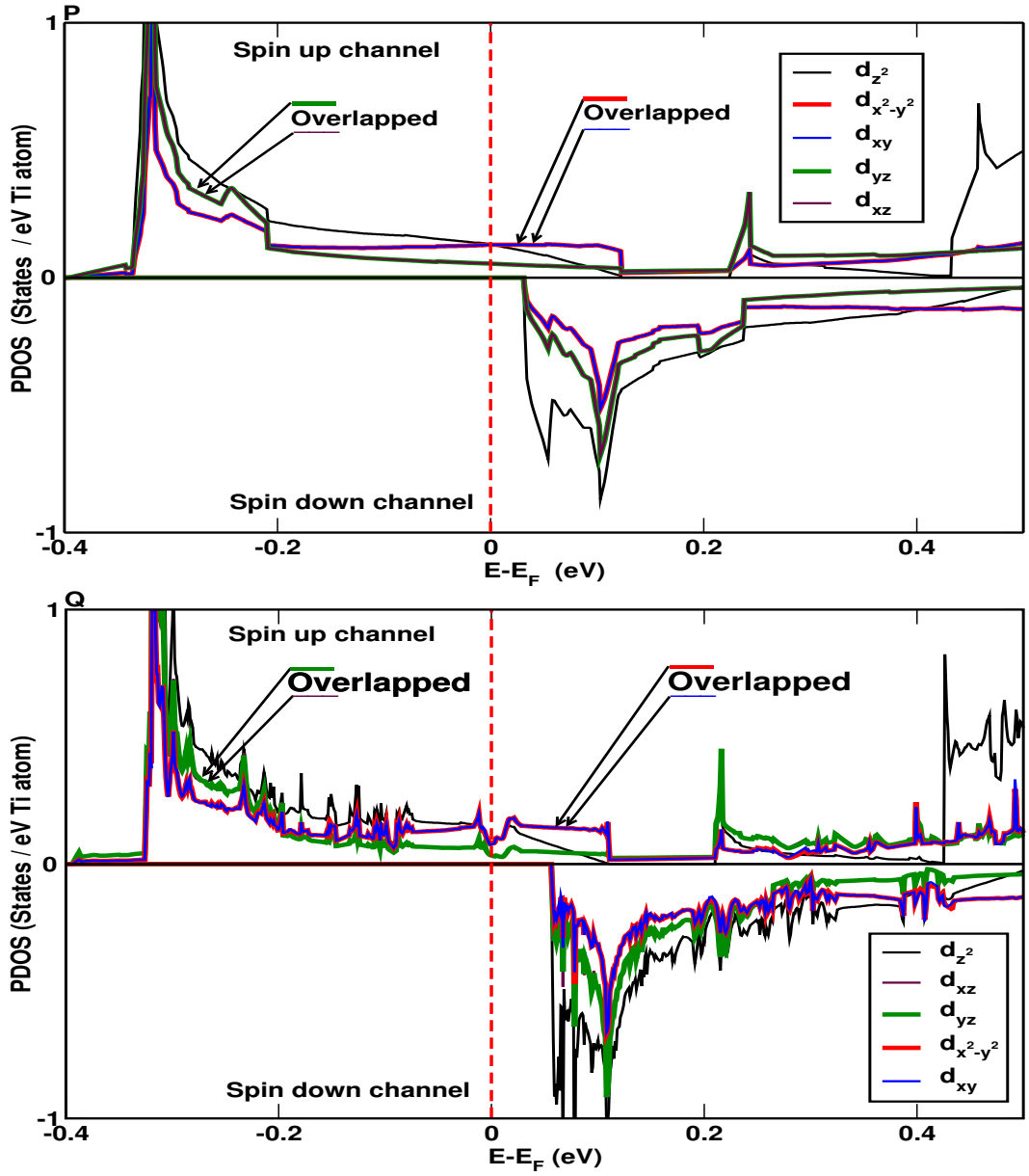

Figure 3.25: (Color online) P and Q represent the projected spin polarized 3*d* DOS of Ti in Ti_2NO_2 within $1 \times 1 \times 1$ mono-layer and $3 \times 3 \times 1$ super-cells, respectively. The Ti atom follows the octahedral symmetry (D_{3d}) crystal field from neighboring N and O, which split the 3*d* orbital into t_{2g} (d_{xz}, d_{yz}, and d_{xy}) and e_g ($d_{x^2-y^2}$ and d_{z^2}) states. The red dash lines represent the position of the Fermi level.

states of Ti in the top and bottom layers. The remaining one 3*d* electron either fills the non-bonding states or helps to delocalize the system to have band magnetic feature and telltale the magnetic moment of 0.27 μ_B per Ti atom. This magnetic moment splits the above mentioned states into fully occupied bands for majority spin channel and open bands for minority spin states providing the semiconducting nature with large gap of 2.28 eV in the minority spin channel, which is also availed by ref. [14]. The material

with large half-metallic gap is most promising magnetic material for the next generation 2D spintronics [75, 76].

On instigating to $2 \times 2 \times 1$ super-cell, the degenerated and non-degenerated states of 3*d* orbitals are similar as $1 \times 1 \times 1$ mono-layer with slight changes in the position of the Fermi level. Intriguingly, half-metallic semi-metal is revealed with topological feature making pseudo gap within the spin up channel and semi-conductor in the spin down channel for individual Ti atom in $3 \times 3 \times 1$ super-cell, which is a novel result found in the MXene. In the pseudo gap, the non-degenerated d_{z^2} state of e_g state is degenerated with $d_{x^2-y^2}$ from e_g and d_{xy} from the t_{2g} states as shown in FIG. 3.25Q. This pseudo gap is responsible for the quantum oscillation. Integrating over all Ti, the half-metallic semi-metal becomes more half-metallic as shown in FIG.3.23Q.

3.2.4 Effect of Biaxial Strain in Electronic Band Structure of MXene

Here, we have studied the compressive strain a(1-e) and the tensile strain a(1+e) (where, e represents compression and elongation up to 5% with increment of 1%) keeping the fixed value of the vertical distance at 17.04 Å. Figure 3.26 (P and Q) represents the band structure under compression and tensile strains. Here, a, b, c, d, e, and f correspond to equilibrium/zero strain, 1%, 2%, 3%, 4%, and 5% compression and tensile strains in $Ti_2N(OH)_2$, respectively. Under the compression (up to 5%), the Fermi level is shifted up continuously by pushing the electrons from the occupied states to the unoccupied states as shown in FIG. 3.26P. The distorted Dirac cone is found at K point above the Fermi level, which remains distorted under 1% compression. Additionally, on increasing the compressive strain from 1%, the distorted gapped Dirac features change to linear gapped Dirac (in 2%, 3%, and 4%) and finally returns to Distorted gapped Dirac cone under 5% compression. Again, the complex gapped Dirac features are also found in the region between K-Γ below the Fermi level under compression from 2% to 5%.

Unlike the compression, the scenario of shifting the Fermi level is reversed during the tensile strain. The Fermi level is continuously shifted down under tensile strain indi-

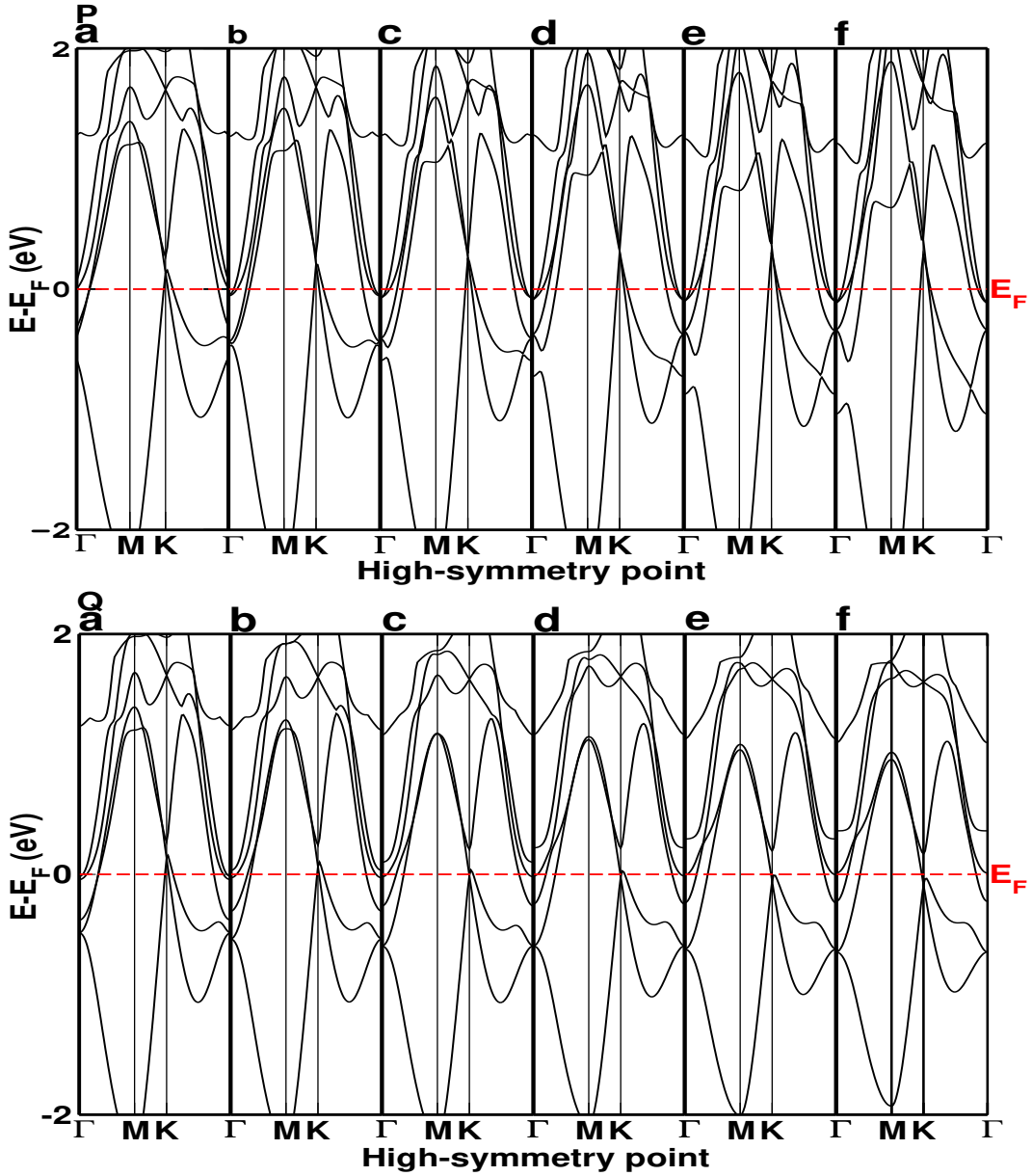

Figure 3.26: (Color online) P and Q represent the band structure under compression and tensile strains up to 5% in $Ti_2N(OH)_2$ MXene. The red dash lines represent the position of the Fermi level in the electronic band structure.

cating the electrons are pushing from the unoccupied states to the occupied states as shown in FIG. 3.28Q. While increasing the strength of tensile strain, the gapped Dirac cone get enhanced as shown in FIG. 3.26Q. We have also studied the effect of applied compression and tensile strains in the bare MXene Ti_2N and other surface terminated MXenes such as: Ti_2NF_2, Ti_2NO_2, and Ti_2NH_2. In Ti_2N , Ti_2NF_2, and $Ti_2N(OH)_2$ MXenes show the same physics for shifting the Fermi level but reversed in the case of Ti_2NH_2 as shown in FIG. 3.28(P and Q). Under the compression, two Dirac cones have

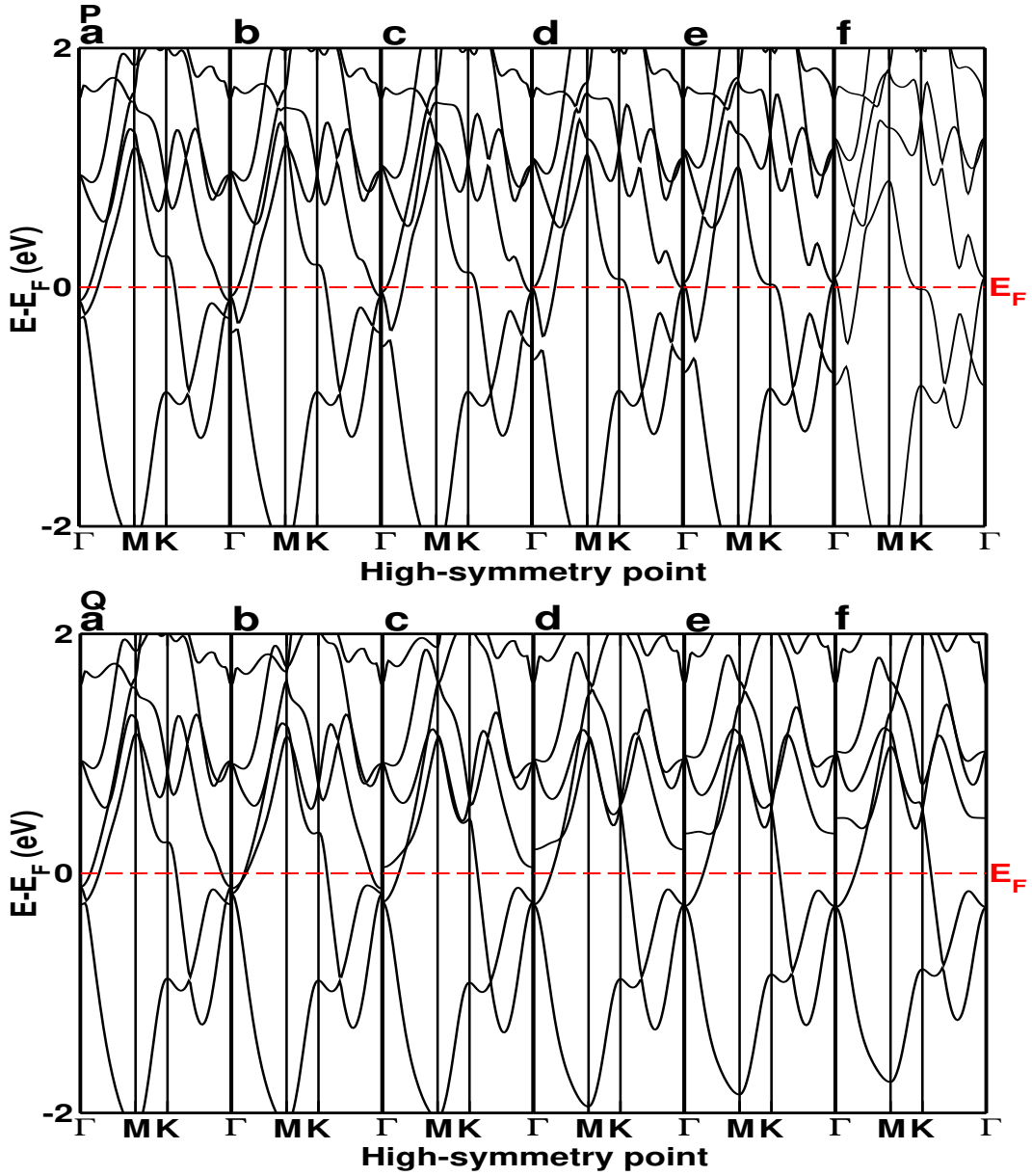

Figure 3.27: (Color online) P and Q represents the band structure under compression and tensile strains up to 5% in Ti_2NH_2 MXene. The red dash lines represent the position of the Fermi level in the electronic band structures.

been found below the Fermi level in the region K-Γ whereas only one Dirac cone has been found under the tensile strain in Ti_2NH_2.

The half-metallic nature in oxygen termination shows peculiar electronic and magnetic properties. The half-metallicity is extremely sensitive to compression. It breaks down under 1% compressive strain as shown in FIG. 3.29P. Under compression, the spin down channel is shifted from the unoccupied states to the occupied states whereas the spin up channel is shifted towards the unoccupied states from the occupied states and finally

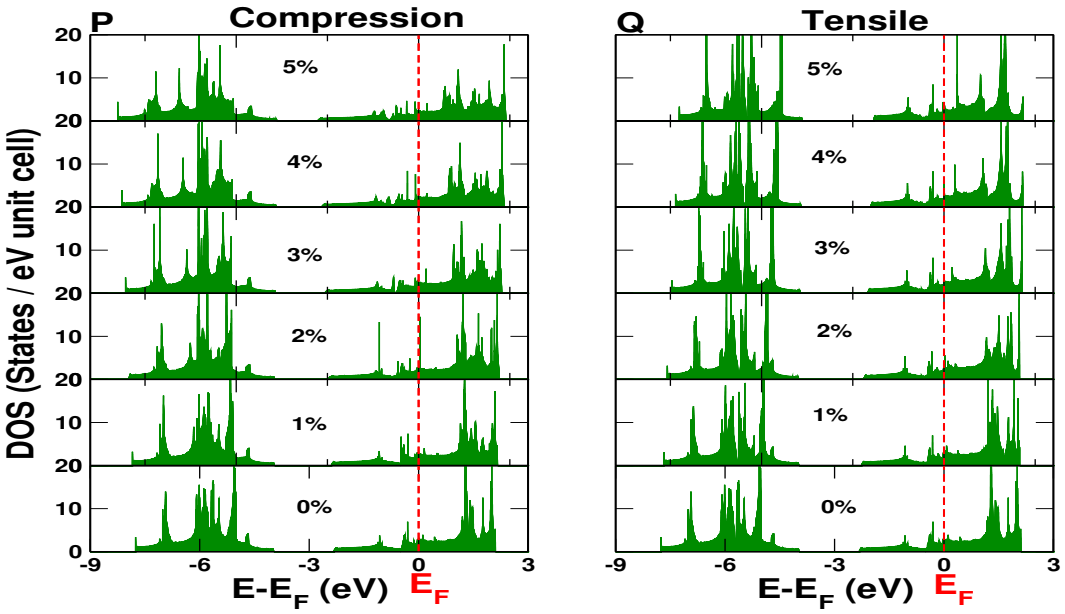

Figure 3.28: (Color online) P and Q represent total DOS under compression and tensile strains up to 5% in $Ti_2N(OH)_2$ MXene. The red dash lines represent the position of the Fermi level in DOS.

both bands are overlapped under 5% compression by converting the system from FM to NM states as shown in FIG. 3.29P. This situation is completely reversed under tensile strain, while increasing the tensile strain, the spin down channel is continuously shifted towards the unoccupied states whereas the spin up channel is continuously shifted towards the occupied states preserving half-metallic character as shown in FIG. 3.29Q. In the spin up Channel, the bands degenerated from Γ point cross the Fermi level in strain free states and reconstruct at other Γ point. The degenerated lower band in up channel just touches the Fermi level at K point under 3% tensile strain. Further, increasing the tensile strain, it completely shift towards the occupied states. The robustness and mutable nature of half-metallic ferromagnetism under applied strain is also clearly shown in FIG. 3.30. The states represented by sub-bands A (spanning from slightly below and above the Fermi level) are significantly dominated by Ti-3*d* states. The sub-bands B and C are the mixed states of Ti-3*d*, O-2*p*, and N-2*p* with the major contribution from the O-2*p* states as shown in FIG. 3.30.

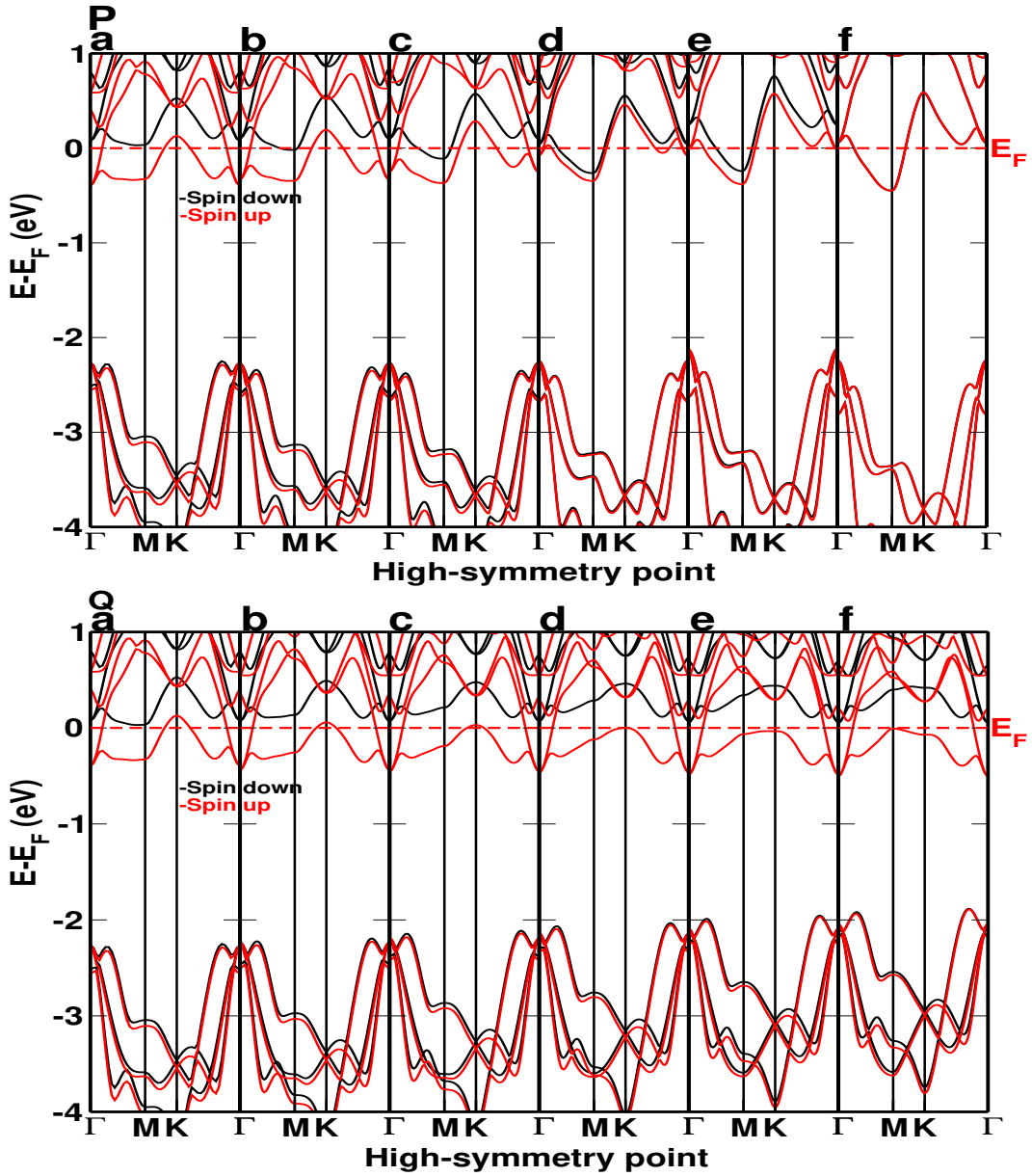

Figure 3.29: (Color online) P and Q represent the band structure under compression and tensile strains up to 5% in Ti_2NO_2 MXene. The red and black colored bands represent the spin up channel and down channel respectively. The red dash lines represent the position of the Fermi level in the electronic band structures.

3.2.5 Vacancy Defect in Ti_2NO_2 MXene

Before studying the electronic and magnetic properties of defected systems, the structural stability corresponding to different super-cells has been studied. The formation and cohesive energies of mono-layer Ti_2N reveal the structural stability starting from $2 \times 2 \times 1$ super-cell as shown in FIG. 3.31(P and Q), respectively. So, the structural defects can be studied within the framework of $2 \times 2 \times 1$ super-cell. Herein, we have

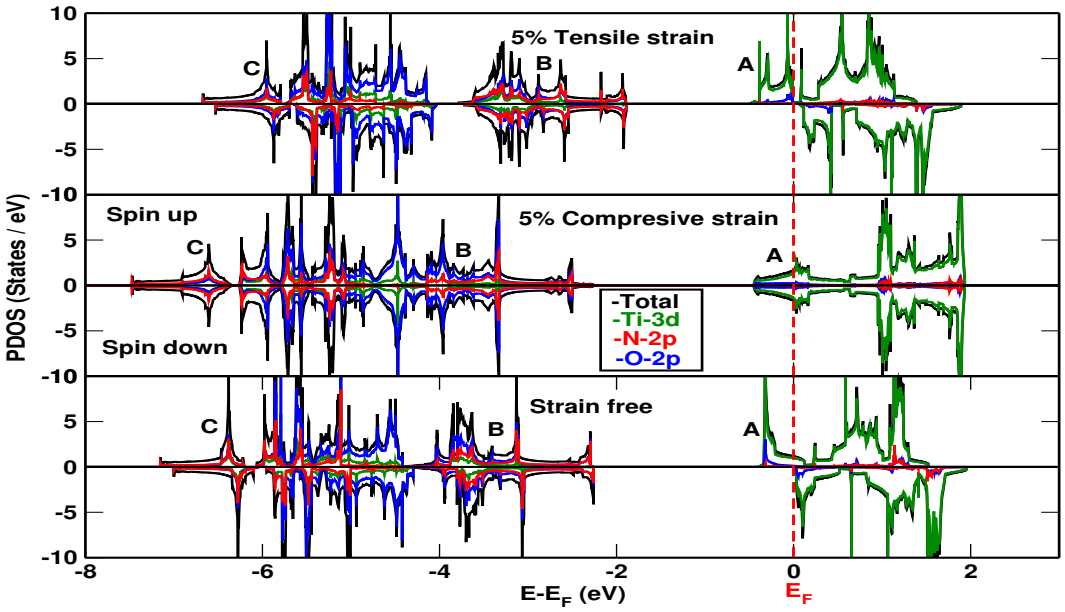

Figure 3.30: (Color online) PDOS under strain free and 5% compressive and tensile strains in Ti_2NO_2 MXene. A, B, and C represent the sub-bands below the Fermi level. The red dash lines represent the position of the Fermi level in PDOS.

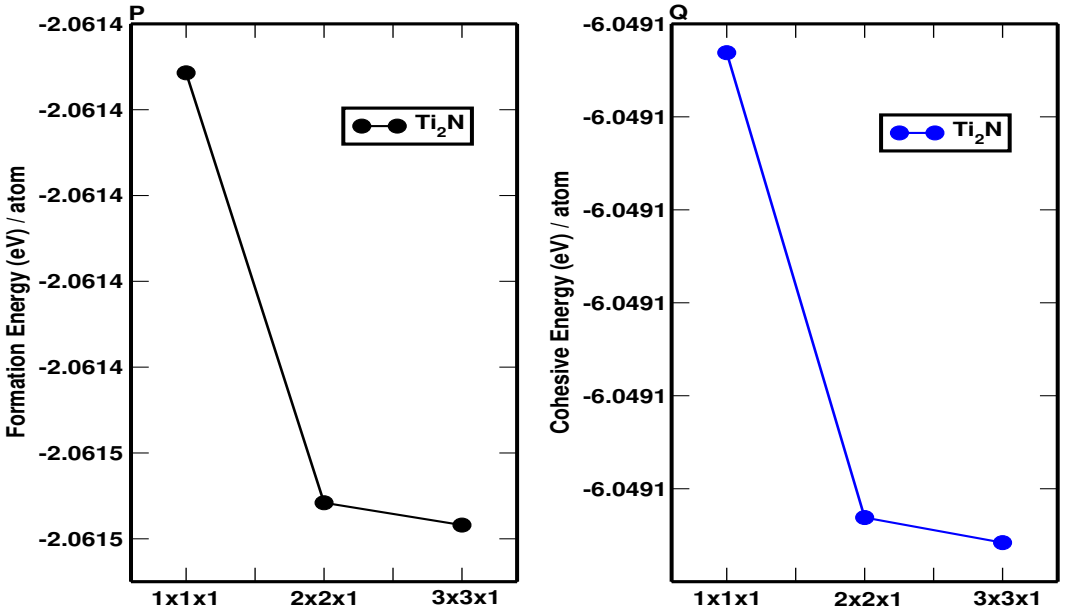

Figure 3.31: P and Q represent the formation and cohesive energies per atom vs number of super-cells respectively.

studied the single vacancy defect and doping in relatively most stable configuration of Ti_2NO_2.

The vacancy concentration defects with N (25%), O (12.5%), and Ti (12.5% and 5.5%) have been studied. The magnetic and NM calculations show NM as the ground state. Therefore, NM configuration was considered to investigate the properties of defected

systems using $2 \times 2 \times 1$ and $3 \times 3 \times 1$ super-cells. The relaxed structures corresponding to N, O, and Ti in MXene Ti_2NO_2 are shown in FIG. 3.32.

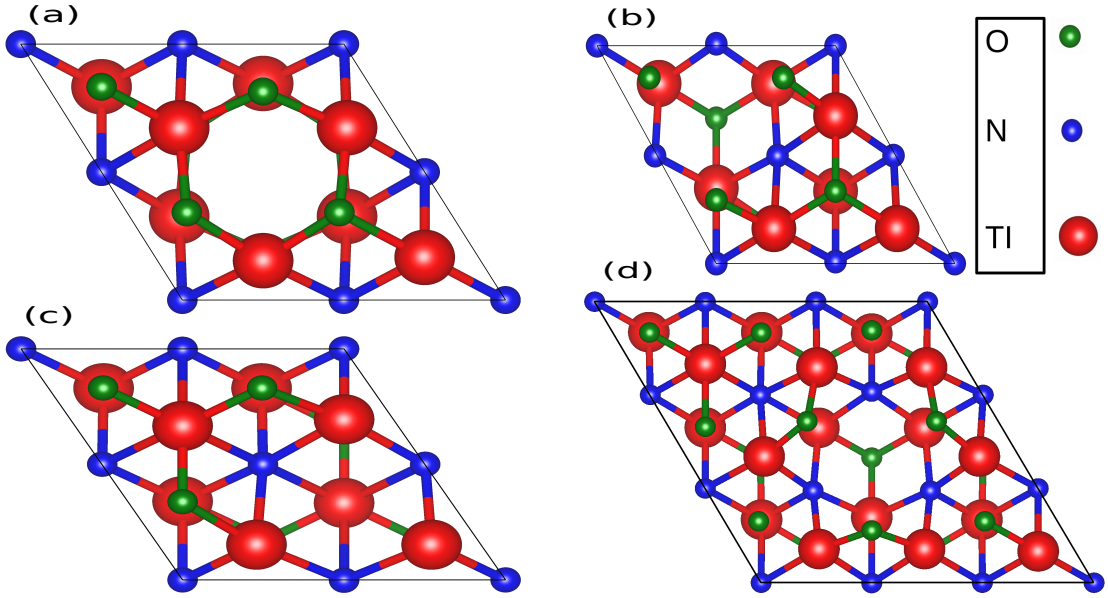

Figure 3.32: (Color online) (a), (b), and (c) are top views of single N, Ti, and O vacancy defects within MXene Ti_2NO_2 in $2 \times 2 \times 1$,respectively and (d) is single vacancy defect of Ti in $3 \times 3 \times 1$ super-cell.

In defect free MXene Ti_2NO_2, the bond length between Ti and N follows symmetrical nature in the entire super-cell. Under the defect formation, the global symmetry is destroyed preserving the local symmetry structures. The formation energy of single vacancy defect is calculated by using formula,

$$E_{SV} = E_{pure} - (E_{defect} + \frac{E_{bulk}}{M}) \tag{3.3}$$

Where E_{pure} and E_{defect} are the total energy of defect free and defected systems, respectively. Similarly, E_{bulk} is the bulk energy of atom forming defect in system and M is total number of atoms in bulk [30]. The calculated value of single vacancy defect formation energy is shown in FIG. 3.33.

The formation energies of single vacancy defects follow the sequence V_{Ti}-Ti_2NO_2 > V_O-Ti_2NO_2 > V_N-Ti_2NO_2. The Ti defect formation is more energy consuming as compared to other because it requires six bonds to break (three Ti-N and three Ti-O). In Ti($3d$)-O($2p$) overlap, the Ti is in +4 oxidation states. The +4 oxidation states in Ti_2NO_2

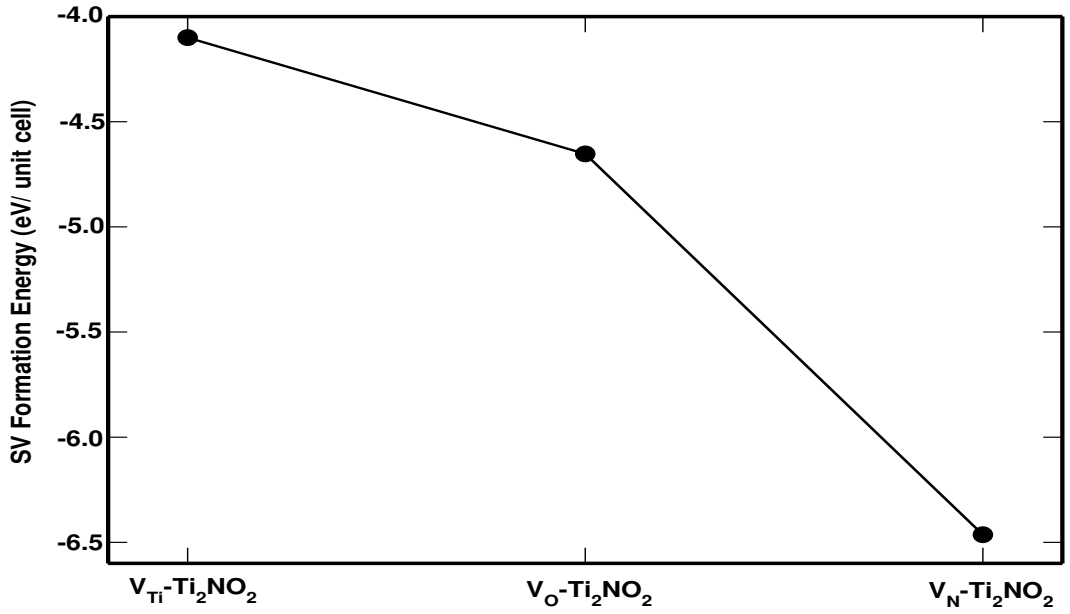

Figure 3.33: The single vacancy formation energies of N, O, and Ti in relatively most stable configuration Ti_2NO_2.

lead to strong Ti-O bond [30]. Due to this reason, Ti-O bond is relatively stronger than Ti-N bond. Similarly, in O defect, which requires only three breaking Ti-O bonds, that way it is relatively less energy consuming than Ti defect but in N defect which requires six Ti-N bonds breaking. This Ti-N bonds are relatively weak as compared to Ti-O bands, so N defect is relatively less energy consuming as compared to Ti and O defect in Ti_2NO_2 MXene sheet. We have also used larger $3 \times 3 \times 1$ super-cell to get more insight in the Ti defected system.

While moving from $2 \times 2 \times 1$ to $3 \times 3 \times 1$ super-cells, the formation energy changes to 0.96 eV designating more stable $2 \times 2 \times 1$ structure as compare to $3 \times 3 \times 1$ super-cell in Ti the defected system. The larger (negative) value of defect formation energy in $2 \times 2 \times 1$ designates the formation of a single vacancy defect.

With the appropriate ground state energy, the electronic band structure and DOS were studied. Interestingly, the single vacancy defect of Ti and O atoms in Ti_2NO_2 abruptly changes the electronic properties from half-metallic to semi-conducting with large direct band gap of 1.73 eV in 12.5% for Ti and topological semi-metal in O defect, which are consistent with previously reported theoretical results [30]. The semi-conducting nature found in Ti defect changes to weak semi-conductor under vacancy concentra-

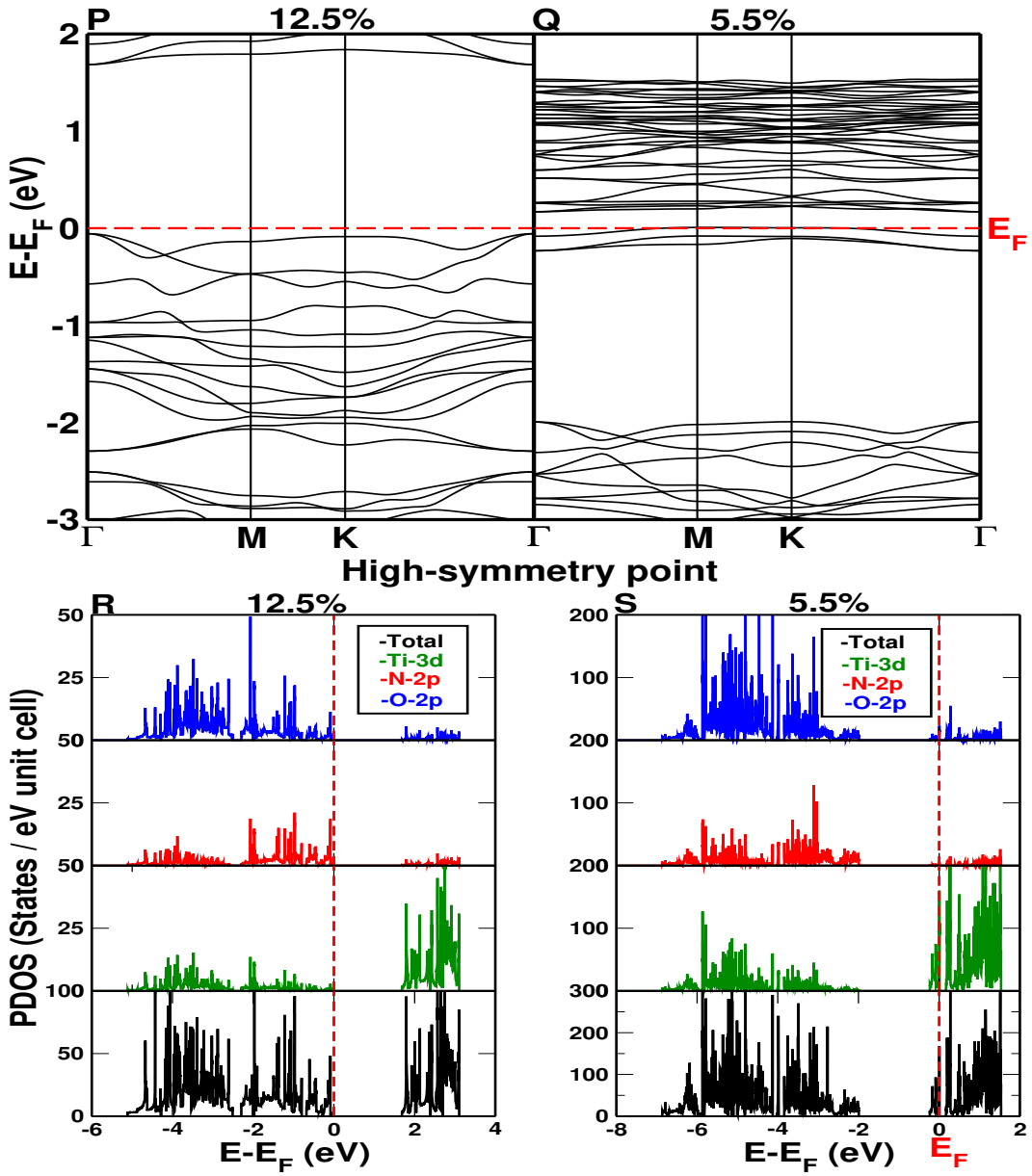

Figure 3.34: (Color online) P and Q are the band structure, and R and S are PDOS of single vacancy of Ti in $2 \times 2 \times 1$ and $3 \times 3 \times 1$ super-cells of Ti_2NO_2 with vacancy concentration 12.5% and 5.5%, respectively. The red dash lines represent the position of the Fermi level in the electronic band structures and PDOS.

tion 5.5%. So, the concentration of vacancy defect eloquently changes the electronics properties of MXene. On decreasing the concentration of vacancy defect, the Fermi level is shifted towards conduction side exhibiting perfect semi-conductor to weak semi-conductor for Ti defect. The NM solution of band structure for O defect with vacancy concentration 12.5% is shown in FIG. 3.35. The topological semi-metal is found by forming two Dirac cones (a) just above the Fermi level and (b) at the Fermi level. The formation of Dirac cone at Fermi level enhances the transport properties of electrons

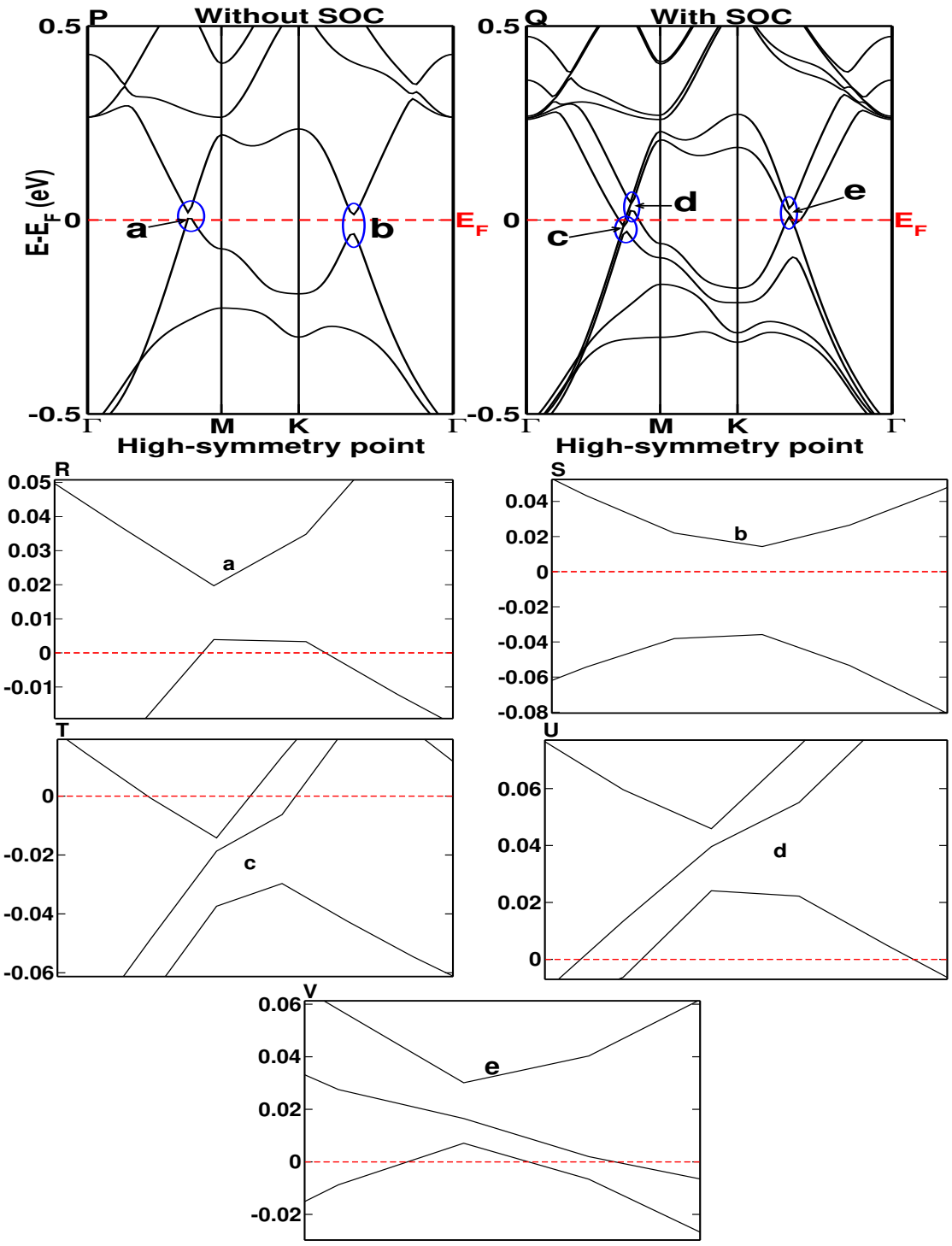

Figure 3.35: (Color online) P and Q represent the band structure correspond to without SOC and SOC with 12.5% vacancy concentration of O within the frame $2 \times 2 \times 1$ super-cell in Ti_2NO_2, respectively. R, S, T, U, and V highlight the Dirac topology found in the electronic band structures. A slightly distorted Dirac cone (a) is found just above the Fermi level, which telltale the p-type self-doing character diminishing the quantum oscillation. Interestingly, a gapped Dirac cone (b) is found at the Fermi level, which exhibits paramount transport properties in the system. The red dash lines represent the position of the Fermi level in the electronic band structure.

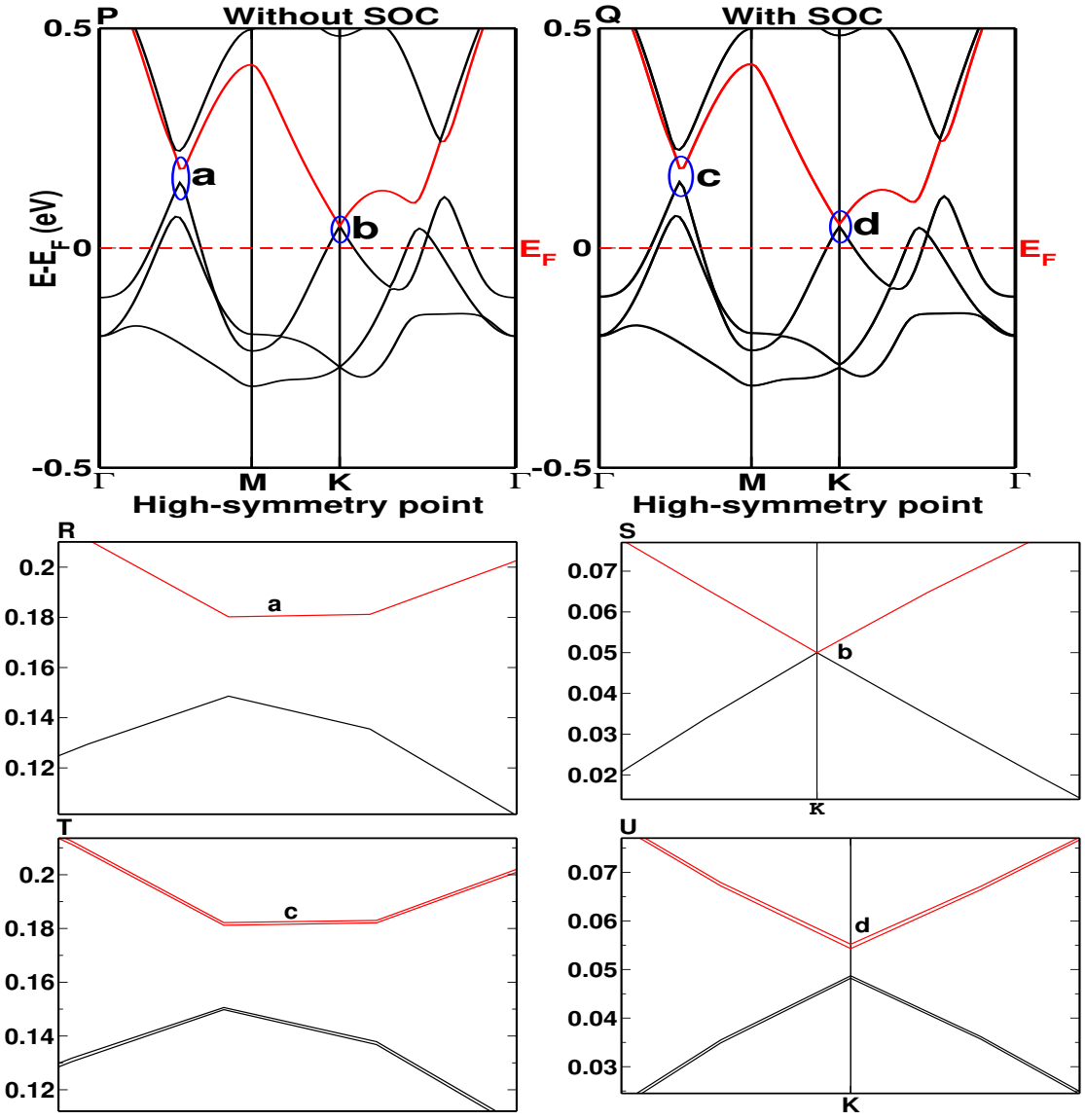

Figure 3.36: (Color online) P and Q represent the band structure corresponding to without SOC and SOC with 25% vacancy concentration of N within the frame $2 \times 2 \times 1$ super-cell in Ti_2NO_2 respectively. R, S, T, and U highlight the Dirac topology found in the electronic band structures. V represents the PDOS of N vacancy defect in stable NM configuration. The red dash lines represent the position of the Fermi level in the electronic band structure.

in the system [40]. The distorted Dirac cone above the Fermi level reveals the characteristic of the p-type self-doping character [38]. Under the SOC, the bands split and form two gapped distorted Dirac cones (c) and (d) near the Fermi level revealing the p and n-type self doping characters. Similarly, the Dirac cone (b) becomes more distorted (e) which diminishes the quantum oscillation under the presence of SOC. The N defect still remains metallic, which is also consistent with previously reported theoretical re-

sults [30]. The linear Dirac cone (a) is found in the region Γ-M above the Fermi level as shown in FIG. 3.36P. Similarly, a gapless linear Dirac cone (b) is found at K point above the Fermi level. Applying the strength of SOC on Ti atoms, the bands get splitted (shown in Dirac cones (c) and (d)) and opened at about 0.01 eV in Dirac cone (b) as shown in FIG. 3.36U [74].

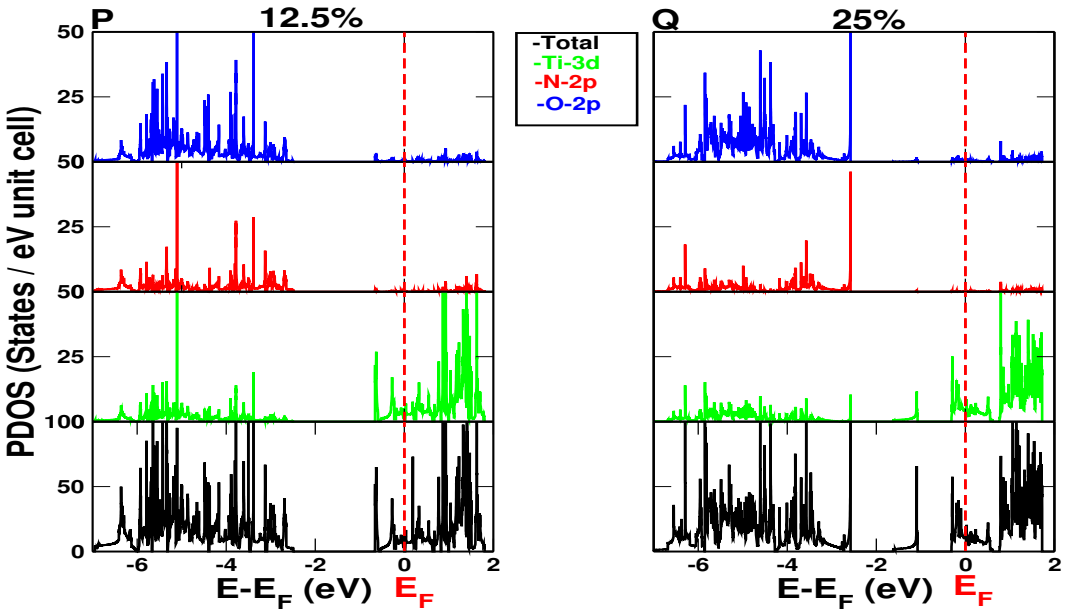

Figure 3.37: (Color online) P and Q represent the PDOS of O and N defects with vacancy concentrations 12.5% and 25% in $2 \times 2 \times 1$ super-cell of Ti_2NO_2, respectively . The red dash lines indicate the position of the Fermi level in PDOS.

To get better delineation on electronic band structure of Ti defect in $2 \times 2 \times 1$ and $3 \times 3 \times 1$ super-cells, the PDOS are shown in FIG. 3.34(R and S), respectively. In both super-cells, the conduction band near the Fermi level are mainly dominated by Ti-3*d* states. Similarly, the valence bands consist of Ti-3*d*, O-2*p*, and N-2*p* states with dominant character of O-2*p* states. The PDOS of O defect is shown in FIG. 3.37P. The bottom of valence bands are mainly dominated by N-2*p* and O-2*p* states, whereas the conduction bands are significantly dominated by Ti-3*d* states and trivial contribution from N-2*p* and O-2*p* states. Under the O defect, the Fermi level is shifted toward the unoccupied states forming the topological semi-metal.

Figure 3.37Q shows the PDOS of N defect in Ti_2NO_2. Similar to O defect, the valence bands are dominated by O-2*p* and N-2*p* states, whereas around and above the Fermi level are dominated by Ti-3*d* states.

3.2.6 Influrence of Cr, Mn, and Co Doping in Ti_2NO_2 MXene

Here, we performed the substitutional doping (12.5%) of different transition elements such as Cr, Mn, and Co in Ti_2NO_2 MXene within the pristine frame of $2 \times 2 \times 1$ super-cell. The substitution of TM elements break the bond length symmetry.

Under the Cr substitution, the global symmetry in bond length breaks down with slight changes. However, local symmetry is preserved near the dopant atom. The Cr-N bond length is found to be 2.09 Å, which is slightly shorter than that of Ti-N in pristine phase, whereas the Cr-O bond is found to be 2.09 Å, which is slightly larger than that of Ti-O in pristine. The elongation and compression of Cr-O and Cr-N bonds as compared to pristine significantly break the uniformity in bond length throughout the super-cell, which results significant influences in the electronic and magnetic properties.

In the case of Mn dopant, same baehaviors are found with slight variation in the bond length. But in the case of Co, the bond length between Co-O is found to be 2.27 Å, which is larger value by 0.27 Åas compared to Ti-O in pristine phase. Similarly, the Co-N bond is found to be 2.08 Å, which is shorter by 0.12 Åthan that of Ti-N. The elongation and compression in bond length results the Co atom slightly shifted toward bottom side as shown in FIG. 3.38c. The relaxed structures after substitutions of Mn,

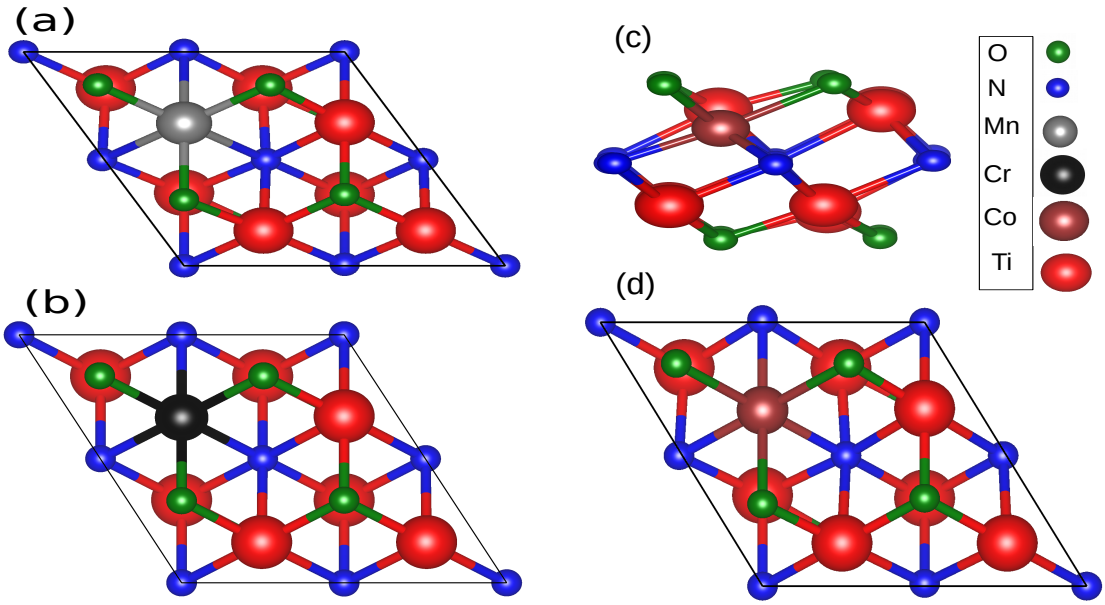

Figure 3.38: (Color online) (a) and (b) are top views of Mn, Cr doped, and (c) and (d) are side and top view of Co doped in Ti_2NO_2 of $2 \times 2 \times 1$ super-cell, respectively.

Cr, and Co in Ti_2NO_2 are shown in FIG. 3.38. The stability of doped systems were investigated through the formation energy using formula,

$$E_f = (E_{t1} - E_{t2}) - (E_1 - E_2) \tag{3.4}$$

Where E_{t1} and E_{t2} represent the total energy of Ti_2NO_2 with substitutional and pristine phases. E_1 and E_2 represent the free energy of single dopant and Ti atoms [77]. The calculated value of formation energies are 4.43 eV, 3.70 eV, and 3.81 eV in Mn, Cr, and Co doped MXenes, respectively [78]. The substitution of transition metals in MXene sheets inaugurate the significant change in the structural, electronic, and magnetic properties while favoring the magnetic configurations.

Figure 3.39 (P and Q) represents the spin polarized band structure and PDOS of Mn doped system. The Mn in Ti_2NO_2 allows to convert 100% spin polarized half-metallic to weakly semi-metallic nature. In the spin up channel, the band splits from Γ point below the Fermi level and reconstructs at other Γ point. Interestingly, these splitted bands form gapped type of Dirac cone at K point above the Fermi level in the spin up channel. The situation of band splitting for spin down channel is same as that of spin up channel. To describe the electronic band structure of Mn doped Ti_2NO_2, we divided the bands into separate sub-bands (i.e A, B, C, D, and E) in the spin up channel and three sub-bands (i.e A, B, and C) in the spin down channel, respectively. The conduction bands are significantly dominated by Ti-3*d* states and trivially contributed from other states. The sub-bands B and C are dominated by Mn-3*d* states. In the spin up channel, the energy gap between sub-bands A and B forms indirect energy gap of 0.52 eV. Similarly, the energy gaps between sub-bands B and C, and C and D are 0.62 eV (direct) and 0.19 eV (indirect), respectively. The sub-bands D and E are significantly concentrated from the O-2*p* states along with Ti-3*d* and Mn-3*d* states. In the case of spin down channel, the energy gap between sub-bands A and B is found to be 1.71 eV (direct). The same behavior is seen in sub-bands B and C.

Here, the asymmetrical nature of the PDOS corresponds to the spin up and spin down channels giving rise to ferromagnetism (3.98 μ_B per cell) preserving the weak semi-

metallic nature, which originates from the $3d$ states of Mn and Ti atoms. The intrinsic magnetic moment of Mn is 3.73 μ_B when it is dopped on the top layer of Ti_2NO_2. This doping reduces the magnetic moment of Ti from 0.28 μ_B to smaller but non negligible values.

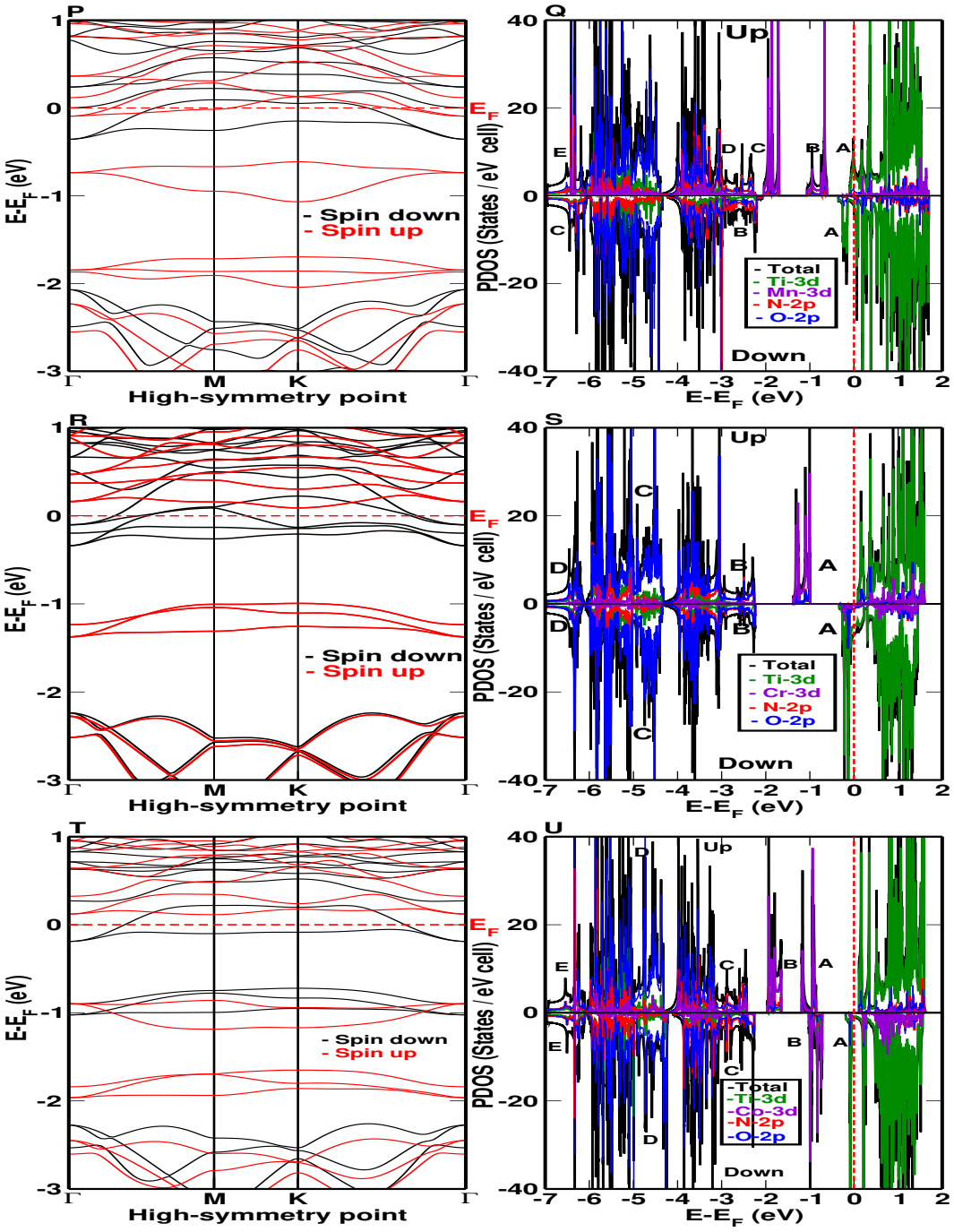

Figure 3.39: (Color online) P-Q, R-S, and T-U represent the electronic band structure and PDOS of Mn, Cr, and Co doped MXene Ti_2NO_2 in $2\times2\times1$ super-cell, respectively.

In contrast to Mn doped system, the spin up channel shows the semi-conducting

nature with direct band gaps of 1.07 eV (at K point) and 0.97 eV (at M point) for Cr and Co, respectively. The 3*d* electrons of TM are responsible for the semi-conducting behavior in both doped systems. In the spin down channel, the bands cross the Fermi level representing the metallic character. Thus, the semi-conducting nature in the spin up channel and metallic nature in the spin down channel predict the half-metallic character in both Cr and Co doped systems with 100% spin polarization.

For Cr dopped system (FIG. 3.39S), the bands above the Fermi level are mostly dominated by Ti-3*d* with smaller contributions from Cr-3*d*, O-2*p*, and N-2*p*. To describe valence states, we divided it into four different sub-bands A, B, C, and D. The sub-band A is dominated by Cr-3*d* states in the spin up channel and by Ti-3*d* states in the spin down channel. The direct energy gaps between the sub-bands A and B are 1.90 eV and 0.91 eV for spin down and spin up channels, respectively. The sub-bands B, C, and D are the mixed states with major contribution from the O-2*p* states.

Similarly, the PDOS of Co doped system is shown in Fig. 3.39U. In the unoccupied states, the bands are dominated by Ti-3d states. Coincidentally, two energy gaps are found toward the occupied states in both spin channels. In spin up channel, the sub-bands A and B are mainly dominated by Co-3*d* states forming an indirect energy gap of 0.47 eV. The energy gap between B and C forms indirect gap of 0.47 eV. In spin down channel, the sub-bands A and B are mainly dominated by Ti-3*d* and Co-3*d* states, respectively. The indirect energy gaps between sub-bands A and B, and B and C are of 0.5 eV and 1.34 eV, respectively. In both channels, the sub-bands C, D, and E show the major contribution from O-2*p* states along with N-2*p*, Ti-3*d*, and Mn-3*d* states.

3.2.7 Origin of Half-metallic Gap in Cr and Co Doped Ti_2NO_2

The 3*d* electrons of Cr and Co play a significant role for half-metallicity and magnetism. Figure 3.40 (P and Q) represents the projected spin polarized 3*d* DOS of Ti and Cr, respectively. The substitution of Cr allows to transform from half-metallic FM to half-metallic AFM. The half-metallicity is originated from both 3*d* electrons of Ti and Cr atoms. Unlike doped free phase, the Cr substitution changes the positive exchange

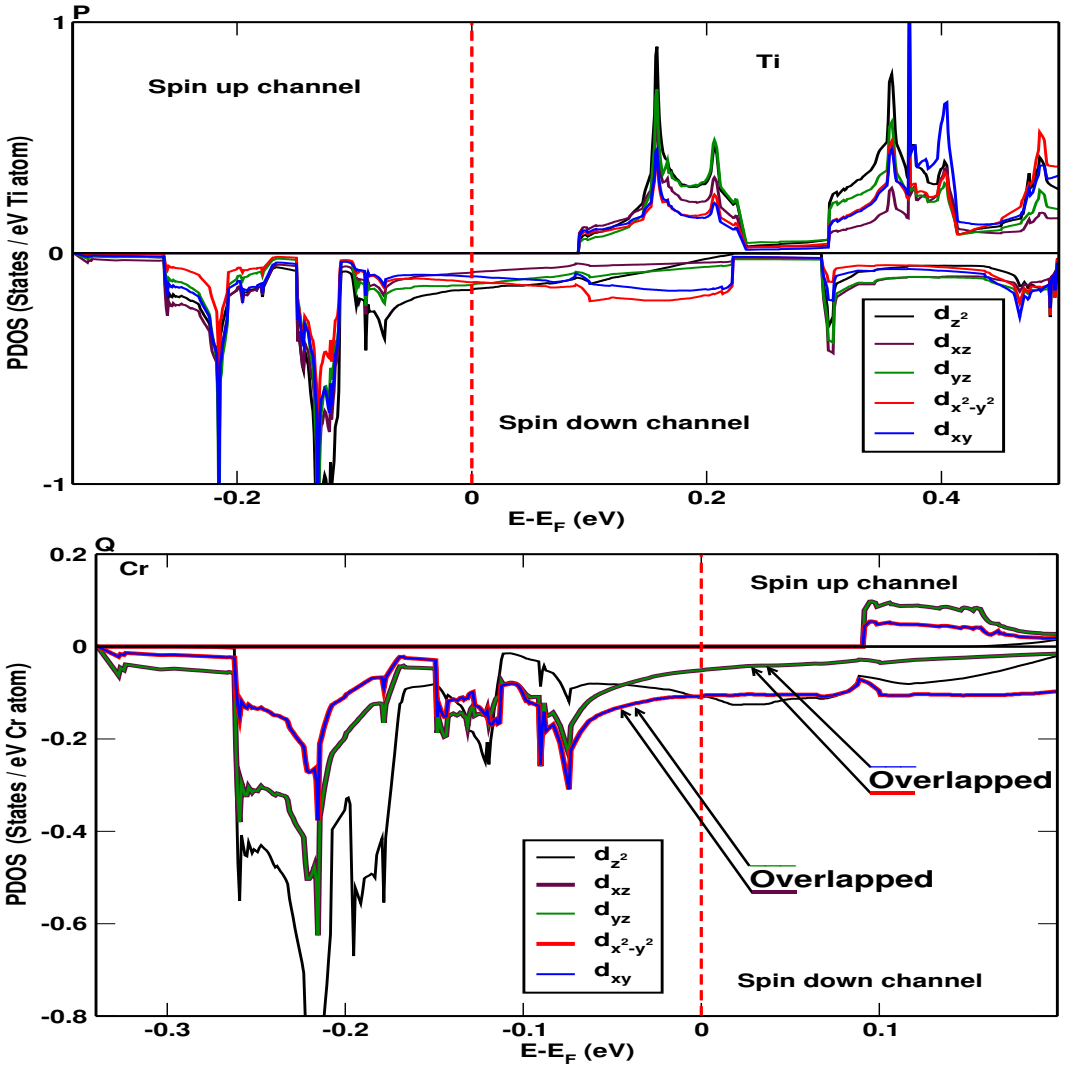

Figure 3.40: (Color online) P and Q represent the projected spin polarized 3*d* DOS of Ti and Cr following octahedral phase with D_{3d} point group corresponds to t_{2g} (d_{xz}, d_{yz}, and d_{xy}) and e_g ($d_{x^2-y^2}$ and d_{z^2}) states in Cr doped Ti_2NO_2. The red dash lines represent the position of the Fermi level.

to negative exchange splitting (spin up - spin down) with energy of 0.42 eV. The Cr substitution allows all the components of t_{2g} states (d_{xz}, d_{yz}, and d_{xy}) and e_g ($d_{x^2-y^2}$ and d_{z^2}) states of Ti to be non-degenerated states, whereas $d_{x^2-y^2}$ of e_g and d_{xy} of t_{2g}, and d_{xz} and d_{yz} of t_{2g} states are degenerated in the case of Cr. The d_{z^2} state also shows the dominant nature in both Ti and Cr atoms. In Cr doped case, there are two possibilities to fill the non-bonding states. Presuming all the constituents of Ti_2NO_2 are in their normal oxidation states, the top and bottom Ti atoms have either +4 or +3 oxidation states as mentioned above. Similarly, the top of Cr and bottom of Ti have either +4 or +3 oxidation states after providing two electrons to O and three electrons to N

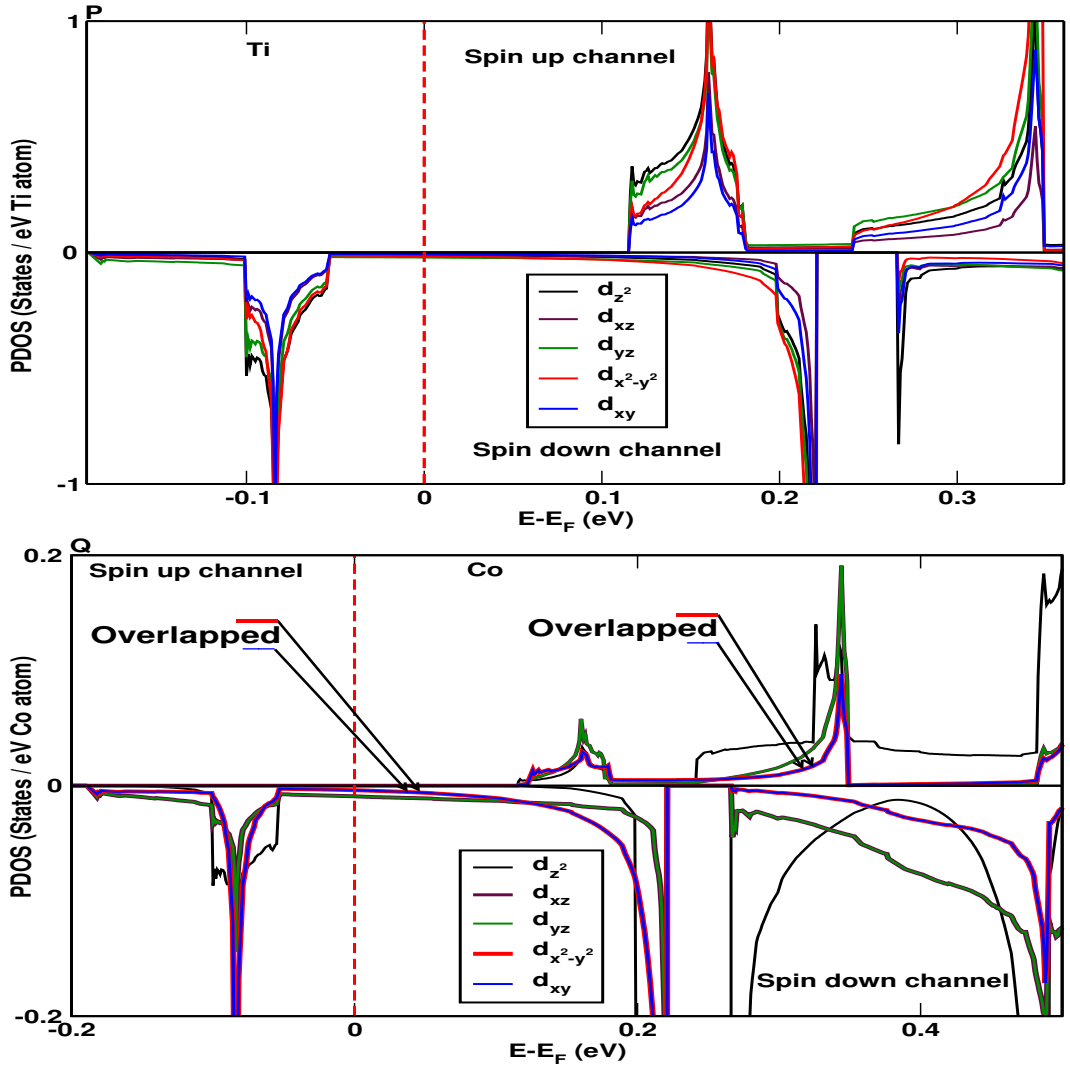

Figure 3.41: (Color online) P and Q represent the projected spin polarized 3*d* DOS of Ti and Co following octahedral phase with D_{3d} point group corresponds to t_{2g} (d_{xz}, d_{yz}, and d_{xy}) and e_g ($d_{x^2-y^2}$ and d_{z^2}) states in Co doped Ti_2NO_2. The red dash lines represent the position of the Fermi level.

atom. Following Hund's rule, the remaining 3*d* electrons of Ti and Cr fill partially the non-bonding states. These free 3*d* electrons in non-bonding states give AFM character. The individual magnetic moments of Ti and Cr align anti-parallely. The Cr moment here is one order magnitude larger than those of Ti atoms. Furthermore, the individual magnetic moments of Cr and Ti split the non-boding states into fully occupied bands in the spin down channel and open band gap in the spin up channel revealing the semiconducting behavior.

Similarly, Co substitution also preserves the FM half-metallic character with total magnetization of 1.05 μ_B. The magnetic moment of Co in Ti_2NO_2 is 1.90 μ_B, which dimin-

ishes the individual magnetic moments of Ti from 0.28 μ_B to smaller but non negligible values. The spin alignment of Co is anti-parallel with all Ti atoms except for one Ti in the bottom layer making the system overall FM. The Co substitution also favors the negative exchange splitting with energy 0.16 eV. Similarly, this substitution allows all the components of t_{2g} (d_{xz}, d_{yz}, and d_{xy}) and e_g ($d_{x^2-y^2}$ and d_{z^2}) states of Ti to be non-degenerate states, whereas $d_{x^2-y^2}$ of e_g and d_{xy} of t_{2g}, and d_{xz} and d_{yz} of t_{2g} states are degenerate states in the case of Co. The d_{z^2} state shows the dominant character in both Ti and Co.

3.3 Conclusions and Remarks

In summary, we have systematically studied the structural, electronic, and magnetic properties of MAX phase Ti_2AlN, bare MXene Ti_2N, and functionalized MXenes Ti_2NT_2 (T= -OH, -H, -O, -F). The formation and cohesive energies favor the chemical and structural stabilities in all MXenes and parent MAX phase. The Ti_2NO_2 is relatively stable among all MXenes starting from $2 \times 2 \times 1$ super-cell. The bare MXene is closely half-metallic FM but after surface termination, FM nature is completely removed without affecting the metallic nature except for O termination, which is found to be half-metallic FM. In addition, the half-metallic semi-metal is found for O surface functionalization in $3 \times 3 \times 1$ super-cell. The ferromagnetism in Ti_2N arises from Ti-3*d* states. The region near the Fermi level is dominated by Ti-3*d* states in all MXenes and MAX phase. The companionship of SOC influences strongly only in bare MXene and trivially influences with O and N defects thereby forming the multiple topological features.

The strained effect significantly influences the Fermi level with peculiar linear and distorted Dirac topological features. The Fermi level shift towards the lower energy states under compression and shift towards the higher energy states under tensile in Ti_2NH_2. These features are reversed in the case of Ti_2N, Ti_2NF_2, and $Ti_2N(OH)_2$. The 100% spin polarized half-metallic nature changes to closely half-metallic under 1% compression and it is completely destroyed under 2% compression in O termination. The defect in

Ti_2NO_2 completely changes the electronic properties from half-metal to semi-conductor with certain band gap and fascinating topological semi-metal for in 12.5% Ti and O atoms, respectively. In the N defect, the material becomes metallic with paramount topological phenomenon. The variable vacancy concentration allows to change the weak semi-conductor to strong semi-conductor in Ti_2NO_2. The 12.5% Co substitution in Ti_2NO_2 preserves the half-metallic character, whereas Mn substitution changes the electronic properties from half-metallic to weak semi-metallic preserving FM character. However, Cr substitution changes the magnetic properties from FM to AFM preserving half-metallic character. The magnetism and half-metallicity are mainly due to different orbital filling configurations of $3d$ electrons of TM. The presence of half-metallicity in pristine, and Cr and Co substitutions could provide magnetic functionalities in spintronic applications.

We believe that this research work would play a vital role in the further enhancement to carry out further computation in the field of nitride based MXenes such as optical, transport, and adsorption properties. I am very much hopeful that research work will be helpful for those researchers those who are interested to work in the field of MXenes.

References

[1] Y. Xie and P. Kent, Phys. Rev. B **87**, 235441 (2013).

[2] N. Zhang, Y. Hong, S. Yazdanparast, and M. A. Zaeem, 2D Mater. **5**, 045004 (2018).

[3] A. Szuplewska, A. Rozmysłowska-Wojciechowska, S. Poźniak, T. Wojciechowski, M. Birowska, M. Popielski, M. Chudy, W. Ziemkowska, L. Chlubny, D. Moszczyńska, *et al.*, J. Nanobiotechnology **17**, 1 (2019).

[4] "Electronic band structure," `https://en.wikipedia.org/wiki/Electronic_band_structure`, accessed: 2021-01-03.

[5] K. S. Novoselov, A. K. Geim, S. V. Morozov, D. Jiang, Y. Zhang, S. V. Dubonos, I. V. Grigorieva, and A. A. Firsov, science **306**, 666 (2004).

[6] R. Mas-Balleste, C. Gomez-Navarro, J. Gomez-Herrero, and F. Zamora, Nanoscale **3**, 20 (2011).

[7] C. Tan, X. Cao, X.-J. Wu, Q. He, J. Yang, X. Zhang, J. Chen, W. Zhao, S. Han, G.-H. Nam, *et al.*, Chem. Rev. **117**, 6225 (2017).

[8] M. J. Allen, V. C. Tung, and R. B. Kaner, Chem. Rev. **110**, 132 (2010).

[9] Q. Jiang, N. Kurra, M. Alhabeb, Y. Gogotsi, and H. N. Alshareef, Adv. Energy Mater. **8**, 1703043 (2018).

[10] N. K. Chaudhari, H. Jin, B. Kim, D. San Baek, S. H. Joo, and K. Lee, J. Mater. Chem. A **5**, 24564 (2017).

[11] K. Huang, Z. Li, J. Lin, G. Han, and P. Huang, Chem. Soc. Rev. **47**, 5109 (2018).

[12] A. Sinha, H. Zhao, Y. Huang, X. Lu, J. Chen, R. Jain, *et al.*, Trends Analyt Chem **105**, 424 (2018).

[13] X. Li, C. Wang, Y. Cao, and G. Wang, Chem.: Asian J. **13**, 2742 (2018).

[14] H. Kumar, N. C. Frey, L. Dong, B. Anasori, Y. Gogotsi, and V. B. Shenoy, ACS nano **11**, 7648 (2017).

[15] B. Anasori, M. R. Lukatskaya, and Y. Gogotsi, Nat. Rev. Mater. **2**, 1 (2017).

[16] M. Magnuson, O. Wilhelmsson, J.-P. Palmquist, U. Jansson, M. Mattesini, S. Li, R. Ahuja, and O. Eriksson, Phys. Rev. B **74**, 195108 (2006).

[17] M. W. Barsoum and M. Radovic, Annu. Rev. Mater. Sci. **41**, 195 (2011).

[18] N. C. Osti, M. Naguib, A. Ostadhossein, Y. Xie, P. R. Kent, B. Dyatkin, G. Rother, W. T. Heller, A. C. Van Duin, Y. Gogotsi, *et al.*, ACS Appl. Mater. Interfaces **8**, 8859 (2016).

[19] M. Ghidiu, S. Kota, J. Halim, A. W. Sherwood, N. Nedfors, J. Rosen, V. N. Mochalin, and M. W. Barsoum, Chem. Mater. **29**, 1099 (2017).

[20] A. Lipatov, M. Alhabeb, M. R. Lukatskaya, A. Boson, Y. Gogotsi, and A. Sinitskii, Adv. Electron. Mater. **2**, 1600255 (2016).

[21] M. Pandey and K. S. Thygesen, J. Phys. Chem. C **121**, 13593 (2017).

[22] B. Soundiraraju and B. K. George, ACS nano **11**, 8892 (2017).

[23] P. Urbankowski, B. Anasori, T. Makaryan, D. Er, S. Kota, P. L. Walsh, M. Zhao, V. B. Shenoy, M. W. Barsoum, and Y. Gogotsi, Nanoscale **8**, 11385 (2016).

[24] C. Zhan, W. Sun, P. R. Kent, M. Naguib, Y. Gogotsi, and D.-e. Jiang, J. Phys. Chem. C **123**, 315 (2018).

[25] K. Hantanasirisakul and Y. Gogotsi, Adv. Mater. **30**, 1804779 (2018).

[26] S. Postorino, D. Grassano, M. DAlessandro, A. Pianetti, O. Pulci, and M. Palummo, Nanomater. Nanotechnol. **10**, 1847980420902569 (2020).

[27] M. Sharma, A. Kumar, P. Ahluwalia, and R. Pandey, J. Appl. Phys. **116**, 063711 (2014).

[28] C. Lee, X. Wei, J. W. Kysar, and J. Hone, science **321**, 385 (2008).

[29] Y. Li, N. Li, S. Zhao, J. Fan, and J.-J. Kai, J. Mater. Chem. A **8**, 760 (2020).

[30] A. Bandyopadhyay, D. Ghosh, and S. K. Pati, Phys. Chem. Chem. Phys. **20**, 4012 (2018).

[31] X. Sang, Y. Xie, M.-W. Lin, M. Alhabeb, K. L. Van Aken, Y. Gogotsi, P. R. Kent, K. Xiao, and R. R. Unocic, ACS nano **10**, 9193 (2016).

[32] R. Liu, W. Cao, D. Han, Y. Mo, H. Zeng, H. Yang, and W. Li, J. Alloys Compd. **793**, 505 (2019).

[33] C.-F. Du, X. Sun, H. Yu, Q. Liang, K. N. Dinh, Y. Zheng, Y. Luo, Z. Wang, and Q. Yan, Adv. Sci. **6**, 1900116 (2019).

[34] P. Chakraborty, T. Das, D. Nafday, L. Boeri, and T. Saha-Dasgupta, Phys. Rev. B **95**, 184106 (2017).

[35] L. Pan, B. Song, J. Sun, L. Zhang, W. Hofer, S. Du, and H.-j. Gao, J. Phys.: Condens. Matter **25**, 505502 (2013).

[36] K. Nagao, Y. Miura, and M. Shirai, Phys. Rev. B **73**, 104447 (2006).

[37] K. Inomata, N. Ikeda, N. Tezuka, R. Goto, S. Sugimoto, M. Wojcik, and E. Jedryka, Sci. Technol. Adv. Mater. **9**, 014101 (2008).

[38] L.-C. Xu, R.-Z. Wang, M.-S. Miao, X.-L. Wei, Y.-P. Chen, H. Yan, W.-M. Lau, L.-M. Liu, and Y.-M. Ma, Nanoscale **6**, 1113 (2014).

[39] D. Malko, C. Neiss, F. Vines, and A. Görling, Phys. Rev. Lett. **108**, 086804 (2012).

[40] N. Tajima, Crystals **8**, 126 (2018).

[41] Y. Zhang, Y.-W. Tan, H. L. Stormer, and P. Kim, nature **438**, 201 (2005).

[42] F. Islam, R. Choudhary, Y. Liu, B. G. Ueland, D. Paudyal, T. Heitmann, R. J. McQueeney, and D. Vaknin, Phys. Rev. B **102**, 085130 (2020).

[43] X. Shao, X. Liu, X. Zhang, J. Wang, and M. Zhao, Phys. Chem. Chem. Phys. **20**, 3946 (2018).

[44] H. Fashandi, V. Ivády, P. Eklund, A. L. Spetz, M. I. Katsnelson, and I. A. Abrikosov, Phys. Rev. B **92**, 155142 (2015).

[45] P. Phillips, "Advanced solid state physics. advanced book program," (2003).

[46] B. AGARWAL and H. PRAKASH, *QUANTAM MECHANICS* (PHI Learning, 1996).

[47] C. D. Sherrill, School of Chemistry and Biochemistry Georgia Institute of Technology (2000).

[48] R. G. Parr and S. K. Ghosh, Proc. Natl. Acad. Sci. **83**, 3577 (1986).

[49] P. Hohenberg and W. Kohn, Phys. Rev. **136**, B864 (1964).

[50] D. Sholl and J. A. Steckel, *Density functional theory: a practical introduction* (John Wiley & Sons, 2011).

[51] W. Koch and M. Holthausen, VCH Weinheim **300**, 3527600043 (2001).

[52] J. P. Perdew, K. Burke, and M. Ernzerhof, Phys. Rev. Lett. **77**, 3865 (1996).

[53] P. E. Blöchl, Phys. Rev. B **50**, 17953 (1994).

[54] R. M. Ronchi, J. T. Arantes, and S. F. Santos, Ceram. Int. **45**, 18167 (2019).

[55] H. Tang, W. Li, L. Pan, K. Tu, F. Du, T. Qiu, J. Yang, C. P. Cullen, N. McEvoy, and C. Zhang, Adv. Funct. Mater. **29**, 1901907 (2019).

[56] J. L. Hart, K. Hantanasirisakul, A. C. Lang, B. Anasori, D. Pinto, Y. Pivak, J. T. van Omme, S. J. May, Y. Gogotsi, and M. L. Taheri, Nat. Commun. **10**, 1 (2019).

[57] P. Giannozzi, S. Baroni, N. Bonini, M. Calandra, R. Car, C. Cavazzoni, D. Ceresoli, G. L. Chiarotti, M. Cococcioni, I. Dabo, *et al.*, J. Phys. Condens. Matter **21**, 395502 (2009).

[58] M. Naguib, V. N. Mochalin, M. W. Barsoum, and Y. Gogotsi, Adv. Mater. **26**, 992 (2014).

[59] V. M. H. Ng, H. Huang, K. Zhou, P. S. Lee, W. Que, J. Z. Xu, and L. B. Kong, J. Mater. Chem. A **5**, 3039 (2017).

[60] D. Wang, Y. Gao, Y. Liu, D. Jin, Y. Gogotsi, X. Meng, F. Du, G. Chen, and Y. Wei, J. Phys. Chem. C **121**, 13025 (2017).

[61] X. Wang, Z. Cheng, J. Wang, L. Wang, Z. Yu, C. Fang, J. Yang, and G. Liu, RSC Adv. **6**, 57041 (2016).

[62] G. Gao, G. Ding, J. Li, K. Yao, M. Wu, and M. Qian, Nanoscale **8**, 8986 (2016).

[63] J. E. Saal, S. Kirklin, M. Aykol, B. Meredig, and C. Wolverton, Jom **65**, 1501 (2013).

[64] S. Kirklin, J. E. Saal, B. Meredig, A. Thompson, J. W. Doak, M. Aykol, S. Rühl, and C. Wolverton, Npj Comput. Mater. **1**, 1 (2015).

[65] Y. Zhou and Z. Sun, Phys. Rev. B **61**, 12570 (2000).

[66] G. Hug and E. Fries, Phys. Rev. B **65**, 113104 (2002).

[67] G. Chang, B. Singh, S.-Y. Xu, G. Bian, S.-M. Huang, C.-H. Hsu, I. Belopolski, N. Alidoust, D. S. Sanchez, H. Zheng, *et al.*, Phys. Rev. B **97**, 041104 (2018).

[68] F. Guillou, D. Paudyal, Y. Mudryk, A. K. Pathak, V. Smetana, A.-V. Mudring, and V. K. Pecharsky, J. Magn. Magn. Mater. **501**, 166405 (2020).

[69] L. Benfatto and E. Cappelluti, Phys. Rev. B **78**, 115434 (2008).

[70] M. Khazaei, M. Arai, T. Sasaki, C.-Y. Chung, N. S. Venkataramanan, M. Estili, Y. Sakka, and Y. Kawazoe, Adv. Funct. Mater. **23**, 2185 (2013).

[71] M. Zhao and R. Zhang, Phys. Rev. B **89**, 195427 (2014).

[72] L. Petit, D. Paudyal, Y. Mudryk, K. Gschneidner Jr, V. Pecharsky, M. Lüders, Z. Szotek, R. Banerjee, and J. Staunton, Phys. Rev. Lett. **115**, 207201 (2015).

[73] M. Chhowalla, H. S. Shin, G. Eda, L.-J. Li, K. P. Loh, and H. Zhang, Nat. Chem **5**, 263 (2013).

[74] M. Khazaei, A. Ranjbar, M. Arai, and S. Yunoki, Phys. Rev. B **94**, 125152 (2016).

[75] M. Katsnelson, V. Y. Irkhin, L. Chioncel, A. Lichtenstein, and R. A. de Groot, Rev. Mod. Phys. **80**, 315 (2008).

[76] X. Li and J. Yang, Natl. Sci. Rev. **3**, 365 (2016).

[77] Y.-j. Liu, B. Gao, D. Xu, H.-m. Wang, and J.-x. Zhao, Phys. Lett. A **378**, 2989 (2014).

[78] S. Yu, W. Zheng, Q. Wen, and Q. Jiang, Carbon **46**, 537 (2008).